Electronic Supplementary Information (ESI) to accompany:

Screening Metal-Organic Frameworks for Separation of Pentane Isomers

Rajamani Krishna*

Van 't Hoff Institute for Molecular Sciences, University of Amsterdam, Science Park 904,

1098 XH Amsterdam, The Netherlands

and

Jasper M. van Baten

AmsterCHEM, Calle Las Rozas 32,

04618 Las Rozas, Cuevas del Almanzora,

Almería, SPAIN

*email: r.krishna@contact.uva.nl

Table of Contents

1. Preamble

This ESI accompanying the article *Screening Metal-Organic Frameworks for Separation of Pentane Isomers* provides the following background information.

(i) Summary of CBMC simulation methodology, along with force fields used.

(ii) Structural data on zeolites, MOFs, and ZIFs.

(iii) CBMC simulation data for unary and mixture isotherms, presented in graphical form, for each of the micro-crystalline adsorbent materials.

(iv) Tabulated data on the dual-site Langmuir-Freundlich fit parameters for the unary pentane isotherms.

(v) Simulation methodology for transient breakthrough in fixed bed adsorbers

(vi) Details of simulation results for transient breakthroughs.

For ease of reading, this ESI is written as a stand-alone document; as a consequence, there is some overlap of material with the main manuscript.

The following video animations have been uploaded as ESI.

(1) Transient breakthrough of nC5/2MB mixture with $Fe_2(BDP)_3$ as adsorbent. The video shows the transient development of the gas phase concentrations of nC5, and 2MB along the length of the fixed bed adsorber.

(2) Transient breakthrough of 2MB/neo-P mixture with $Fe_2(BDP)_3$ as adsorbent. The video shows the transient development of the gas phase concentrations of 2MB, and neo-P along the length of the fixed bed adsorber.

2. CBMC simulation methodology

For comparison of the separation performance of zeolites, MOFs, and ZIFs, CBMC simulations have been carried out to determine the adsorption isotherms for pentanes in various microporus crystalline adsorbents. The CBMC simulation methodology is precisely the same as described in our earlier works. [1-6] For ease of reading, a brief summary of the methodology is provided hereunder. We use the united atom model. The crystalline framework is considered to be rigid. We consider the CH_x groups as single, chargeless interaction centers with their own effective potentials. For simulations with linear alkanes with two or more C atoms, the beads in the chain are connected by harmonic bonding potentials. A harmonic cosine bending potential models the bond bending between three neighboring beads, a Ryckaert-Bellemans potential controls the torsion angle. The beads in a chain separated by more than three bonds interact with each other through a Lennard-Jones potential. The Lennard-Jones potentials are shifted and cut at 12 Å. Periodic boundary conditions were employed. The zeolite, MOF and ZIF structures were considered to be rigid in the simulations.

The force fields of Dubbeldam et al.[1, 2] was used for the variety of potentials to describe alkane/MFI interactions.

For the atoms in the host MOF and ZIF frameworks, the generic UFF [7] and DREIDING [8] force fields were used. The Lennard-Jones parameters for MOF and ZIF atoms are summarized in Tables 3, 4, 5, 6, 7, 8, 9, 10. The Lorentz-Berthelot mixing rules were applied for calculating σ and ε/k_B for guest-host interactions. For Zn(bdc)dabco, the force field information used is that provided in earlier work.[2, 9] For ZIF-77, the force field implementation is described in detail by Dubbeldam et al.[2]

The CBMC simulations were performed using the BIGMAC code developed by T.J.H. Vlugt[10] as basis.

3. Molecular simulations of heats of adsorption

We determined the isosteric heats of adsorption, ΔH, from CBMC simulations using the fluctuation formula

$$\Delta H = RT - \frac{<U_i n_i> - <U_i><n_i>}{\langle n_i^2 \rangle - \langle n_i \rangle^2} \qquad (1)$$

where n_i represents the number of molecules in the simulation box and $\langle \ldots \rangle$ denotes ensemble averaging. In this connection the reader is referred to the paper of Karavias and Myers [11], who point out that the conventional definition of the isosteric heat of *adsorption* is in reality the heat of *desorption*.

4. Structural information on zeolites, MOFs, and ZIFs

For MFI zeolite, the crystallographic structural data are available on the zeolite atlas website of the International Zeolite Association (IZA).[12] The structural data, and pore landscapes along with snapshots of pentanes are provided in Figures 1, 2, 3.

The structural information for BeBTB = $Be_{12}(OH)_{12}(BTB)_4$ with (BTB^{3-} = 1,3,5-benzenetribenzoate) is from Sumida et al.[13] The structural data, and pore landscapes along with snapshots of pentanes are provided in Figures 4, 5, 6.

The structural information for Co(BDP) with (BDP^{2-} = 1,4-benzenedipyrazolate) is from Choi et al. [14] and Salles et al.[15] The structural data, and pore landscapes along with snapshots of pentanes are provided in Figures 7, 8, 9.

The structural information for CuBTT is from Demessence et al.[16] The structural data, and pore landscapes along with snapshots of pentanes are provided in Figures 10, 11, 12.

For $Fe_2(BDP)_3$ (BDP^{2-} = 1,4-benzenedipyrazolate), we used the structural data published by Herm et al.[4] For appreciation of the pore structure of $Fe_2(BDP)_3$ the pore landscapes were constructed using the structural information. The channels are triangular in shape, with a pore size of 4.9 Å, as determined from molecular simulations. The structural data, and pore landscapes along with snapshots of pentane and hexane isomers are provided in Figures 13, 14, 15.

For IRMOF-1 (= MOF 5 = $Zn_4O(BDC)_3$ with BDC^{2-} = 1-4 benzenedicarboxylate), we used the structural data published by Dubbeldam et al. [17, 18] The structural data, and pore landscapes along with snapshots of pentanes are provided in Figures 16, 17, 18.

The structural information on MgMOF-74 (= Mg_2(dobdc) = Mg\(dobdc) with dobdc = ($dobdc^{4-}$ = 1,4-dioxido-2,5-benzenedicarboxylate)), ZnMOF-74 (= Zn_2(dobdc) = Zn\(dobdc)), were obtained from a variety of references.[19-24] The structural data, and pore landscapes of MgMOF-74 along with snapshots of pentanes are provided in Figures 19, 20, 21, 22. The structural data, and pore landscapes of ZnMOF-74 along with snapshots of pentanes are provided in Figures 23, 24, 25. The simulations for ZnMOF-74 and MgMOF-74 were carried out with the force field information provided by Yazaydin et al.[24] See Tables 8 and 9.

The structural information for MOF-177 (= $Zn_4O(BTB)_2$ with (BTB^{3-} = 1,3,5-benzenetribenzoate)) is provided by Chae et al.[25] The structural data, and pore landscapes, along with snapshots of alkanes are provided in Figures 26, 27, 28. The force field information for MOF-177 is summarized in Table 10.

The structural information for Zn(bdc)dabco is from Bárcia et al.[26] and Lee et al. [27] The structural data, and pore landscapes, along with snapshots of pentanes are provided in Figures 29, 30, 31, 32.

The structural data for ZIF-77 were taken from Dubbeldam et al.[2] The characteristic pore size of ZIF-77 is 4.5 Å, significantly smaller than the 4.9 Å sized triangular channels of $Fe_2(BDP)_3$. The structural data, and pore landscapes are provided in Figures 33, 34.

The ZIF-8 = Zn(methylimidazole)$_2$ structure was constructed on the basis of the structural data from Banerjee et al.[28] The structural data, and pore landscapes, are provided in Figures 35, 36.

Unary nC5, 2MB, and neo-P isotherms and nC5(1)/2MB(2)/neo-P(3) mixture isotherms (for equimolar mixtures in the bulk fluid phase, $f_1=f_2=f_3$) were determined at a temperature of 433 K, that is typical of the temperatures used for separation of alkane isomers.[2-4, 6] Earlier published data[2-4] are also gainfully utilized in the analysis of the nC5/2MB/neo-P mixture separations with different adsorbents.

5. CBMC simulation data for alkanes adsorption in MFI zeolite

Figure 37 presents CBMC simulation results for adsorption of pentanes in all-silica MFI zeolite at 433 K. Figure 37a are the CBMC simulated unary isotherms for nC5, 2MB, and neo-P; the continuous solid lines are the isotherm fits with dual-site Langmuir-Freundlich model

$$q_i = q_{i,A,sat} \frac{b_{i,A} f_i^{v_{i,A}}}{1 + b_{i,A} f_i^{v_{i,A}}} + q_{i,B,sat} \frac{b_{i,B} f_i^{v_{i,B}}}{1 + b_{i,B} f_i^{v_{i,B}}} \tag{2}$$

The fit parameters are specified in Table 11. The linear nC5 has a saturation loading of 8 molecules per unit cell. This is explained on the basis of the snapshots in Figure 3; nC5 can locate anywhere along the straight and zig-zag channels. In sharp contrast, the saturation loadings of both 2MB and neo-P are restricted to 4 molecules per unit cell; this is because the branched isomers can only locate at the channel intersections of which there are 4 per unit cell.

Figure 37b shows the CBMC simulations for equimolar nC5/2MB/neo-P mixture in MFI zeolite; the partial fugacities of each component in the bulk fluid phase are equal, i.e., $f_1 = f_2 = f_3$. The CBMC mixture adsorption data has been plotted with two different x-axes: (i) the total bulk phase fugacity, $f_t = f_1 + f_2 + f_3$, and total mixture loading $\Theta_t = \Theta_1 + \Theta_2 + \Theta_3$, expressed in molecule per unit cell. The continuous solid lines are the estimations using the Ideal Adsorbed Solution Theory (IAST) of Myers and Prausnitz[29] using the pure component isotherm fits. The nC5 loading increases sharply as the total mixture loading Θ_t exceeds 4 molecules per unit cell; at this loading, all the channel intersections are occupied. Entropy effects cause the selectivity to increase significantly in favor of the linear isomer for loadings $\Theta_t > 4$/uc. Entropy effects are quantitatively captured by the IAST predictions.

Figure 37c shows the nC5/2MB selectivity as a function of the total hydrocarbons fugacity. The sharp increase in the selectivity at total fugacities $f_t > 100$ kPa occurs when the total mixture loading exceeds 4 molecules per unit cell.

Figure 37d shows 2MB/neo-P selectivity as a function of the total hydrocarbons fugacity, $f_t > 100$ kPa. We again note that for $f_t > 20$ kPa, there is a sharp increase in the selectivity because all the intersection sites are occupied. Entropy effects favor the mono-branched isomer 2MB.

Entropy effects in MFI zeolite also manifest for adsorption of hexane isomers: n-hexane (nC6), 2-methylpentane (2MP), 3-methylpentane (3MP), 2,2-dimethylbutane (22DMB). Figure 38a shows the unary isotherms, fitted with the dual-site Langmuir-Freundlich model. Figure 38b presents CBMC simulations of component loadings in a ternary equimolar nC6/3MP/22DMB mixture at 433 K as a

function of the total hydrocarbons fugacity f_t. The IAST (continuous solids lines) predicts entropy effects in quantitative agreement with CBMC simulations. The plot of the component loading Θ_i as a function of the total mixture loading Θ_t (cf. Figure 38c), demonstrates that configurational entropy effects manifest at $\Theta_t > 4$, causing the hierarchy of component loadings to be nC6 > 3MP > 22DMB. The total mixture loading of $\Theta_t = 4$/uc is attained at a total hydrocarbons fugacity $f_t \approx 0.1$ MPa. This suggests the efficacy of MFI for separating hexane isomers according to the degree of branching; we need to operate at $f_t > 0.1$ MPa.

Entropy effects also manifest for 5-component nC6/2MP/3MP/22DMB/23DMB mixtures in MFI zeolite. The pure component isotherms are shown in Figure 39a; the continuous solid lines are the unary isotherm fits with the dual-site Langmuir-Freundlich model. Figure 39b presents CBMC simulations of component loadings in a 5-component nC6/2MP/3MP/22DMB/23DMB mixture at 433 K as a function of the total hydrocarbons fugacity f_t. The IAST calculations are in good agreement with the CBMC simulations. The plot of the component loading Θ_i as a function of the total mixture loading Θ_t (cf. Figure 39c), demonstrates that configurational entropy effects manifest at $\Theta_t > 4$/uc, causing the hierarchy of component loadings to be nC6 > 2MP > 3MP > 23DMB > 22DMB. The total mixture loading of $\Theta_t = 4$ is attained at a total hydrocarbons fuactity $f_t \approx 0.3$ MPa. This suggests the efficacy of MFI for separating hexane isomers according to the degree of branching; we need to operate at $f_t > 0.3$ MPa.

6. CBMC simulation data for alkanes adsorption in MOFs, and ZIFs

Figure 40 presents the CBMC simulation results for adsorption of pentanes in BeBTB at 433 K. Note that the pure component isotherms were not determined in this case. The nC5/2MB and 2MB/neo-P selectivities are lie in the range 1- 2.5.

Figure 41 presents CBMC simulation results for adsorption of pentanes in Co(BDP) at 433 K. The nC5/2MB and 2MB/neo-P selectivities lie in the range 1- 3.4.

Figure 42 presents the CBMC simulation results for adsorption of pentanes in CuBTT at 433 K. Note that the pure component isotherms were not determined in this case. The nC5/2MB and 2MB/neo-P selectivities lie in the range 1- 3.6.

Figure 43a presents the CBMC data for unary isotherms for nC5, 2MB, and neo-P in $Fe_2(BDP)_3$ at 433 K. The hierarchy of component loadings is nC5 >> 2MB >>neo-P. To understand the hierarchy, snapshots of the alignment of guest pentane molecules within the triangular channels of $Fe_2(BDP)_3$ are shown in Figure 15. The linear nC5 appears to align, almost commensurately, within the channel landscape; this allows maximum degree of van der Waals interactions of the C atoms with the walls. The branched isomers 2MB and neo-P are significantly more constrained within the triangular channels; not all of the C atoms can effectively interact with the pore walls. The compact neo-P molecule exerts the least amount of van der Waals interactions with the pore walls, and consequently has the lowest adsorption strength.

The molecular simulation data for the heats of adsorption (cf. Figure 43b) show that the binding energy of nC5 is about factor two higher than that of 2MB; the binding energy of 2MB is, in turn, a factor two higher than that of neo-P.

Figure 44a presents the corresponding CBMC simulation results for unary adsorption of hexane isomers: n-hexane (nC6), 2-methylpentane (2MP), 3-methylpentane (3MP), 2,2-dimethylbutane (22DMB) and 2,3-dimethylbutane (23DMB) in $Fe_2(BDP)_3$ at 433 K. The continuous solid lines in (a) and (b) are dual-site Langmuir fits with fit parameters specified in Table 13. The adsorption hierarchy is nC6 >2MP≈3MP>22DMB>23DMB. This is also the hierarchy of the heats of adsorption; see Figure 44b. Figure 44c presents the CBMC simulation results for unary adsorption of heptane isomers: n-heptane (nC7), 2-methylhexane (2MH), 3-methylhexane (3MH), 2,2-dimethylpentane (22DMP) and 2,3-dimethylpentane (23DMP) in $Fe_2(BDP)_3$. The adsorption hierarchy is nC7 >2MH>3MH>22DMP>23DMP.

Figure 45a presents the CBMC simulations of the component loadings for adsorption of enC5/2MB/neo-P mixtures, with equal partial fugacities in the bulk fluid phase, $f_1=f_2=f_3$. The continuous

solid lines are the IAST estimations using the pure component isotherm fits; there is excellent agreement between the CBMC mixture simulations and IAST predictions. The nC5/2MB selectivity lies in the range 20 – 54; Figure 45b. The 2MB/neo-P selectivity lies in the range 100-300; Figure 45c.

The accuracy of IAST calculations to predict mixture adsorption equilibrium in $Fe_2(BDP)_3$ also holds for mixtures containing hexane and heptane isomers. In order to demonstrate this, Figures 46a,b present CBMC simulation data (symbols) for adsorption of (a) 5-component hexanes: nC6/2MP/3MP/22DMB/23DMB in $Fe_2(BDP)_3$ at 433 K, and (b) 8-component pentanes/hexanes mixture: nC5/2MB/neoP/nC6/2MP/3MP/22DMB/23DMB in $Fe_2(BDP)_3$ at 433 K. The continuous solid lines are the IAST estimations using the pure component isotherm fits specified in Table 13. There is excellent, near-perfect agreement between CBMC mixture simulations and IAST predictions.

The CBMC mixture simulation data for adsorption of 13-component pentanes/hexanes/heptanes nC5/2MB/neoP/nC6/2MP/3MP/22DMB/23DMB/nC7/2MH/3MH/22DMP/23DMP in $Fe_2(BDP)_3$ at 433 K are presented in Figure 47. The continuous solid lines are IAST calculations of the mixture equilibrium using the dual-site Langmuir- parameters in Table 13. There is excellent, near-perfect agreement between CBMC mixture simulations and IAST predictions.

Figure 48 presents the CBMC simulation results for adsorption of pentanes in IRMOF-1 at 433 K. Note that the pure component isotherms were not determined in this case. The nC5/2MB and 2MB/neo-P selectivities lie in the range 1- 2.8.

Figure 49 presents the CBMC simulation results for adsorption of pentanes in MgMOF-74 at 433 K. The nC5/2MB and 2MB/neo-P selectivities lie in the range 1.2- 3.8.

Figure 50 presents the CBMC simulation results for adsorption of pentanes in ZnMOF-74 at 433 K. The nC5/2MB and 2MB/neo-P selectivities lie in the range 1.2- 3.4.

Figure 51 presents the CBMC simulation results for adsorption of pentanes in MOF-177 at 433 K. The nC5/2MB and 2MB/neo-P selectivities lie in the range 1- 2.8.

Figure 52 presents the CBMC simulation results for adsorption of pentanes in Zn(bdc)dabco at 433 K. Note that the pure component isotherms were not determined in this case. The nC5/2MB and 2MB/neo-P selectivities lie in the range 0.8 - 8.

Figure 53 presents the CBMC simulation results of Dubbeldam et al.[2] for adsorption of pentanes in ZIF-77 at 433 K. The nC5/2MB selectivity lies in the range 10 – 15. The 2MB/neo-P selectivity lies in the range 300-1000.

Figure 54 presents the CBMC simulation data of Dubbeldam et al.[2] for adsorption of hexanes in ZIF-77 at 433 K. The CBMC simulation data (symbols) for adsorption of 5-component hexanes: nC6/2MP/3MP/22DMB/23DMB in ZIF-77 are in excellent agreement with IAST calculations using the unary isotherm fits.

Figure 55 presents the CBMC simulation data of Dubbeldam et al.[2] for adsorption of heptanes in ZIF-77 at 433 K. The CBMC simulation data (symbols) for adsorption of 5-component hexanes: : nC7/2MH/3MH/22DMP/23DMP in ZIF-77 are in excellent agreement with IAST calculations using the unary isotherm fits.

Figure 56 presents the data on adsorption of nC5 and 2MB in ZIF-8; the unary isotherms are determined from the experimental data of Zhang et al.,[30] measured at 308 K, 343 K and 373 K. The data were fitted with T-dependent single-site Langmuir model; the parameters are specified in Table 17. (a) The isotherm fits were used to calculate the unary isotherms of nC5 and 2MB at 433 K. Figure 56b shows IAST calculations of the component loadings for equimolar nC5/2MB mixtures at 433 K. The IAST calculations for nC5/2MB selectivity as a function of the total hydrocarbons pressure are shown in Figure 56c.

7. Comparison of adsorption selectivities and uptake capacities

Figure 57a compares the nC5/2MB adsorption selectivity for the 12 different materials investigated. The highest selectivity is realized with $Fe_2(BDP)_3$, followed by ZIF-77, MFI, and ZIF-8. With the 8 other MOFs, the selectivities are only in the range of 1-1.4; these MOFs are unlikely to be effective in this separation task. For 2MB/neo-P separations (cf. Figure 57b), the highest selectivities are realized

with ZIF-77 and Fe$_2$(BDP)$_3$; the selectivities for other materials are about an order-of-magnitude lower. The characteristic pore size of ZIF-77 is 4.5 Å, significantly smaller than the 4.9 Å sized triangular channels of Fe$_2$(BDP)$_3$; consequently, the neo-P is practically excluded from the pore channels of ZIF-77.[2]

Besides adsorption selectivity, separations in fixed bed adsorbers is also dictated by uptake capacities. Figure 58 compares the uptake capacities of (a) nC5, and (b) 2MB for the promising adsorbent materials. The nC5 uptake capacity of Fe$_2$(BDP)$_3$ is highest, but MFI has the highest uptake capacity for 2MB.

In order to take proper account of both selectivity and capacity, we undertake transient breakthrough simulations in fixed bed adsorbers.

8. Simulation methodology for transient breakthrough in fixed bed adsorbers

Fixed beds, packed with crystals of microporous materials, are commonly used for separation of mixtures (see schematic in Figure 59); such adsorbers are commonly operated in a transient mode, and the compositions of the gas phase, and component loadings within the crystals, vary with position and time. During the initial stages of the transience, the pores are loaded up gradually, and only towards the end of the adsorption cycle are conditions corresponding to pore saturation attained. Put another way, separations in fixed bed adsorbers are influenced by both the Henry regime of adsorption as well as the conditions corresponding to pore saturation. For a given separation task, transient breakthroughs provide more a realistic evaluation of the efficacy of a material, as they reflect the combined influence of adsorption selectivity, and adsorption capacity.[31, 32]

We describe below the simulation methodology used to perform transient breakthrough calculations that are presented in this work. This simulation methodology is the same as that used in our previous published works. [31, 32]

Assuming plug flow of an n-component gas mixture through a fixed bed maintained under isothermal conditions, the partial pressures in the gas phase at any position and instant of time are obtained by solving the following set of partial differential equations for each of the species i in the gas mixture.[33]

$$\frac{1}{RT}\frac{\partial p_i(t,z)}{\partial t} = -\frac{1}{RT}\frac{\partial(v(t,z)p_i(t,z))}{\partial z} - \frac{(1-\varepsilon)}{\varepsilon}\rho\frac{\partial \overline{q}_i(t,z)}{\partial t}; \quad i = 1,2,...n \qquad (3)$$

In equation (3), t is the time, z is the distance along the adsorber, ρ is the framework density, ε is the bed voidage, v is the interstitial gas velocity, and $\overline{q}_i(t,z)$ is the *spatially averaged* molar loading within the crystallites of radius r_c, monitored at position z, and at time t.

At any time t, during the transient approach to thermodynamic equilibrium, the spatially averaged molar loading within the crystallite r_c is obtained by integration of the radial loading profile

$$\overline{q}_i(t) = \frac{3}{r_c^3}\int_0^{r_c} q_i(r,t)r^2 dr \qquad (4)$$

For transient unary uptake within a crystal at any position and time with the fixed bed, the radial distribution of molar loadings, q_i, within a spherical crystallite, of radius r_c, is obtained from a solution of a set of differential equations describing the uptake

$$\frac{\partial q_i(r,t)}{\partial t} = -\frac{1}{\rho}\frac{1}{r^2}\frac{\partial}{\partial r}\left(r^2 N_i\right) \qquad (5)$$

The molar flux N_i of component i is described by the simplified version of the Maxwell-Stefan equations in which both correlation effects and thermodynamic coupling effects are considered to be of negligible importance[31]

$$N_i = -\rho Đ_i \frac{\partial q_i}{\partial r} \qquad (6)$$

Summing equation (**4**) over all n species in the mixture allows calculation of the *total average* molar loading of the mixture within the crystallite

$$\bar{q}_t(t,z) = \sum_{i=1}^{n} \bar{q}_i(t,z) \qquad (7)$$

The *interstitial* gas velocity is related to the *superficial* gas velocity by

$$v = \frac{u}{\varepsilon} \qquad (8)$$

In industrial practice, the most common operation is with to use a step-wise input of mixtures to be separation into an adsorber bed that is initially free of adsorbates, i.e. we have the initial condition

$$t = 0; \quad q_i(0,z) = 0 \qquad (9)$$

At time, $t = 0$, the inlet to the adsorber, $z = 0$, is subjected to a step input of the *n*-component gas mixture and this step input is maintained till the end of the adsorption cycle when steady-state conditions are reached.

$$t \geq 0; \quad p_i(0,t) = p_{i0}; \quad u(0,t) = u \qquad (10)$$

where u is the superficial gas velocity at the inlet to the adsorber.

Besides, the breakthrough simulations with a step-input (10), we also carried out simulations for a packed bed adsorber with injection of a short duration pulse of the mixture to be separated. This type of simulation is particularly useful to demonstrate the fractionating capability of adsorbents. For simulation of pulse chromatographic separations, we use the corresponding set of inlet conditions

$$0 \leq t \leq t_0; \quad p_i(0,t) = p_{i0}; \quad u(0,t) = u \qquad (11)$$

where the time for duration of the pulse is t_0. Pulse chromatographic simulations and experiments are representative of separations in the Henry regime at low pore occupancies.[34, 35]

If the value of $\dfrac{Ð_i}{r_c^2}$ is large enough to ensure that intra-crystalline gradients are absent and the entire crystallite particle can be considered to be in thermodynamic equilibrium with the surrounding bulk gas phase at that time t, and position z of the adsorber

$$\bar{q}_i(t,z) = q_i(t,z) \tag{12}$$

The molar loadings at the *outer surface* of the crystallites, i.e. at $r = r_c$, are calculated on the basis of adsorption equilibrium with the bulk gas phase partial pressures p_i at that position z and time t. The adsorption equilibrium can be calculated on the basis of the Ideal Adsorbed Solution Theory (IAST) of Myers and Prausnitz.[29] In all the simulation results we present in this article, the IAST calculations use pure component isotherms fitted with dual-site Langmuir-Freundlich model. For all the simulations presented in this article, the diffusional effects are considered to be negligible.

For presenting the breakthrough simulation results, we use the dimensionless time, $\tau = \dfrac{tu}{L\varepsilon}$, obtained by dividing the actual time, t, by the characteristic time, $\dfrac{L\varepsilon}{u}$, where L is the length of adsorber, u is the superficial fluid velocity, ε is the bed voidage.[36]

For all the simulations reported in this article we choose the following: adsorber length, $L = 0.3$ m; cross-sectional area, $A = 1$ m^2; superficial gas velocity in the bed, $u = 0.04$ m s^{-1}; voidage of the packed bed, $\varepsilon = 0.4$. Please note that since the superficial gas velocity is specified, the specification of the cross-sectional area of the tube, A, is not relevant in the simulation results presented. The volume of MOF used in the simulations is $(1 - \varepsilon) A L = 0.18$ m^3. If ρ is the framework density, the mass of the adsorbent in the bed is $\rho (1 - \varepsilon) A L$ kg. In these breakthrough simulations we use the same volume of adsorbent in the breakthrough apparatus, i.e. $(1 - \varepsilon) A L = 0.18$ m^3 = 180 L.

In all the pulse chromatographic simulations presented in this article the duration of the pulse $t_0 = 10$ s.

9. Comparison of nC5/2MB separations in fixed bed adsorbers packed with MOFs

For quantitative comparison of the nC5/2MB separation performance in fixed bed adsorbers, Figure 60a presents transient nC5(1)/2MB(2) breakthroughs comparing four different adsorbents ZIF-77, MFI,

Fe$_2$(BDP)$_3$, and ZIF-8. The dimensionless concentration of nC5 and 2MB, normalized with respect to the molar concentrations at the adsorber inleter, are plotted against the dimensionless time, $\tau = \dfrac{tu}{L\varepsilon}$.

In all cases, the linear nC5 is more strongly adsorbed and is the component that elutes last; the less strongly adsorbed branched isomer 2MB breaks through earlier. There is a finite time interval, $\Delta\tau$, during which pure 2MB can be recovered for incorporation into the gasoline pool; the larger value of $\Delta\tau$, the higher is the productivity of pure 2MB. We assume that we aim for 99% purity of 2MB. The best adsorbent is the material that yields the longest breakthrough time for nC5, and also the larger value of $\Delta\tau$. In Figure 60b, the difference in the dimensionless breakthrough times between nC5 and 2MB, $\Delta\tau$, is plotted against the dimensionless breakthrough time of nC5. From a material balance on the adsorber, we determine the productivity of 99% pure22MB per L of adsorbent in the fixed bed. The values of the 99% pure 2MB productivity are: Fe$_2$(BDP)$_3$ = 1.87, ZIF-77 = 0.98, MFI = 0.56, ZIF-8 = 0.52 mol L^{-1}. The 2MB productivity of Fe$_2$(BDP)$_3$ is the highest, a factor 2 higher than that of ZIF-77.

The windows of ZIF-8 are about 3.3 Å, and therefore diffusion effects are likely to significantly influence the transient breakthroughs in fixed-bed adsorbers. In order to determine the influence of intra-crystalline diffusion on the productivity of 99% pure 2MB, simulations were undertaken with inclusion of intra-crystalline diffusion limitations. The diffusivity values used in the simulations are $Đ_{nC5}/r_c^2 = 2.5 \times 10^{-5}$ s^{-1}; $Đ_{2NB}/r_c^2 = 5 \times 10^{-5}$ s^{-1}; $Đ_{nC5}/Đ_{2MB} = 50$. The chosen diffusivity values are based on our earlier publication[31] which contains a thorough re-analysis of the experimental data of Peralta et al.[37] for breakthrough of hexane isomers in an adsorber packed with ZIF-8. Figure 61 compares the two sets of simulations, with and without diffusional influences. Inclusion of intra-crystalline diffusion effects leads to distended breakthroughs. From a material balance on the adsorber, the productivity of 99% pure 2MB is determined to be 0.44 mol L^{-1}, only 15% lower than the value of 0.52 mol L^{-1}, obtained with the assumption of negligible diffusion limitations.

10. Comparison of 2MB/neo-P separations in fixed bed adsorbers packed with MOFs

The results for transient 2MB(1)/neo-P(2) breakthroughs in fixed bed adsorbers packed with ZIF-77, MFI, and $Fe_2(BDP)_3$, are presented in Figure 62. We assume that we aim for 99% purity of neo-P. The values of the 99% pure neo-P productivity are: $Fe_2(BDP)_3$ = 1.36, ZIF-77 = 0.56, MFI = 0.05 mol L^{-1}. The neo-P productivity of $Fe_2(BDP)_3$ is the highest, a factor 2.5 times higher than that of ZIF-77.

11. The separation step of the alkane isomerization process

Isomerization of alkanes, for the purposes of octane improvement, is a process of importance in the petroleum industry.[2, 4, 37-39] Figure 63 shows an example of a process for isomerization of a feed mixture of C5, C6, and C7 hydrocarbons. The product from the isomerization reactor, that commonly uses zeolite MOR as catalyst, consists of an equilibrium distribution of C5 isomers (nC5, 2MB, neo-P), C6 isomers (n-hexane (nC6), 2-methylpentane (2MP), 3-methylpentane (3MP), 2,2-dimethylbutane (22DMB), 2,3-dimethylbutane (23DMB)), and C7 isomers (n-heptane (nC7), 2-methylhexane (2MH), 3-methylhexane (3MH), 2,2-dimethylpentane (22DMP), 2,3-dimethylpentane (23DMP)). In current industrial practice the linear isomers nC5, nC6, and nC7 is separated from the mono-branched, and di-branched isomers in an adsorption separation step that relies on molecular sieving.[39] The adsorbent is LTA-5A that consists of cages separated by 4.1 Å sized windows. The windows only allow the diffusion and adsorption of the linear isomer, and the mono-branched and di-branched isomers are rejected and removed as product. The linear isomers nC5, nC6, and nC7 are recycled back to the isomerization reactor.

The values of the Research Octane Number (RON) increases with the degree of branching; Table 1 lists the Research Octane Numbers (RON) of C5, C6, and C7 alkanes.[4] The di-branched isomers (neo-P, 22DMB, 23DMB, 22DMP, 23DMP) have significantly higher RON values than that of the linear isomers (nC5, nC6, and nC7), and mon-branched isomers (2MB, 2MP, 3MP, 2MH, 3MH). Therefore, di-branched isomers are preferred products for incorporation into the high-octane gasoline pool.

An improved process would require the recycle of both linear and mono-branched isomers to the reactor; see Figure 64. Typically, in such a processing scheme the aim would be to produce a product stream from the separation step with RON value of 92. The separation of neo-P, 22DMB, 23DMB, 22DMP, 23DMP from the remaining isomers is a difficult task because it requires distinguishing molecules on the *degree* of branching. This requirement of 92+ RON implies that the product stream will contain predominantly the mono-branched isomers into the product stream. Sharp separations between mono- and di- branched isomers is not a strict requirement, but does help the performance of pressure swing adsorption (PSA) units.

We now compare the performance of $Fe_2(BDP)_3$ with those of ZIF-77, and MFI for use as adsorbent in the separation step in Figure 64. Towards this end, we consider the following mixtures:

(1) 3-component pentanes nC5/2MB/neo-P mixture, with equal partial fugacities f_i = 30 kPa at 433 K.

(2) 5-component hexanes nC6/2MP/3MP/22DMB/23DMB mixture, with equal partial fugacities f_i = 20 kPa at 433 K.

(3) 8-component nC5/2MB/neoP/nC6/2MP/3MP/22DMB/23DMB mixture, with equal partial fugacities f_i = 20 kPa at 433 K.

(4) 13-component pentanes/hexanes/heptanes mixture: nC5/2MB/neoP/nC6/2MP/3MP/22DMB/23DMB/nC7/2MH/3MH/22DMP/23DMP, with equal partial fugacities f_i = 20 kPa at 433 K.

(5) 5-component heptanes nC7/2MH/3MH/22DMP/23DMP mixture, with equal partial fugacities f_i = 20 kPa at 433 K.

12. Separation of nC5/2MB/neo-P isomers using $Fe_2(BDP)_3$, MFI, and ZIF-77

Figures 65a,b,c present the transient breakthrough of nC5(1)/2MB(2)/neo-P(3) mixture in fixed bed adsorbers packed with (a) $Fe_2(BDP)_3$, (b) ZIF-77, and (c) MFI zeolite operating at 433 K. The partial fugacities in the feed nC5(1)/2MB(2)/neo-P(3) mixture at the inlet, $f_1 = f_2 = f_3$ = 30 kPa. The dimensionless concentration of nC5, 2MB and neo-P, normalized with respect to the molar concentrations at the adsorber inlet, are plotted against the dimensionless time. In all simulations

presented here, the total volume of adsorbent in the fixed bed is 0.18 m^3 = 180 L. For each adsorbent, the RON of the mixture exiting the fixed bed is calculated from the pure component RON values in Table 1. The RON calculations are based a linear mixing rule using the mole fractions in the product gas; no non-linear mixing rules are applied. Figure 65d presents plots of the product RON as a function of the dimensionless time, $\tau = \dfrac{tu}{L\varepsilon}$. For incorporation into the gasoline pool, a reasonable target RON value is 92+ has been set in the work of Herm et al. for separation of hexane isomers;[4] this threshold value of 92+ is retained in our analysis of C5 isomer separation. From a material balance on the fixed bed adsorber we can calculate the amount, in moles, of 92+ RON product gas that can be recovered per L of adsorbent in the bed. The 92+ RON productivity values are: Fe$_2$(BDP)$_3$ = 3.88, ZIF-77 = 1.92, and MFI = 0.96 mol L^{-1}. The 92+ RON productivity of Fe$_2$(BDP)$_3$ is the highest, a factor 2 higher than that of ZIF-77.

13. Separation of hexane isomers using Fe$_2$(BDP)$_3$, MFI, and ZIF-77

Figure 66a presents transient breakthrough of nC6/2MP/3MP/22DMB/23DMB mixture, with step-input, in fixed bed adsorbers packed with Fe$_2$(BDP)$_3$. The partial fugacities in the feed gas nC6/2MP/3MP/22DMB/23DMB mixture at the inlet, $f_1 = f_2 = f_3 = f_4 = f_5 = 20$ kPa. Similar simulations were also carried out for adsorbers packed with ZIF-7 and MFI. Using the same calculation procedure described in the foregoing section, Figure 66b compares the RON of the product gas mixture at the adsorber outlet as a function of the dimensionless time. The 92+ RON productivity values are: Fe$_2$(BDP)$_3$ = 1.19, ZIF-77 = 0.53, and MFI = 0.12 mol L^{-1}. The 92+ RON productivity of Fe$_2$(BDP)$_3$ is the highest, a factor 2 higher than that of ZIF-77.

14. Separation of C5/C6 mixtures using Fe$_2$(BDP)$_3$, MFI, and ZIF-77

Figure 67a presents transient breakthrough of 8-component pentanes/hexanes mixture: nC5/2MB/neoP/nC6/2MP/3MP/22DMB/23DMB, with step-input, in fixed bed adsorbers packed with Fe$_2$(BDP)$_3$. Similar simulations were also carried out for adsorbers packed with ZIF-7 and MFI. Figure 67b compares the RON of the product gas mixture at the adsorber outlet as a function of the

dimensionless time. The 92+ RON productivity values are: $Fe_2(BDP)_3 = 1.63$, ZIF-77 = 0.57, and MFI = 0.26 mol L^{-1}. The 92+ RON productivity of $Fe_2(BDP)_3$ is the highest, a factor 3 higher than that of ZIF-77.

15. Separation of C5/C6/C7 mixtures using $Fe_2(BDP)_3$, and ZIF-77

Figure 68a presents transient breakthrough of 13-component pentanes/hexanes/heptanes nC5/2MB/neoP/nC6/2MP/3MP/22DMB/23DMB/nC7/2MH/3MH/22DMP/23DMP

mixture, with step-input, in fixed bed adsorbers packed with $Fe_2(BDP)_3$. Similar simulations were also carried out for adsorbers packed with ZIF-7. Figure 68b compares the RON of the product gas mixture at the adsorber outlet as a function of the dimensionless time. The 92+ RON productivity values are: $Fe_2(BDP)_3 = 1.42$, and ZIF-77 = 0.66 mol L^{-1}. The 92+ RON productivity of $Fe_2(BDP)_3$ is the highest, a factor 2.5 higher than that of ZIF-77.

16.Fractionation of C5/C6/C7 mixtures using $Fe_2(BDP)_3$ adsorbent

$Fe_2(BDP)_3$ is capable of separating a ternary nC5(1)/2MB(2)/neo-P(3) mixture to yield three different, nearly-pure fractions. In order to demonstrate this, Figures 69 presents pulse chromatographic simulations in fixed bed operating at 433 K. The pulse chromatographic simulations demonstrates the capability of $Fe_2(BDP)_3$ to separate pentane isomers to yield three different fractions, with different degrees of branching. The fractionating capability of $Fe_2(BDP)_3$ also holds for 5-component mixture of hexane isomers (cf. Figure 70a) and 5-component mixture of heptane isomers (cf. Figure 70b). In both cases, feed mixture can be separated to yield three different fractions, with different degree of branching.

Figure 71 presents pulse chromatographic simulation of 8-component pentanes/hexanes mixture: nC5/2MB/neoP/nC6/2MP/3MP/22DMB/23DMB in fixed bed adsorber packed with $Fe_2(BDP)_3$ and operating at 433 K. The C5/C6 feed mixture can be separated into three different fractions, with different degrees of branching.

Figure 72 presents the pulse chromatographic simulation results for separation of 13-component pentanes/hexanes/heptanes mixture:

nC5/2MB/neoP/nC6/2MP/3MP/22DMB/23DMB/nC7/2MH/3MH/22DMP/23DMP

The separation into three fractions based on degree of branching, rather than on C numbers, is evident.

17. Notation

A	cross-sectional area of breakthrough tube, m^2
b_A	dual-Langmuir-Freundlich constant for species i at adsorption site A, $Pa^{-\nu_A}$
b_B	dual-Langmuir-Freundlich constant for species i at adsorption site B, $Pa^{-\nu_B}$
c_i	molar concentration of species i in gas mixture, mol m^{-3}
c_{i0}	molar concentration of species i in gas mixture at inlet to adsorber, mol m^{-3}
$Đ_i$	Maxwell-Stefan diffusivity, m^2 s^{-1}
f_i	partial fugacity of species i, Pa
f_t	total fugacity of bulk fluid mixture, Pa
k_B	Boltzmann constant, 1.38×10^{-23} J molecule^{-1} K^{-1}
L	length of packed bed adsorber, m
n	number of species in the mixture, dimensionless
N_i	molar flux of species i, mol m^{-2} s^{-1}
p_i	partial pressure of species i in mixture, Pa
p_t	total system pressure, Pa
q_i	component molar loading of species i, mol kg^{-1}
$q_{i,sat}$	molar loading of species i at saturation, mol kg^{-1}
q_t	total molar loading in mixture, mol kg^{-1}
$q_{sat,A}$	saturation loading of site A, mol kg^{-1}
$q_{sat,B}$	saturation loading of site B, mol kg^{-1}
r	radial direction coordinate, m
r_c	radius of crystallite, m
R	gas constant, 8.314 J mol^{-1} K^{-1}
t	time, s
T	absolute temperature, K
u	superficial gas velocity in packed bed, m s^{-1}
v	interstitial gas velocity in packed bed, m s^{-1}

| z | distance along the adsorber, and along membrane layer, m |

Greek letters

ε	voidage of packed bed, dimensionless
ε	Lennard-Jones interaction energy parameter, J molecule^{-1}
Θ_i	loading of species i, molecules per unit cell
$\Theta_{i,sat}$	saturation loading of species i, molecules per unit cell
Θ_t	total molar loading of mixture, molecules per unit cell
μ_i	molar chemical potential, J mol^{-1}
ν	exponent in dual-Langmuir-Freundlich isotherm, dimensionless
ρ	framework density, kg m^{-3}
σ	Lennard-Jones size parameter, m
τ	time, dimensionless

Subscripts

A	referring to site A
B	referring to site B
i	referring to component i
t	referring to total mixture

18.   References

(1) Dubbeldam, D.; Calero, S.; Vlugt, T. J. H.; Krishna, R.; Maesen, T. L. M.; Smit, B. United Atom Forcefield for Alkanes in Nanoporous Materials. *J. Phys. Chem. B* **2004**, *108*, 12301-12313.

(2) Dubbeldam, D.; Krishna, R.; Calero, S.; Yazaydın, A. Ö. Computer-Assisted Screening of Ordered Crystalline Nanoporous Adsorbents for Separation of Alkane Isomers. *Angew. Chem. Int. Ed.* **2012**, *51*, 11867-11871.

(3) Krishna, R.; van Baten, J. M. In silico screening of metal-organic frameworks in separation applications. *Phys. Chem. Chem. Phys.* **2011**, *13*, 10593-10616.

(4) Herm, Z. R.; Wiers, B. M.; Van Baten, J. M.; Hudson, M. R.; Zajdel, P.; Brown, C. M.; Maschiocchi, N.; Krishna, R.; Long, J. R. Separation of Hexane Isomers in a Metal-Organic Framework with Triangular Channels *Science* **2013**, *340*, 960-964.

(5) Vlugt, T. J. H.; Krishna, R.; Smit, B. Molecular Simulations of Adsorption Isotherms for Linear and Branched Alkanes and Their Mixtures in Silicalite. *J. Phys. Chem. B* **1999**, *103*, 1102-1118.

(6) Krishna, R.; van Baten, J. M. Screening of zeolite adsorbents for separation of hexane isomers: A molecular simulation study. *Sep. Purif. Technol.* **2007**, *55*, 246-255.

(7) Rappé, A. K.; Casewit, C. J.; Colwel, K. S.; Goddard, W. A.; Skiff, W. M. UFF, A Full Periodic Table Force Field for Molecular Mechanics and Molecular Dynamics Simulations. *J. Am. Chem. Soc.* **1992**, *114*, 10024-10035.

(8) Mayo, S. L.; Olafson, B. D.; Goddard, W. A. DREIDING: A Generic Force Field for Molecular Simulations. *J. Phys. Chem.* **1990**, *94*, 8897-8909.

(9) Krishna, R.; van Baten, J. M. A molecular simulation study of commensurate – incommensurate adsorption of n-alkanes in cobalt formate frameworks. *Molecular Simulation* **2009**, *35*, 1098-1104.

(10) Vlugt, T. J. H. BIGMAC. http://molsim.chem.uva.nl/bigmac/, University of Amsterdam, 1 November 2000.

(11) Karavias, F.; Myers, A. L. Isosteric Heats of Multicomponent Adsorption: Thermodynamics and Computer Simulations. *Langmuir* **1991**, *7*, 3118-3126.

(12) Baerlocher, C.; McCusker, L. B. Database of Zeolite Structures. http://www.iza-structure.org/databases/, International Zeolite Association, 10 January 2002.

(13) Sumida, K.; Hill, M. R.; Horike, S.; Dailly, A.; Long, J. R. Synthesis and Hydrogen Storage Properties of $Be_{12}(OH)_{12}$(1,3,5-benzenetribenzoate)$_4$. *J. Am. Chem. Soc.* **2009**, *131*, 15120-15121.

(14) Choi, H. J.; Dincă, M.; Long, J. R. Broadly Hysteretic H_2 Adsorption in the Microporous Metal-Organic Framework Co(1,4-benzenedipyrazolate). *J. Am. Chem. Soc.* **2008**, *130*, 7848-7850.

(15) Salles, F.; Maurin, G.; Serre, C.; Llewellyn, P. L.; Knöfel, C.; Choi, H. J.; Filinchuk, Y.; Oliviero, L.; Vimont, A.; Long, J. R.; Férey, G. Multistep N_2 Breathing in the Metal-Organic Framework Co(1,4-benzenedipyrazolate). *J. Am. Chem. Soc.* **2010**, *132*, 13782-13788.

(16) Demessence, A.; D'Alessandro, D. M.; Foo, M. W.; Long, J. R. Strong CO_2 Binding in a Water-Stable, Triazolate-Bridged Metal-Organic Framework Functionalized with Ethylenediamine. *J. Am. Chem. Soc.* **2009**, *131*, 8784-8786.

(17) Dubbeldam, D.; Walton, K. S.; Ellis, D. E.; Snurr, R. Q. Exceptional Negative Thermal Expansion in Isoreticular Metal–Organic Frameworks. *Angew. Chem. Int. Ed.* **2007**, *46*, 4496-4499.

(18) Dubbeldam, D.; Frost, H.; Walton, K. S.; Snurr, R. Q. Molecular simulation of adsorption sites of light gases in the metal-organic framework IRMOF-1. *Fluid Phase Equilib.* **2007**, *261*, 152-161.

(19) Britt, D.; Furukawa, H.; Wang, B.; Glover, T. G.; Yaghi, O. M. Highly efficient separation of carbon dioxide by a metal-organic framework replete with open metal sites. *Proc. Natl. Acad. Sci. U.S.A.* **2009**, *106*, 20637-20640.

(20) Rosi, N. L.; Kim, J.; Eddaoudi, M.; Chen, B.; O'Keeffe, M.; Yaghi, O. M. Rod Packings and Metal-Organic Frameworks Constructed from Rod-Shaped Secondary Building Units. *J. Am. Chem. Soc.* **2005**, *127*, 1504-1518.

(21) Dietzel, P. D. C.; Panella, B.; Hirscher, M.; Blom, R.; Fjellvåg, H. Hydrogen adsorption in a nickel based coordination polymer with open metal sites in the cylindrical cavities of the desolvated framework. *Chem. Commun.* **2006**, 959-961.

(22) Dietzel, P. D. C.; Besikiotis, V.; Blom, R. Application of metal–organic frameworks with coordinatively unsaturated metal sites in storage and separation of methane and carbon dioxide. *J. Mater. Chem.* **2009**, *19*, 7362-7370.

(23) Caskey, S. R.; Wong-Foy, A. G.; Matzger, A. J. Dramatic Tuning of Carbon Dioxide Uptake via Metal Substitution in a Coordination Polymer with Cylindrical Pores. *J. Am. Chem. Soc.* **2008**, *130*, 10870-10871.

(24) Yazaydın, A. Ö.; Snurr, R. Q.; Park, T. H.; Koh, K.; Liu, J.; LeVan, M. D.; Benin, A. I.; Jakubczak, P.; Lanuza, M.; Galloway, D. B.; Low, J. J.; Willis, R. R. Screening of Metal-Organic Frameworks for Carbon Dioxide Capture from Flue Gas using a Combined Experimental and Modeling Approach. *J. Am. Chem. Soc.* **2009**, *131*, 18198-18199.

(25) Chae, H. K.; Siberio-Pérez, D. Y.; Kim, J.; Go, Y. B.; Eddaoudi, M.; Matzger, A. J.; O'Keeffe, M.; Yaghi, O. M. A route to high surface area, porosity and inclusion of large molecules in crystals. *Nature* **2004**, *427*, 523-527.

(26) Bárcia, P. S.; Zapata, F.; Silva, J. A. C.; Rodrigues, A. E.; Chen, B. Kinetic Separation of Hexane Isomers by Fixed-Bed Adsorption with a Microporous Metal-Organic Framework. *J. Phys. Chem. B* **2008**, *111*, 6101-6103.

(27) Lee, J. Y.; Olson, D. H.; Pan, L.; Emge, T. J.; Li, J. Microporous Metal–Organic Frameworks with High Gas Sorption and Separation Capacity. *Adv. Funct. Mater.* **2007**, *17*, 1255-1262.

(28) Banerjee, R.; Phan, A.; Wang, B.; Knobler, C.; Furukawa, H.; O'Keeffe, M.; Yaghi, O. M. High-Throughput Synthesis of Zeolitic Imidazolate Frameworks and Application to CO_2 Capture. *Science* **2008**, *319*, 939-943.

(29) Myers, A. L.; Prausnitz, J. M. Thermodynamics of Mixed Gas Adsorption. *A.I.Ch.E.J.* **1965**, *11*, 121-130.

(30) Zhang, L.; Qian, G.; Liu, Z.; Cui, Q.; Wang, h.; Yao., H. Adsorption and Separation Properties of N-pentane/Isopentane on ZIF-8. *Sep. Purif. Technol.* **2015**, *156*, 472-479.

(31) Krishna, R. The Maxwell-Stefan Description of Mixture Diffusion in Nanoporous Crystalline Materials. *Microporous Mesoporous Mater.* **2014**, *185*, 30-50.

(32) Krishna, R. Methodologies for Evaluation of Metal-Organic Frameworks in Separation Applications. *RSC Adv.* **2015**, *5*, 52269-52295.

(33) Krishna, R.; Baur, R. Modelling Issues in Zeolite Based Separation Processes. *Sep. Purif. Technol.* **2003**, *33*, 213-254.

(34) Krishna, R. Separating Mixtures by Exploiting Molecular Packing Effects in Microporous Materials. *Phys. Chem. Chem. Phys.* **2015**, *17*, 39-59.

(35) Gu, Z.-Y.; Yang, C.-X.; Chang, N.; Yan, X.-P. Metal-Organic Frameworks for Analytical Chemistry: From Sample Collection to Chromatographic Separation. *Acc. Chem. Res.* **2012**, *45*, 734-745.

(36) Krishna, R.; Long, J. R. Screening metal-organic frameworks by analysis of transient breakthrough of gas mixtures in a fixed bed adsorber. *J. Phys. Chem. C* **2011**, *115*, 12941-12950.

(37) Peralta, D.; Chaplais, G.; Simon-Masseron, A.; Barthelet, K.; Pirngruber, G. D. Separation of C6 paraffins using Zeolitic Imidazolate Frameworks: comparison with zeolite 5A. *Ind. Eng. Chem. Res.* **2012**, *51*, 4692-4702.

(38) Krishna, R. Exploiting Configurational Entropy Effects for Separation of Hexane Isomers Using Silicalite-1. *Chem. Eng. Res. Des.* **2001**, *79*, 182-194.

(39) Vermeiren, W.; Gilson, J.-P. Impact of Zeolites on the Petroleum and Petrochemical Industry. *Top. Catal.* **2009**, *52*, 1131-1161.

(40) Walton, K. S.; Millward, A. R.; Dubbeldam, D.; Frost, H.; Low, J. J.; Yaghi, O. M.; Snurr, R. Q. Understanding Inflections and Steps in Carbon Dioxide Adsorption Isotherms in Metal-Organic Frameworks. *J. Am. Chem. Soc.* **2008**, *130*, 406-407.

(41) Xu, Q.; Zhong, C. A General Approach for Estimating Framework Charges in Metal-Organic Frameworks. *J. Phys. Chem. C* **2010**, *114*, 5035-5042.

(42) Schenk, M.; Vidal, S. L.; Vlugt, T. J. H.; Smit, B.; Krishna, R. Separation of alkane isomers by exploiting entropy effects during adsorption on silicalite-1: A configurational-bias Monte Carlo simulation study. *Langmuir* **2001**, *17*, 1558-1570.

(43) Calero, S.; Smit, B.; Krishna, R. Configurational entropy effects during sorption of hexane isomers in silicalite. *J. Catal.* **2001**, *202*, 395-401.

(44) Krishna, R.; Smit, B.; Calero, S. Entropy effects during sorption of alkanes in zeolites. *Chem. Soc. Rev.* **2002**, *31*, 185-194.

Table 1. Research Octane Numbers (RON) of C5, C6, and C7 alkanes. Information collected from a variety of web sources.

Alkane		Research Octane Number
Symbol	Chemical Name	(RON)
nC4	n-butane	94
iC4	iso-butane = 2-methyl propane	102
nC5	n-pentane	61.7
2MB	2-methyl butane	93.5
neoP	2,2 dimethyl propane	98
nC6	n-hexane	30
2MP	2-methyl pentane	74.5
3MP	3-methyl pentane	75.5
22DMB	2,2 dimethyl butane	94
23DMB	2,3 dimethyl butane	105
nC7	n-heptane	0
2MH	2-methyl hexane	42.4
3MH	3-methyl hexane	52
22DMP	2,2 dimethyl pentane	92.8
23DMP	2,3 dimethyl pentane	91.1

Table 2. Boiling points of alkane isomers.

Alkane		Boiling point
Symbol	Chemical Name	K
nC4	n-butane	263.1
iC4	iso-butane = 2-methyl propane	261.5
nC5	n-pentane	309
2MB	2-methyl butane	301
neo-P	2,2 dimethyl propane	282.5
nC6	n-hexane	341.5
2MP	2-methyl pentane	333.1
3MP	3-methyl pentane	336.5
22DMB	2,2 dimethyl butane	323.15
23DMB	2,3 dimethyl butane	331.2
nC7	n-heptane	371.5
2MH	2-methyl hexane	363.15
3MH	3-methyl hexane	365
22DMP	2,2 dimethyl pentane	352.15
23DMP	2,3 dimethyl pentane	362

Table 3. Lennard-Jones parameters for framework atoms of BeBTB

(pseudo-) atom	σ / Å	ε/k_B / K
Be	2.446	42.78
C	3.473	47.86
O	3.033	48.16
H	2.846	7.650

Table 4. Lennard-Jones parameters for framework atoms of Co(BDP)

(pseudo-) atom	σ / Å	ε/k_B / K
Co	2.559	7.046
C	3.473	47.86
H	2.846	7.650
N	3.263	38.95

Table 5. Lennard-Jones parameters for framework atoms of CuBTT

(pseudo-) atom	σ / Å	ε/k_B / K
Cl	3.519	142.58
Cu	3.114	2.516
C	3.473	47.86
H	2.846	7.650
N	3.263	38.95

Table 6. The alkane-alkane interactions were determined using the force field of Dubbeldam et al.[1] The metal-organic framework structure was considered to be rigid in the simulations. For the atoms in the $Fe_2(BDP)_3$, the generic UFF [7] and DREIDING [8] force fields were used to determine the Lennard-Jones parameters given below. The Lorentz-Berthelot mixing rules were applied for calculating for guest-host interactions.

(pseudo-) atom	σ / Å	ε/k_B / K
Fe	4.04	27.68
C	3.47	47.86
N	3.26	38.95
H	2.85	7.65
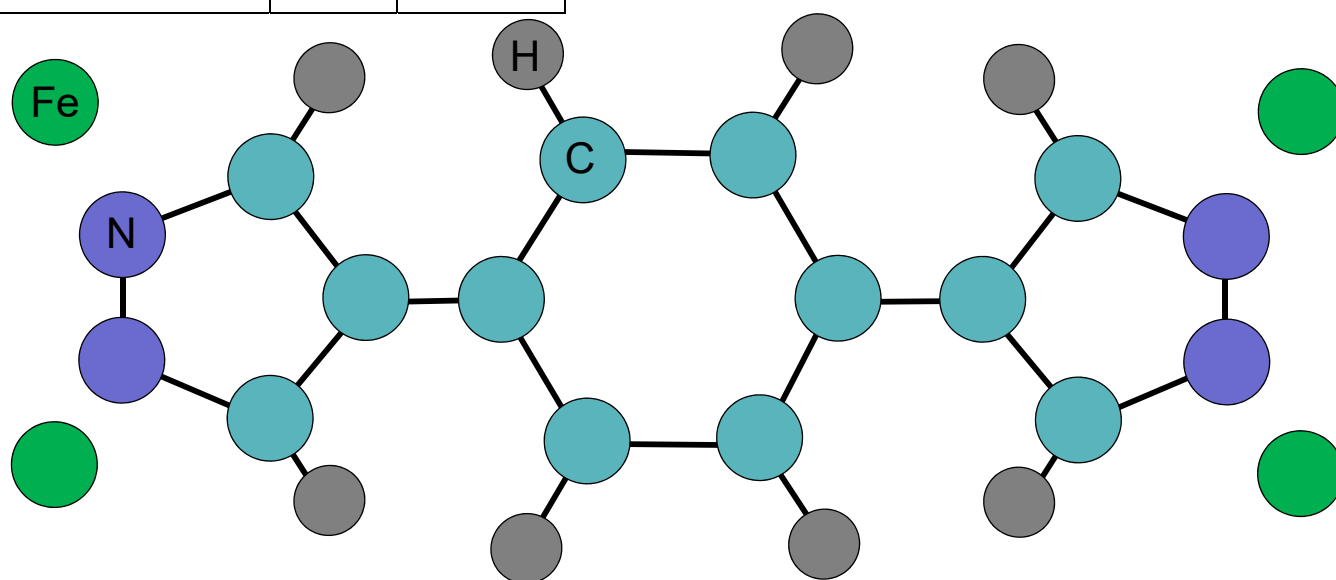
Table 7. Lennard-Jones parameters for atoms in IRMOF-1. The force field corresponds to that presented in the papers by Walton et al.[40] and Dubbeldam et al.[18].

(pseudo-) atom	σ / Å	ε/k_B / K	charge
Zn	2.69	0.41	1.275
Oa	2.98	700	-1.5
Ob	3.11	70.5	-0.6
Ca	3.74	47	0.475
Cb	3.47	47.9	0.125
Cc	3.47	47.9	-0.15
H	2.85	7.65	0.15

See Cartoon below for further explanation:

IRMOF-1
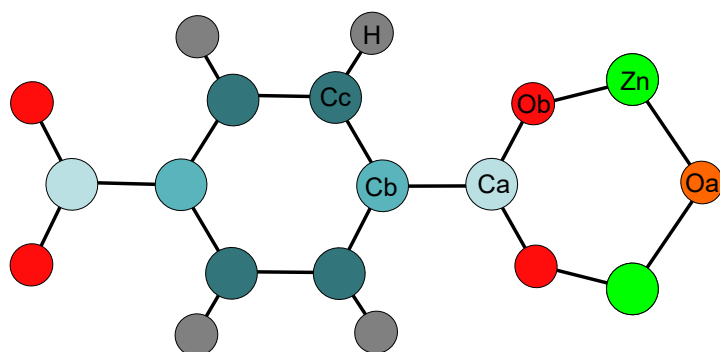
Table 8. Lennard-Jones parameters for atoms in MgMOF-74 based on the data from Yazaydin et al. [24].

(pseudo-) atom	σ / Å	ε/k_B / K	charge
Mg	2.691	55.86	1.458
OA	3.033	48.16	-0.909
OB	3.033	48.16	-0.714
OC	3.033	48.16	-0.784
CA	3.473	47.86	0.800
CB	3.473	47.86	-0.260
CC	3.473	47.86	0.492
CD	3.473	47.86	-0.280
H	2.846	7.650	0.197
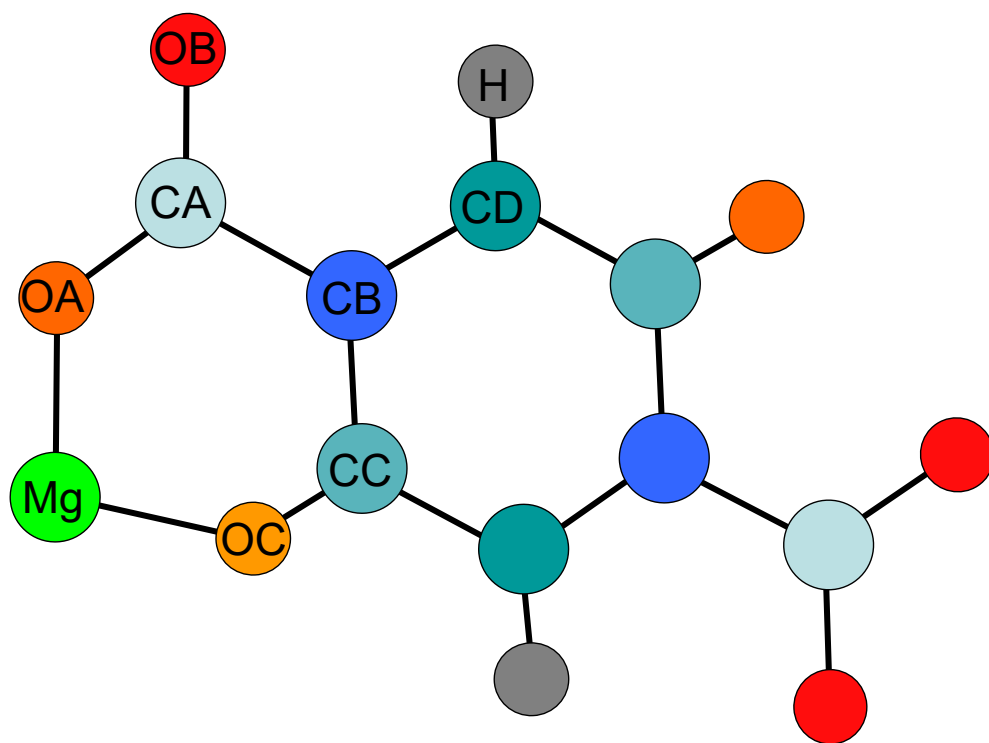
Table 9. Lennard-Jones parameters for atoms in ZnMOF-74 based on the data from Yazaydin et al[24].

(pseudo-) atom	σ / Å	ε/k_B / K	charge
Zn	4.045	27.68	1.206
OA	3.033	48.16	-0.670
OB	3.033	48.16	-0.659
OC	3.033	48.16	-0.702
CA	3.473	47.86	0.767
CB	3.473	47.86	-0.292
CC	3.473	47.86	0.325
CD	3.473	47.86	-0.147
H	2.846	7.650	0.172
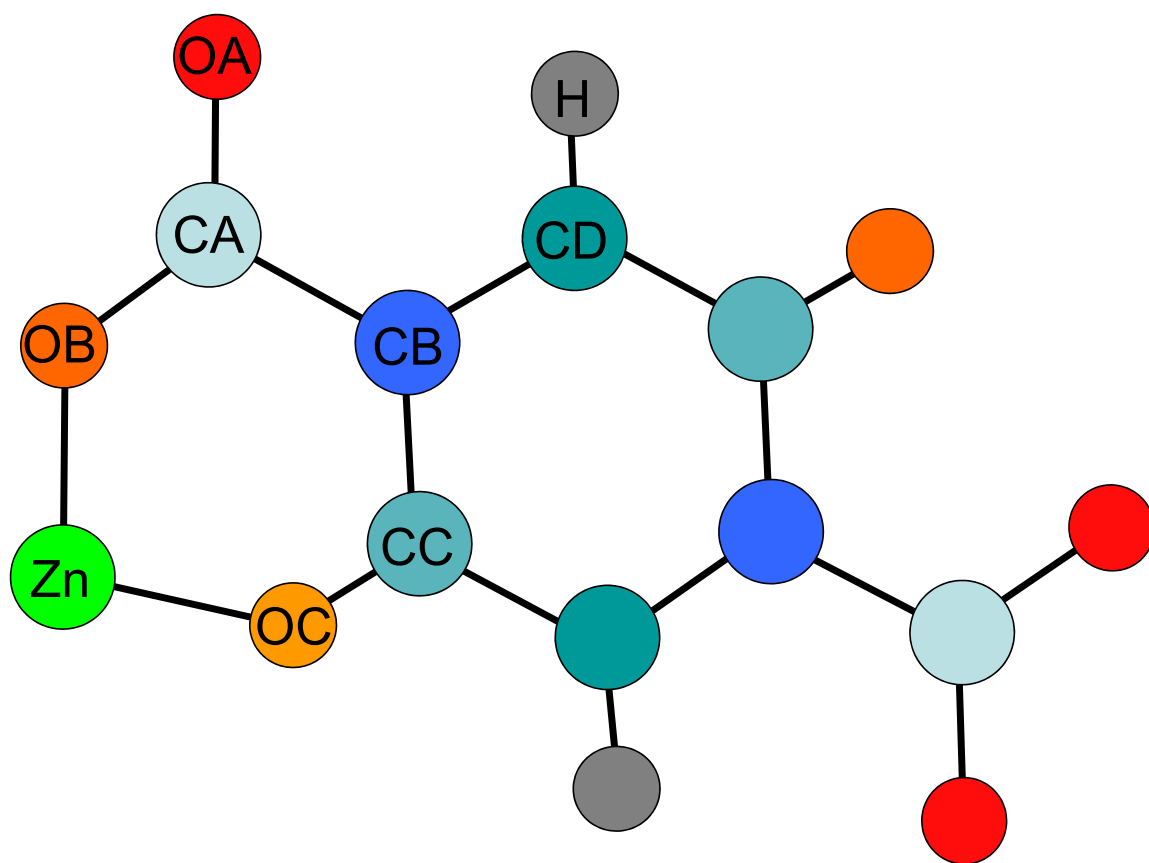
Table 10. Lennard-Jones parameters for the framework atoms of MOF-177. The framework charges of MOF-177 were estimated using the group-contribution procedure based on quantum mechanical calculations described by Xu and Zhong. [41]

(pseudo-) atom	σ / Å	ε/k_B / K	charge
CA	3.473	47.86	0.8056
CB	3.473	47.86	0.0496
CC	3.473	47.86	-0.1304
H	2.846	7.650	0.1086
OA	3.033	48.16	-1.9214
OB	3.033	48.16	-0.7934
Zn	4.044	27.68	1.5916
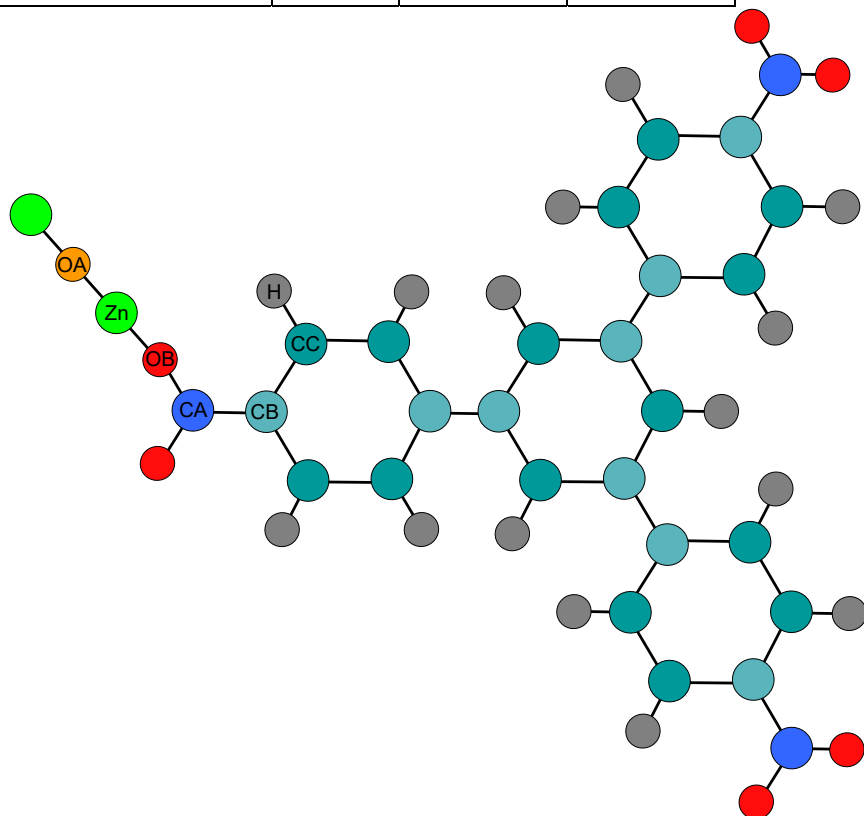
Table 11. Dual-site Langmuir-Freundlich parameters for pure component pentane and hexane isomers at 433 K in MFI zeolite. The fits are based on CBMC simulation data of Krishna and van Baten.[3]

$\Theta = \Theta_{A,sat}\dfrac{b_A f^{\nu_A}}{1+b_A f^{\nu_A}}$ $+\Theta_{B,sat}\dfrac{b_B f^{\nu_B}}{1+b_B f^{\nu_B}}$	Site A			Site B		
	$\Theta_{A,sat}$ molecules uc^{-1}	b_A Pa$^{-\nu_A}$	ν_A dimensionless	$\Theta_{B,sat}$ molecules uc^{-1}	b_B Pa$^{-\nu_B}$	ν_B dimensionless
nC5	4	6.26×10^{-6}	1.12	4	1.94×10^{-4}	1
2MB	4	1.69×10^{-4}	1	2	4.93×10^{-7}	1
Neo-pentane	4	1.24×10^{-4}	1			
nC6	3.2	2.21×10^{-8}	1.6	4.3	7.42×10^{-4}	1
2MP	4	7.85×10^{-4}	1.03			
3MP	4	4.22×10^{-4}	1.02	1	9.88×10^{-7}	1
22DMB	4	2.55×10^{-4}	1.02			
23DMB	4	4.59×10^{-4}	1.02			

Table 12. Dual-site Langmuir-Freundlich parameters for pure component pentane isomers at 433 K in Co(BDP). The fits are based on CBMC simulation data of Krishna and van Baten.[3]

$q = q_{A,sat}\dfrac{b_A f^{\nu_A}}{1+b_A f^{\nu_A}}$ $+ q_{B,sat}\dfrac{b_B f^{\nu_B}}{1+b_B f^{\nu_B}}$	Site A			Site B		
	$q_{A,sat}$ mol kg^{-1}	b_A Pa$^{-\nu_A}$	ν_A dimensionless	$q_{B,sat}$ mol kg^{-1}	b_B Pa$^{-\nu_B}$	ν_B dimensionless
nC5	2.17	2.059×10^{-12}	3	3.8	4.365×10^{-5}	1
2MB	1.9	2.52×10^{-10}	2.4	4.3	3.44×10^{-5}	1
Neo-pentane	0.3	3.31×10^{-13}	3	5.3	1.52×10^{-5}	1

Table 13. Dual-Langmuir parameter fits of CBMC simulations of pure component alkane isotherms in Fe$_2$(BDP)$_3$; these parameter values are valid for 433 K. Note that the Freundlich exponents ν_A, and ν_B are unity for all alkanes. The fits are based on the CBMC simulations reported in the Supplementary Material accompanying the paper by Herm et al.[4]

$q_i = q_{A,sat} \dfrac{b_A f}{1+b_A f}$ $+ q_{B,sat} \dfrac{b_B f}{1+b_B f}$	Site A		Site B	
	$q_{A,sat}$	b_A	$q_{B,sat}$	b_B
	mol/kg	Pa^{-1}	mol/kg	Pa^{-1}
nC5	2.0	1.23×10^{-3}	0.7	6.08×10^{-7}
2MB	2.9	1.75×10^{-5}		
neoP	2.8	6.28×10^{-8}		
nC6	1.6	5.9×10^{-3}	0.4	6.26×10^{-5}
2MP	2.1	8.35×10^{-5}		
3MP	2	6.96×10^{-5}		
22DMB	2.75	1.72×10^{-7}		
23DMB	2.75	7.5×10^{-8}		
nC7	1.38	3.93×10^{-2}		
2MH	1.8	5.77×10^{-4}		
3MH	1.85	1.44×10^{-4}		
22DMP	2	4.94×10^{-7}		
23DMP	2	3.24×10^{-7}		

Table 14. Dual-site Langmuir-Freundlich parameters for pure component pentane isomers at 433 K in MgMOF-74. The fits are based on CBMC simulation data of Krishna and van Baten.[3]

$q = q_{A,sat} \dfrac{b_A f^{\nu_A}}{1+b_A f^{\nu_A}}$ $+ q_{B,sat} \dfrac{b_B f^{\nu_B}}{1+b_B f^{\nu_B}}$	Site A			Site B		
	$q_{A,sat}$ mol kg^{-1}	b_A Pa$^{-\nu_A}$	ν_A dimensionless	$q_{B,sat}$ mol kg^{-1}	b_B Pa$^{-\nu_B}$	ν_B dimensionless
nC5	2.2	5.94×10^{-10}	2.6	2.5	1.23×10^{-4}	1
2MB	2.3	2.01×10^{-10}	2.7	2.4	1.1×10^{-4}	1
Neo-pentane	1.1	2.25×10^{-10}	2.4	3.1	3.61×10^{-5}	1

Table 15. Dual-site Langmuir-Freundlich parameters for pure component pentane isomers at 433 K in ZnMOF-74. The fits are based on CBMC simulation data of Krishna and van Baten.[3]

$q = q_{A,sat} \dfrac{b_A f^{\nu_A}}{1+b_A f^{\nu_A}}$ $+ q_{B,sat} \dfrac{b_B f^{\nu_B}}{1+b_B f^{\nu_B}}$	Site A			Site B		
	b_A $\mathrm{Pa}^{-\nu_A}$	ν_A dimensionless	b_A $\mathrm{Pa}^{-\nu_A}$	ν_A dimensionless	b_A $\mathrm{Pa}^{-\nu_A}$	ν_A dimensionless
nC5	1.4	8.54×10^{-10}	2.7	2.1	1.41×10^{-4}	1
2MB	1.6	9.57×10^{-10}	2.6	1.9	1.34×10^{-4}	1
Neo-pentane	0.5	3.71×10^{-9}	2.2	2.7	4.17×10^{-5}	1

Table 16. Dual-site Langmuir-Freundlich parameters for pure component pentane isomers at 433 K in MOF-177. The fits are based on CBMC simulation data of Krishna and van Baten.[3]

$q = q_{A,sat} \dfrac{b_A f^{v_A}}{1 + b_A f^{v_A}}$ $+\, q_{B,sat} \dfrac{b_B f^{v_B}}{1 + b_B f^{v_B}}$	Site A			Site B		
	b_A Pa^{-v_A}	v_A dimensionless	b_A Pa^{-v_A}	v_A dimensionless	b_A Pa^{-v_A}	v_A dimensionless
nC5	8.3	4.03×10^{-17}	3.3	5.8	4.74×10^{-6}	1
2MB	8.5	3.73×10^{-19}	3.7	6	4.39×10^{-6}	1
Neo-pentane	6.7	1.53×10^{-13}	2.4	6.1	2.81×10^{-6}	1

Table 17. Langmuir parameter fits for nC5 and 2MB in ZIF-8. The fits are based on experimental isotherm data of Zhang et al.[30] measured at 308 K, 343 K and 373 K. The experimental data were scanned from Figures 6 and 7 of Zhang et al.[30]

$q = q_{sat} \dfrac{bp}{1+bp}$; $b = b_0 \exp\left(\dfrac{E}{RT}\right)$	q_{sat} mol kg^{-1}	b_0 Pa^{-1}	E kJ mol^{-1}
nC5	3.5	6.5×10^{-11}	45
2MB	2.2	8×10^{-10}	35.4

Table 18. Dual-site Langmuir parameters for pure component butane, pentane, hexane, and heptane isomers at 433 K in ZIF-77. The fits are based on the CBMC simulations of Dubbeldam et al.[2]

$q = q_{A,sat}\dfrac{b_A f}{1+b_A f}$ $+ q_{B,sat}\dfrac{b_B f}{1+b_B f}$	Site A		Site B	
	$q_{A,sat}$ mol/kg	b_A Pa^{-1}	$q_{B,sat}$ mol/kg	b_B Pa^{-1}
nC4	0.91	5.75×10^{-5}	0.81	1.33×10^{-6}
iC4	0.92	1.63×10^{-5}	1.14	3.09×10^{-7}
nC5	0.87	1.82×10^{-4}	0.66	1.87×10^{-6}
2MB	0.8	2.0×10^{-5}	0.6	2.0×10^{-7}
DMP	0.7	6.23×10^{-8}		
nC6	0.81	5.25×10^{-4}	0.59	2.24×10^{-6}
2MP	0.92	4.95×10^{-5}	0.43	1.66×10^{-8}
3MP	0.8	2.15×10^{-5}	0.4	5.15×10^{-8}
22DMB	0.7	2.1×10^{-8}		
23DMB	0.96	6.31×10^{-7}	0.2	3.65×10^{-9}
nC7	0.74	1.72×10^{-3}	0.49	1.69×10^{-6}
2MH	0.8	1.02×10^{-4}	0.27	9.35×10^{-7}
3MH	0.77	5.62×10^{-5}	0.26	1.86×10^{-7}
22DMP	0.71	4.0×10^{-8}	1.1	6.47×10^{-12}
23DMP	0.74	1.38×10^{-6}		

19.   Captions for Figures

Figure 1. Pore landscape and structural data for MFI zeolite.

Figure 2. Pore landscape and structural data for MFI zeolite.

Figure 3. Snapshot of nC5 within the channels of MFI zeolite.

Figure 4. Pore landscape and structural data for BeBTB.

Figure 5. Pore landscape and structural data for BeBTB.

Figure 6. Snapshot of nC5/2MB/neo-P within the pore topology of BeBTB.

Figure 7. Pore landscape and structural data for Co(BDP).

Figure 8. Pore landscape and structural data for Co(BDP).

Figure 9. Snapshot of nC5/2MB/neo-P within the pore topology of Co(BDP).

Figure 10. Pore landscape and structural data for CuBTT.

Figure 11. Pore landscape and structural data for CuBTT.

Figure 12. Snapshot of nC5/2MB/neo-P within the pore topology of CuBTT.

Figure 13. Pore landscape and structural data for Fe$_2$(BDP)$_3$.

Figure 14. Pore landscape and structural data for Fe$_2$(BDP)$_3$.

Figure 15. Snapshot of nC5, 2MB, and neo-P within the triangular channels of Fe$_2$(BDP)$_3$. Also shown are the snapshots of the hexane isomers: n-hexane (nC6), 2-methylpentane (2MP), 3-methylpentane (3MP), 2,2-dimethylbutane (22DMB) and 2,3-dimethylbutane (23DMB).

Figure 16. Pore landscape and structural data for IRMOF-1.

Figure 17. Pore landscape and structural data for IRMOF-1.

Figure 18. Snapshot of nC5/2MB/neo-P within the pore topology of IRMOF-1.

Figure 19. Pore landscape and structural data for MgMOF-74.

Figure 20. Pore landscape and structural data for MgMOF-74.

Figure 21. Snapshot of nC5, 2MB, and neo-P within the hexagonal channels of MgMOF-74.

Figure 22. Snapshot of nC5/2MB/neo-P within the the hexagonal channels of MgMOF-74.

Figure 23. Pore landscape and structural data for ZnMOF-74.

Figure 24. Pore landscape and structural data for ZnMOF-74.

Figure 25. Snapshot of nC5/2MB/neo-P within the the hexagonal channels of ZnMOF-74.

Figure 26. Pore landscape and structural data for MOF-177.

Figure 27. Pore landscape and structural data for MOF-177.

Figure 28. Snapshot of hexane isomers within the pore topology of MOF-177.

Figure 29. Pore landscape and structural data for Zn(bdc)dabco.

Figure 30. Pore landscape and structural data for Zn(bdc)dabco.

Figure 31. Pore landscape and structural data for Zn(bdc)dabco.

Figure 32. Snapshot of nC5/2MB/neo-P within the pore topology of Zn(bdc)dabco.

Figure 33. Pore landscape and structural data for ZIF-77.

Figure 34. Pore landscape and structural data for ZIF-77.

Figure 35. Pore landscape and structural data for ZIF-8.

Figure 36. Pore landscape and structural data for ZIF-8.

Figure 37. CBMC simulation results for adsorption of pentanes in all-silica MFI zeolite at 433 K. (a) unary isotherms for nC5, 2MB, and neo-P. Comparison of CBMC simulations (symbols) with dual-site Langmuir-Freundlich fits. The fit parameters are specified in Table 11. (b) CBMC simulations for equimolar nC5/2MB/neo-P mixture. The continuous solid lines are the IAST estimations using the pure component isotherm fits. (c) nC5/2MB selectivity as a function of the total hydrocarbons fugacity. (d) 2MB/neo-P selectivity as a function of the total hydrocarbons fugacity.

Figure 38. (a) Pure component sorption isotherms for nC6, 3MP and 22DMB in MFI at 433 K. The symbols represent CBMC simulation data.[42-44] The continuous lines are the fits using the dual-site Langmuir-Freundlich model; the parameter values are specified in Table 11. (b, c) CBMC simulations (denoted by symbols), of loadings in MFI zeolite at 433 K for equimolar ternary nC6/3MP/22DMB mixture. The continuous solid lines are calculations using IAST, with parameter values specified in Table 11.

Figure 39. (a) Pure component sorption isotherms for nC6, 2MP, 3MP, 22DMB and 23DMB in MFI at 433 K. The symbols represent CBMC simulation data.[42-44] The continuous lines are the fits using the dual-site Langmuir-Freundlich model; the parameter values are specified in Table 11. (b, c) CBMC simulations (denoted by symbols), of loadings in MFI zeolite at 433 K for equimolar 5-component nC6/2MP/3MP/22DMB/23DMB mixture. The continuous solid lines are calculations using IAST, with parameter values specified in Table 11.

Figure 40. CBMC simulation results for adsorption of pentanes in BeBTB at 433 K. Note that the pure component isotherms were not determined in this case. (b) CBMC simulations for equimolar nC5/2MB/neo-P mixture. (c) nC5/2MB selectivity as a function of the total hydrocarbons fugacity. (d) 2MB/neo-P selectivity as a function of the total hydrocarbons fugacity.

Figure 41. CBMC simulation results for adsorption of pentanes in Co(BDP) at 433 K. (a) unary isotherms for nC5, 2MB, and neo-P. Comparison of CBMC simulations (symbols) with dual-site Langmuir Freundlich fits. The fit parameters are specified in Table 12. (b) CBMC simulations for equimolar nC5/2MB/neo-P mixture. The continuous solid lines are the IAST estimations using the pure component isotherm fits. (c) nC5/2MB selectivity as a function of the total hydrocarbons fugacity. (d) 2MB/neo-P selectivity as a function of the total hydrocarbons fugacity.

Figure 42. CBMC simulation results for adsorption of pentanes in CuBTT at 433 K. Note that the pure component isotherms were not determined in this case. (b) CBMC simulations for equimolar nC5/2MB/neo-P mixture. (c) nC5/2MB selectivity as a function of the total hydrocarbons fugacity. (d) 2MB/neo-P selectivity as a function of the total hydrocarbons fugacity.

Figure 43. CBMC simulation data, culled from Supplementary Material accompanying the paper by Herm et al.,[4] for adsorption of pentanes in $Fe_2(BDP)_3$ at 433 K. (a) unary isotherms for nC5, 2MB, and neo-P. Comparison of CBMC simulations (symbols) with dual-site Langmuir fits. The fit parameters are specified in Table 13. (b) Molecular simulations of heats of adsorption.

Figure 44. (a) CBMC simulation data, culled from Supplementary Material accompanying the paper by Herm et al.,[4] for unary adsorption of hexane isomers: n-hexane (nC6), 2-methylpentane (2MP), 3-methylpentane (3MP), 2,2-dimethylbutane (22DMB) and 2,3-dimethylbutane (23DMB) in $Fe_2(BDP)_3$ at 433 K. (b) Heats of adsorption of pure hexanes. (c) CBMC simulation data, culled from Supplementary Material accompanying the paper by Herm et al.,[4] for unary adsorption of heptane isomers: n-heptane (nC7), 2-methylhexane (2MH), 3-methylhexane (3MH), 2,2-dimethylpentane (22DMP) and 2,3-dimethylpentane (23DMP) in $Fe_2(BDP)_3$ at 433 K. Comparison of CBMC simulations (symbols) with dual-site Langmuir fits. The fit parameters are specified in Table 13.

Figure 45. (a) CBMC simulations for adsorption of equimolar nC5/2MB/neo-P mixture in $Fe_2(BDP)_3$ at 433 K. The continuous solid lines are the IAST estimations using the pure component isotherm fits. (b) nC5/2MB selectivity as a function of the total hydrocarbons fugacity. (c) 2MB/neo-P selectivity as a function of the total hydrocarbons fugacity.

Figure 46. (a) CBMC simulation data (symbols) CBMC simulation data, culled from Supplementary Material accompanying the paper by Herm et al.,[4] for adsorption of 5-component hexanes: nC6/2MP/3MP/22DMB/23DMB in $Fe_2(BDP)_3$ at 433 K. (a) CBMC simulation data (symbols) CBMC simulation data, culled from Supplementary Material accompanying the paper by Herm et al.,[4] for adsorption of 8-component pentanes/hexanes mixture: nC5/2MB/neoP/nC6/2MP/3MP/22DMB/23DMB in $Fe_2(BDP)_3$ at 433 K. For both mixtures the partial fugacities of each component in the mixture is taken to be the same, i.e. $f_1 = f_2 = f_3 = f_4 = f_5 = ...$ The continuous solid lines are the IAST estimations using the pure component isotherm fits specified in Table 13.

Figure 47. CBMC simulation data (symbols) CBMC simulation data, culled from Supplementary Material accompanying the paper by Herm et al.,[4] for adsorption of 13-component pentanes/hexanes/heptanes mixture

nC5/2MB/neoP/nC6/2MP/3MP/22DMB/23DMB/nC7/2MH/3MH/22DMP/23DMP

in $Fe_2(BDP)_3$ at 433 K. The partial fugacities of each component in the mixture is taken to be the same, i.e. $f_1 = f_2 = f_3 = f_4 = f_5 = ... f_{13}$. The continuous solid lines are the IAST estimations using the pure component isotherm fits specified in Table 13.

Figure 48. CBMC simulation results for adsorption of pentanes in IRMOF-1 at 433 K. Note that the pure component isotherms were not determined in this case. (b) CBMC simulations for equimolar nC5/2MB/neo-P mixture. (c) nC5/2MB selectivity as a function of the total hydrocarbons fugacity. (d) 2MB/neo-P selectivity as a function of the total hydrocarbons fugacity.

Figure 49. CBMC simulation results for adsorption of pentanes in MgMOF-74 at 433 K. (a) unary isotherms for nC5, 2MB, and neo-P. Comparison of CBMC simulations (symbols) with dual-site Langmuir Freundlich fits. The fit parameters are specified in Table 14. (b) CBMC simulations for equimolar nC5/2MB/neo-P mixture. The continuous solid lines are the IAST estimations using the pure component isotherm fits. (c) nC5/2MB selectivity as a function of the total hydrocarbons fugacity. (d) 2MB/neo-P selectivity as a function of the total hydrocarbons fugacity.

Figure 50. CBMC simulation results for adsorption of pentanes in ZnMOF-74 at 433 K. (a) unary isotherms for nC5, 2MB, and neo-P. Comparison of CBMC simulations (symbols) with dual-site

Langmuir Freundlich fits. The fit parameters are specified in Table 15. (b) CBMC simulations for equimolar nC5/2MB/neo-P mixture. The continuous solid lines are the IAST estimations using the pure component isotherm fits. (c) nC5/2MB selectivity as a function of the total hydrocarbons fugacity. (d) 2MB/neo-P selectivity as a function of the total hydrocarbons fugacity.

Figure 51. CBMC simulation results for adsorption of pentanes in MOF-177 at 433 K. (a) unary isotherms for nC5, 2MB, and neo-P. Comparison of CBMC simulations (symbols) with dual-site Langmuir-Freundlich fits. The fit parameters are specified in Table 16. (b) CBMC simulations for equimolar nC5/2MB/neo-P mixture. The continuous solid lines are the IAST estimations using the pure component isotherm fits. (c) nC5/2MB selectivity as a function of the total hydrocarbons fugacity. (d) 2MB/neo-P selectivity as a function of the total hydrocarbons fugacity.

Figure 52. CBMC simulation results for adsorption of pentanes in Zn(bdc)dabco at 433 K. Note that the pure component isotherms were not determined in this case. (b) CBMC simulations for equimolar nC5/2MB/neo-P mixture. (c) nC5/2MB selectivity as a function of the total hydrocarbons fugacity. (d) 2MB/neo-P selectivity as a function of the total hydrocarbons fugacity.

Figure 53. CBMC simulation results, culled from Supplementary Material accompanying the paper by Dubbeldam et al.,[2, 4] ENREF_4 for adsorption of pentanes in ZIF-77 at 433 K. (a) unary isotherms for nC5, 2MB, and neo-P. Comparison of CBMC simulations (symbols) with dual-site Langmuir fits. The fit parameters are specified in Table 18. (b) IAST calculations of the component loadings for the

adsorption of equimolar nC5/2MB/neo-P mixture at 433 K. (c) nC5/2MB selectivity as a function of the total hydrocarbons fugacity. (d) 2MB/neo-P selectivity as a function of the total hydrocarbons fugacity.

Figure 54. (a) CBMC simulation data, culled from Supplementary Material accompanying the paper by Dubbeldam et al.[2] for unary adsorption of hexane isomers: n-hexane (nC6), 2-methylpentane (2MP), 3-methylpentane (3MP), 2,2-dimethylbutane (22DMB) and 2,3-dimethylbutane (23DMB) in ZIF-77 at 433 K. The dual-site Langmuir fit parameters are specified in Table 18. (b) CBMC simulation data (symbols), culled from Supplementary Material accompanying the paper by Dubbeldam et al.[2] for adsorption of 5-component hexanes: nC6/2MP/3MP/22DMB/23DMB in ZIF-77 at 433 K. The continuous solid lines are the IAST estimations using the pure component isotherm fits specified in Table 18.

Figure 55. (a) CBMC simulation data, culled from Supplementary Material accompanying the paper by Dubbeldam et al.[2] for unary adsorption of heptane isomers: n-heptane (nC7), 2-methylhexane (2MH), 3-methylhexane (3MH), 2,2-dimethylpentane (22DMP), 2,3-dimethylpentane (23DMP)in ZIF-77 at 433 K. The dual-site Langmuir fit parameters are specified in Table 18. (b) CBMC simulation data (symbols), culled from Supplementary Material accompanying the paper by Dubbeldam et al.[2] for adsorption of 5-component heptanes: nC7/2MH/3MH/22DMP/23DMP in ZIF-77 at 433 K. The continuous solid lines are the IAST estimations using the pure component isotherm fits specified in Table 18.

Figure 56. Adsorption of nC5 and 2MB in ZIF-8. The experimental unary isotherms were determined by Zhang et al.[30] at 308 K, 343 K and 373 K. The data were fitted with T-dependent single-site

Langmuir model; the parameters are specified in Table 17. (a) The isotherm fits were used to calculate the unary isotherms of nC5 and 2MB at 433 K. (b) IAST calculations of the component loadings for equimolar nC5/2MB mixtures at 433 K. (c) nC5/2MB selectivity as a function of the total hydrocarbons pressure.

Figure 57. Comparison of the (a) nC5/2MB, and (b) 2MB/neo-P selectivities for adsorption of nC5/2MB/neo-P mixtures, plotted as a function of the total hydrocarbons fugacity in the bulk fluid phase, $f_t=f_1+f_2+f_3$.

Figure 58. Comparison of the uptake capacities of (a) nC5, and (b) 2MB for adsorption of nC5/2MB/neo-P mixtures, plotted as a function of the total hydrocarbons fugacity in the bulk fluid phase, $f_t=f_1+f_2+f_3$.

Figure 59. Schematic of a packed bed adsorber.

Figure 60. Transient nC5(1)/2MB(2) breakthrough simulations for fixed bed adsorbers packed with ZIF-77, MFI, Fe$_2$(BDP)$_3$, and ZIF-8, and operating at 433 K. The partial fugacities in the feed gas mixture at the inlet, $f_1=f_2=50$ kPa. (a) The dimensionless concentration of nC5 and 2MB, normalized with respect to the molar concentrations at the adsorber inlet, are plotted against the dimensionless time, $\tau=\dfrac{tu}{L\varepsilon}$. (b) The difference in the dimensionless breakthrough times between nC5 and 2MB, $\Delta\tau$, is plotted against the dimensionless breakthrough time of nC5.

Figure 61. Transient nC5(1)/2MB(2) breakthrough simulations for fixed bed adsorber packed with ZIF-8 and operating at 433 K. The partial fugacities in the feed gas mixture at the inlet, $f_1 = f_2 = 50$ kPa. The dimensionless concentration of nC5 and 2MB, normalized with respect to the molar concentrations at the adsorber inlet, are plotted against the dimensionless time, $\tau = \dfrac{tu}{L\varepsilon}$. The diffusivity values used in the simulations are $Đ_{nC5}/r_c^2 = 2.5 \times 10^{-5}$ s^{-1}; $Đ_{2NB}/r_c^2 = 5 \times 10^{-5}$ s^{-1}; $Đ_{nC5}/Đ_{2MB} = 50$.

Figure 62. Transient 2MB(1)/neo-P(2) breakthrough simulations for fixed bed adsorbers packed with ZIF-77, MFI, and Fe$_2$(BDP)$_3$, and operating at 433 K. The partial fugacities in the feed gas mixture at the inlet, $f_1 = f_2 = 50$ kPa. (a) The dimensionless concentration of 2MB and neo-P, normalized with respect to the molar concentrations at the adsorber inlet, are plotted against the dimensionless time, $\tau = \dfrac{tu}{L\varepsilon}$. (b) The difference in the dimensionless breakthrough times between 2MB and neo-P, $\Delta\tau$, is plotted against the dimensionless breakthrough time of 2MB.

Figure 63. Conventional process flow scheme for isomerization of C5/C6/C7 alkanes.

Figure 64. Suggested improved process for C5/C6/C7 isomerization.

Figure 65. (a, b, c) Transient breakthrough of nC5(1)/2MB(2)/neo-P(3) mixture, with step-input, in fixed bed adsorbers packed with (a) $Fe_2(BDP)_3$, (b) ZIF-77, (c) MFI zeolite operating at 433 K. The partial fugacities in the feed gas mixture at the inlet, $f_1 = f_2 = f_3 = 30$ kPa. The dimensionless concentration of nC5, 2MB and neo-P, normalized with respect to the molar concentrations at the adsorber inlet, are plotted against the dimensionless time. (d) Plot of the RON of the product gas mixture at the adsorber outlet as a function of the dimensionless time.

Figure 66. (a) Transient breakthrough of nC6/2MP/3MP/22DMB/23DMB mixture, with step-input, in fixed bed adsorbers packed with $Fe_2(BDP)_3$. (b) Plot of the RON of the product gas mixture at the adsorber outlet as a function of the dimensionless time.

Figure 67. (a) Transient breakthrough 8-component pentanes/hexanes mixture: nC5/2MB/neoP/nC6/2MP/3MP/22DMB/23DMB, with step-input, in fixed bed adsorbers packed with $Fe_2(BDP)_3$. (b) Plot of the RON of the product gas mixture at the adsorber outlet as a function of the dimensionless time.

Figure 68. (a) Transient breakthrough 13-component pentanes/hexanes/heptanes mixture

nC5/2MB/neoP/nC6/2MP/3MP/22DMB/23DMB/nC7/2MH/3MH/22DMP/23DMP

with step-input, in fixed bed adsorbers packed with $Fe_2(BDP)_3$. (b) Plot of the RON of the product gas mixture at the adsorber outlet as a function of the dimensionless time.

Figure 69. Pulse chromatographic simulations for separation of nC5(1)/2MB(2)/neo-P(3) mixture in fixed bed adsorbers packed with $Fe_2(BDP)_3$ and operating at 433 K. The partial fugacities in the feed gas mixture at the inlet, $f_1 = f_2 = f_3 = 30$ kPa. The dimensionless concentration of nC5, 2MB and neo-P, normalized with respect to the molar concentrations at the adsorber inlet, are plotted against the dimensionless time. The duration of the pulse is 10 s.

Figure 70. (a) Pulse chromatographic simulations for separation of (a) 5-component hexane isomer mixture: nC6/2MP/3MP/22DMB/23DMB, and (b) 5-component heptanes: nC7/2MH/3MH/22DMP/23DMP in fixed bed adsorber packed with $Fe_2(BDP)_3$ and operating at 433 K. The partial fugacities in the feed gas mixture at the inlet, $f_1 = f_2 = f_3 = f_4 = f_5 = 20$ kPa. These simulations are carried out using pure component isotherm fits of CBMC simulations using the dual-site Langmuir parameters in Table 13.

Figure 71. Pulse chromatographic simulation of 8-component pentanes/hexanes mixture: nC5/2MB/neoP/nC6/2MP/3MP/22DMB/23DMB in fixed bed adsorber packed with $Fe_2(BDP)_3$ and operating at 433 K. These simulations are carried out using pure component isotherm fits of CBMC simulations using the dual-site Langmuir parameters in Table 13.

Figure 72. Pulse chromatographic simulation of 13-component pentanes/hexanes/heptanes mixture

nC5/2MB/neoP/nC6/2MP/3MP/22DMB/23DMB/nC7/2MH/3MH/22DMP/23DMP

in fixed bed adsorber packed with $Fe_2(BDP)_3$ and operating at 433 K. These simulations are carried out using pure component isotherm fits of CBMC simulations using the dual-site Langmuir parameters in Table 13.

MFI pore landscape

	MFI
a /Å	20.022
b /Å	19.899
c /Å	13.383
Cell volume / Å^3	5332.025
conversion factor for [molec/uc] to [mol per kg Framework]	0.1734
conversion factor for [molec/uc] to [kmol/m^3]	1.0477
ρ [kg/m3]	1796.386
MW unit cell [g/mol(framework)]	5768.141
ϕ, fractional pore volume	0.297
open space / Å^3/uc	1584.9
Pore volume / cm^3/g	0.165
Surface area /m^2/g	487.0
DeLaunay diameter /Å	5.16
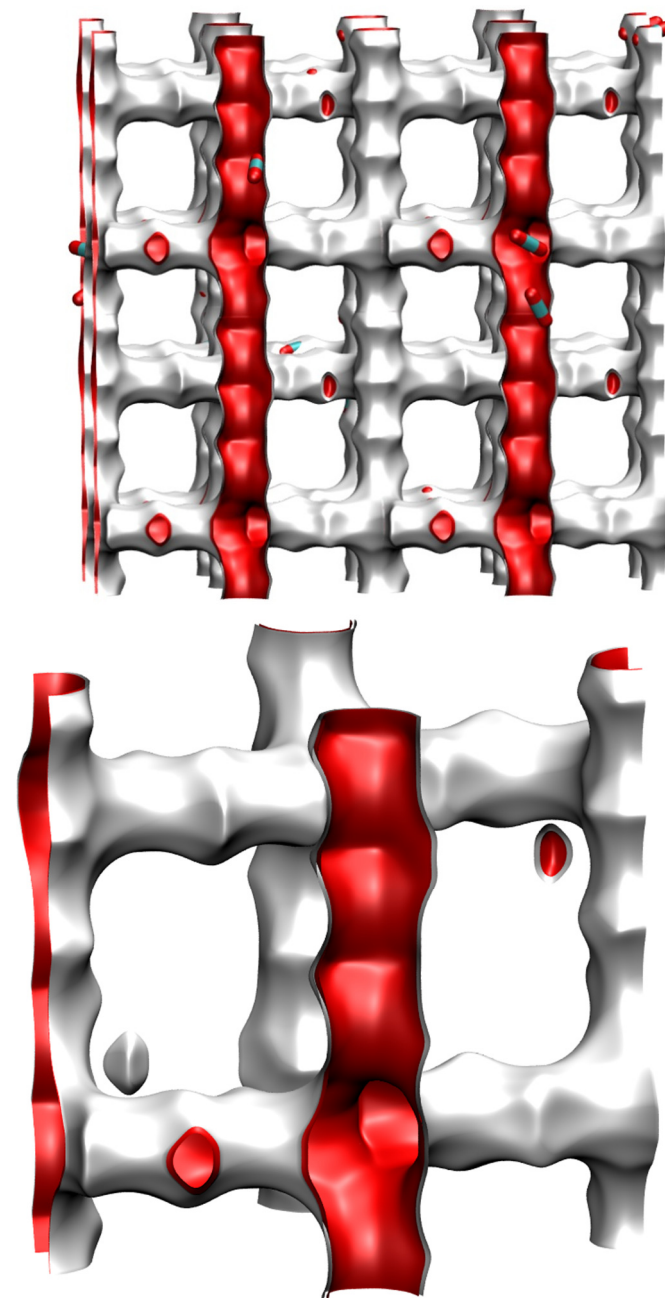
MFI pore dimensions

10 ring channel of MFI viewed along [100]
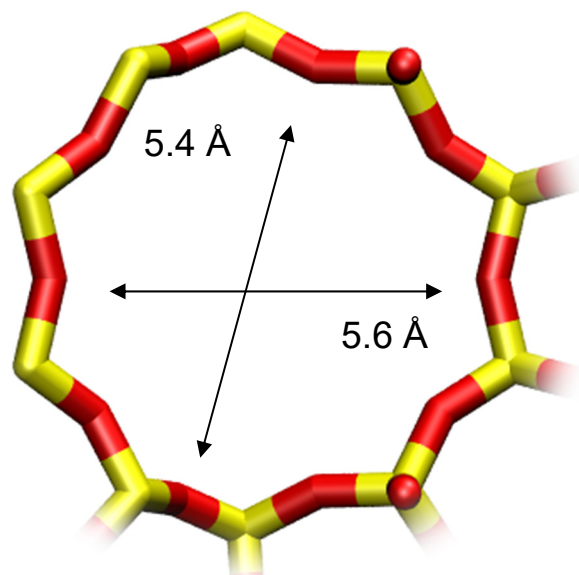
10 ring channel of MFI viewed along [010]
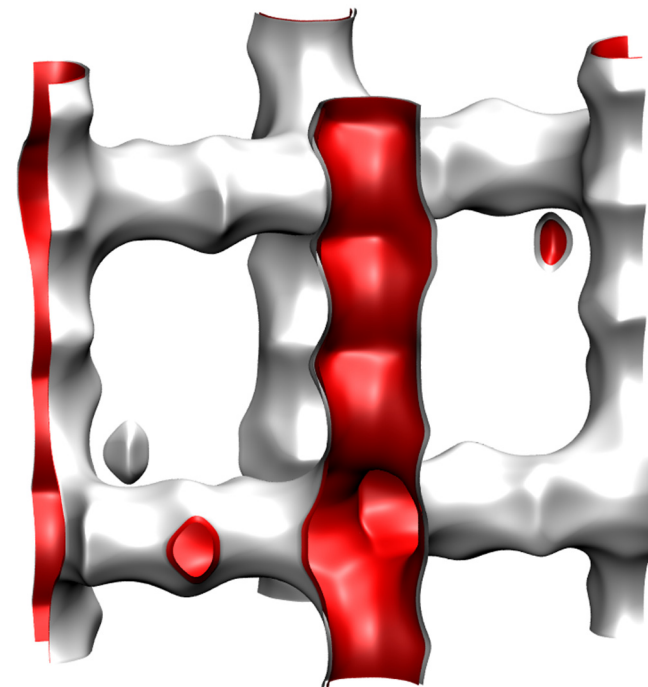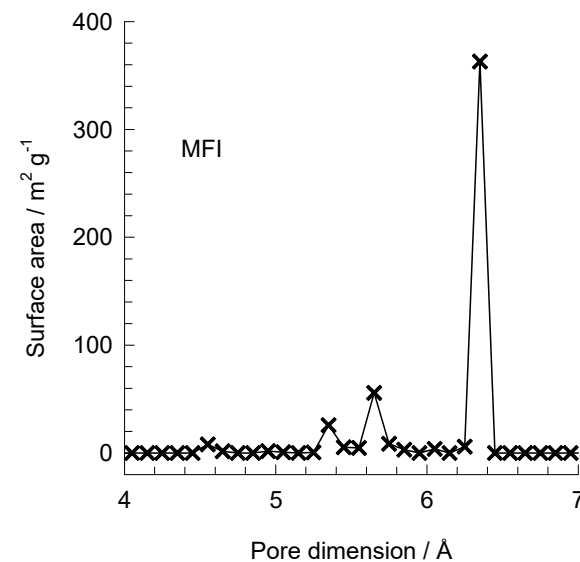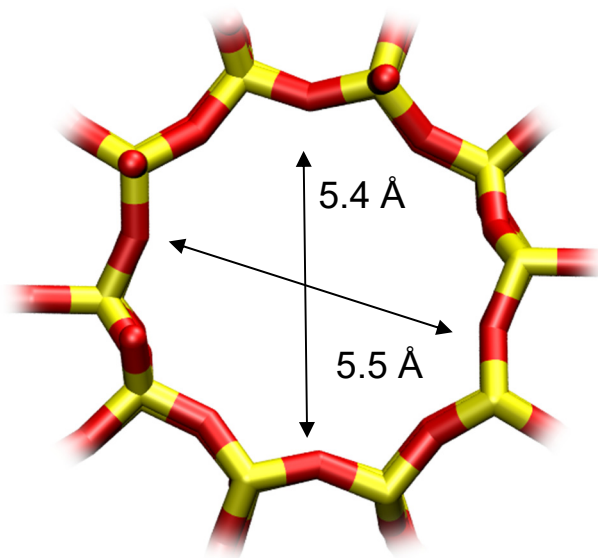
MFI snapshot of unary nC5

The linear molecule nC5 can locate along the straight and zig-zag channels.
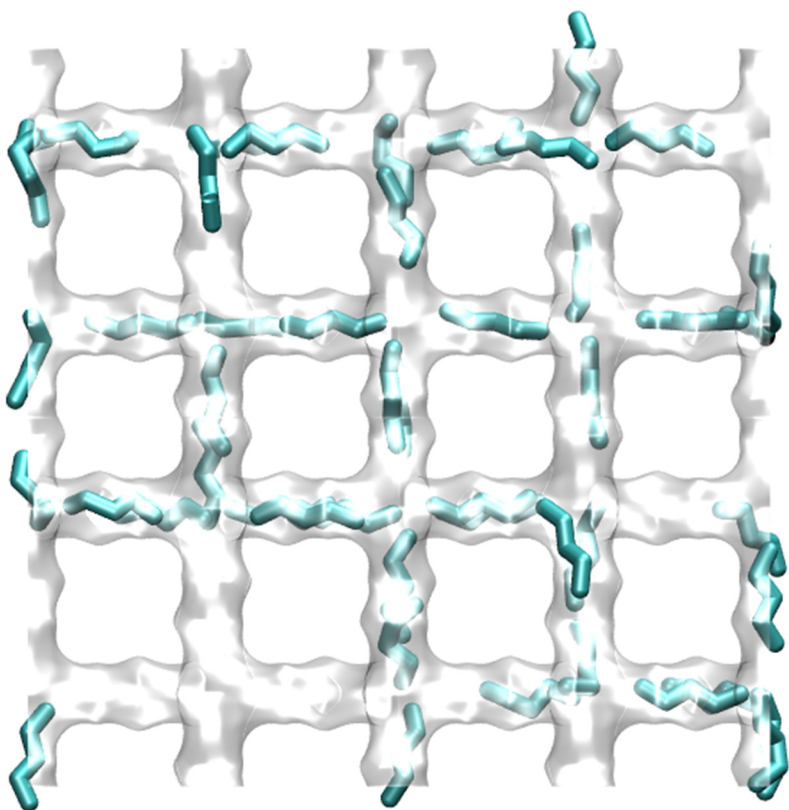
The branched isomers prefer location at the channel intersections

BeBTB pore landscapes
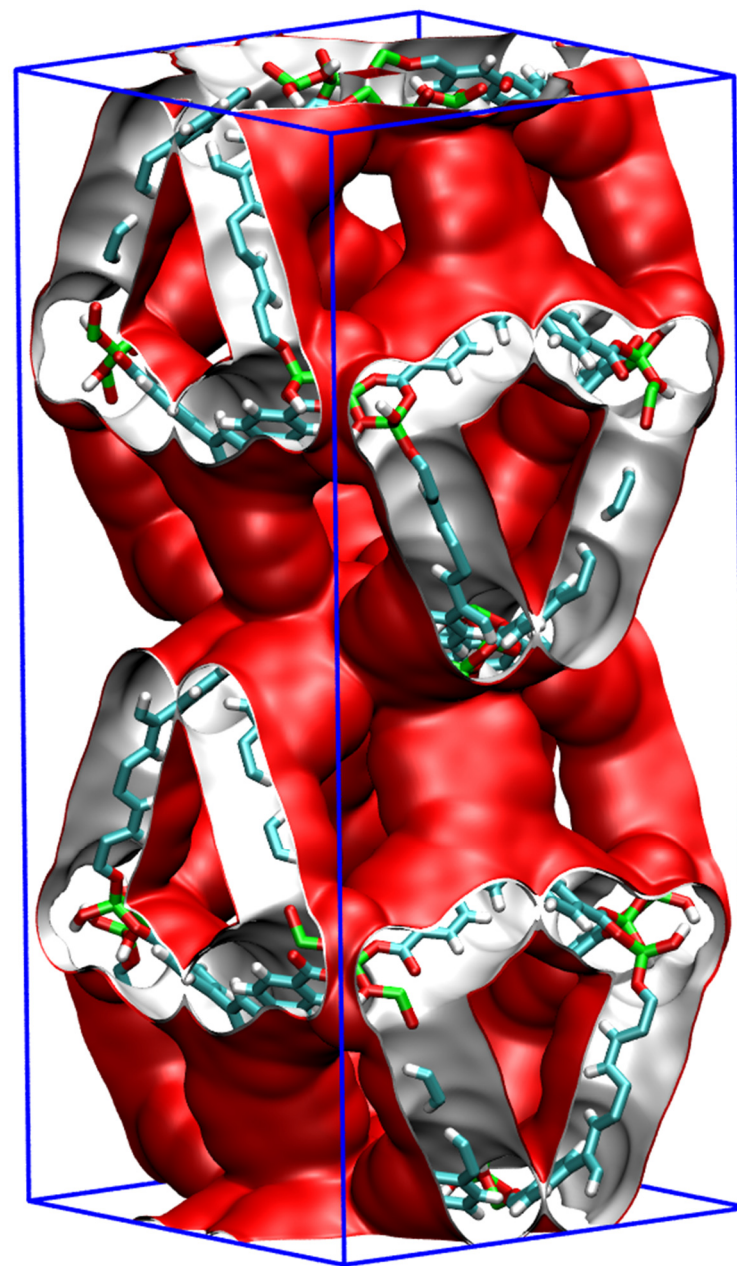
BeBTB pore dimensions
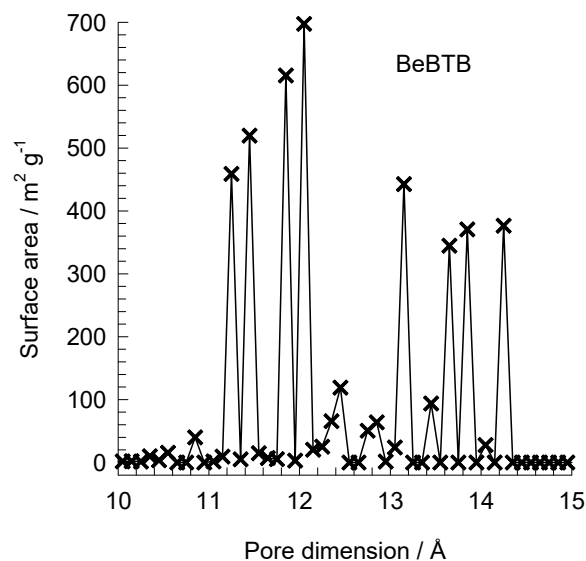
This plot of surface area versus pore dimension is determined using a combination of the DeLaunay triangulation method for pore dimension determination, and the procedure of Düren for determination of the surface area.

	BeBTB
a /Å	24.3013
b /Å	24.3013
c /Å	54.57
Cell volume / Å^3	32226.49
conversion factor for [molec/uc] to [mol per kg Framework]	0.1218
conversion factor for [molec/uc] to [kmol/m^3]	0.0638
ρ [kg/m3]	423.0851
MW unit cell [g/mol(framework)]	8210.785
ϕ, fractional pore volume	0.807
open space / Å^3/uc	26013.8
Pore volume / cm^3/g	1.908
Surface area /m^2/g	4706.0

BeBTB snapshot of nC5/2MB/neo-P isomers

Figure S6
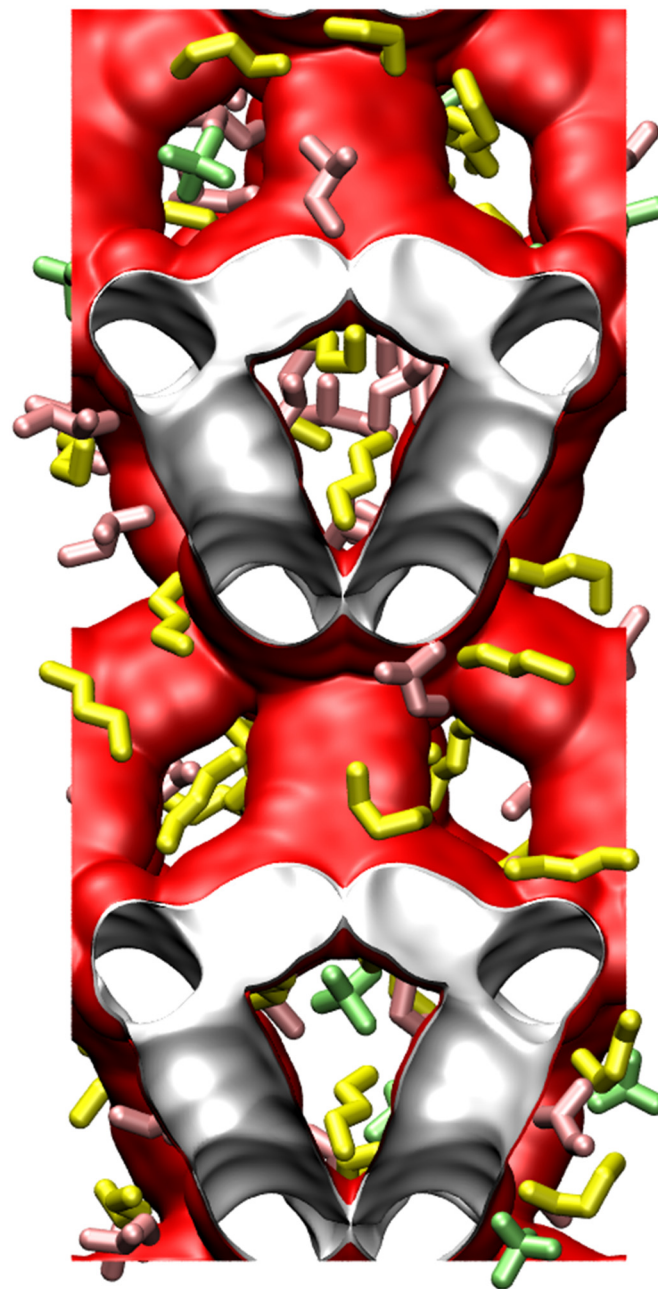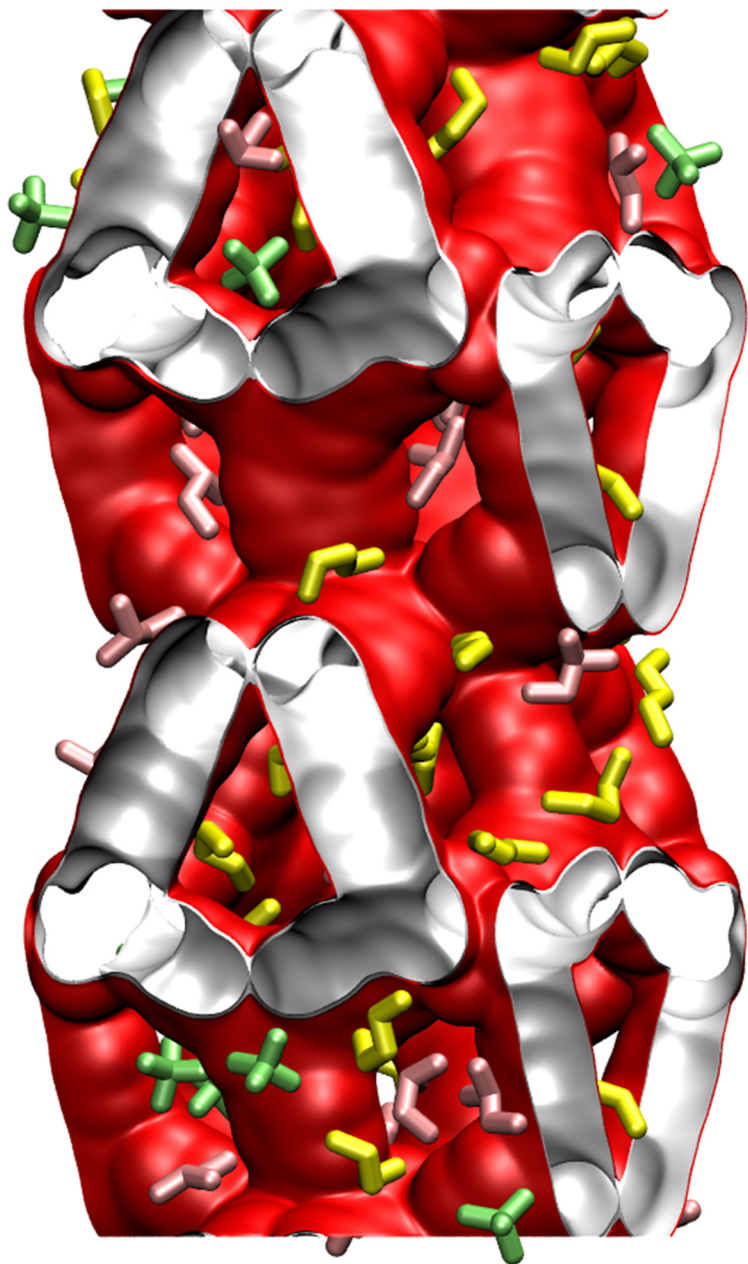
Co(BDP) pore landscapes
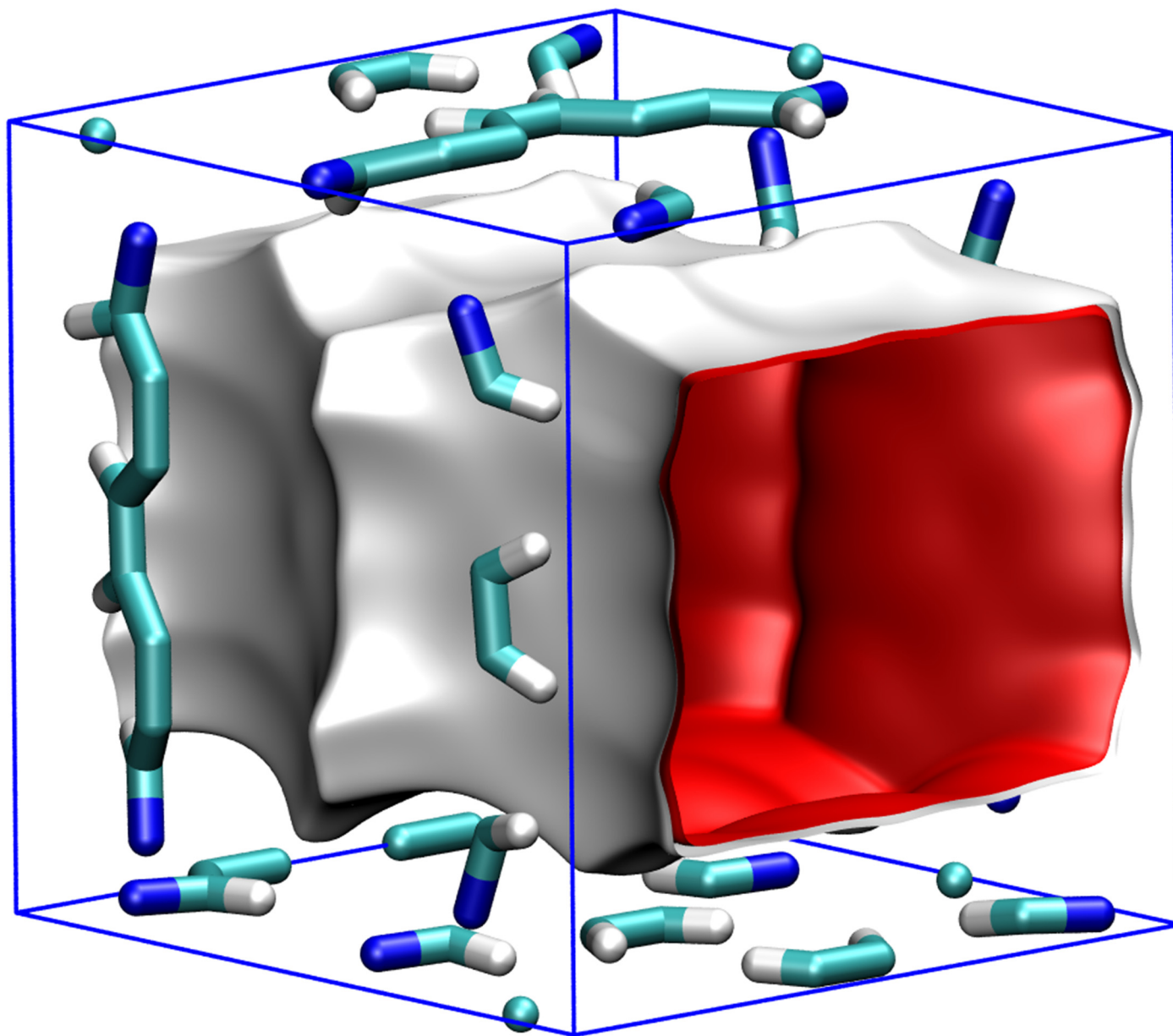
Co(BDP) pore dimensions
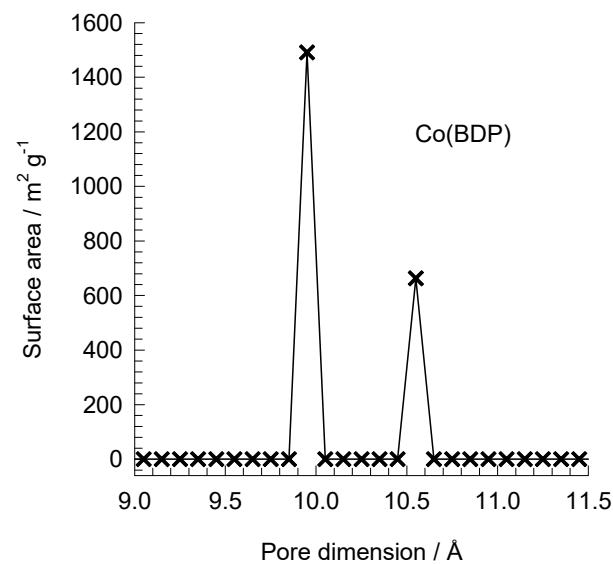
This plot of surface area versus pore dimension is determined using a combination of the DeLaunay triangulation method for pore dimension determination, and the procedure of Düren for determination of the surface area.

	CoBDP
a /Å	13.2529
b /Å	13.253
c /Å	13.995
Cell volume / Å^3	2458.091
conversion factor for [molec/uc] to [mol per kg Framework]	0.9362
conversion factor for [molec/uc] to [kmol/m^3]	1.0102
ρ [kg/m3]	721.5517
MW unit cell [g/mol(framework)]	1068.094
ϕ, fractional pore volume	0.669
open space / Å^3/uc	1643.9
Pore volume / cm^3/g	0.927
Surface area /m^2/g	2148.8
DeLaunay diameter /Å	10

Co(BDP) snapshots

Snapshot of pure pentanes

CuBTT pore landscapes

These inaccessible pockets were blocked in our simulations
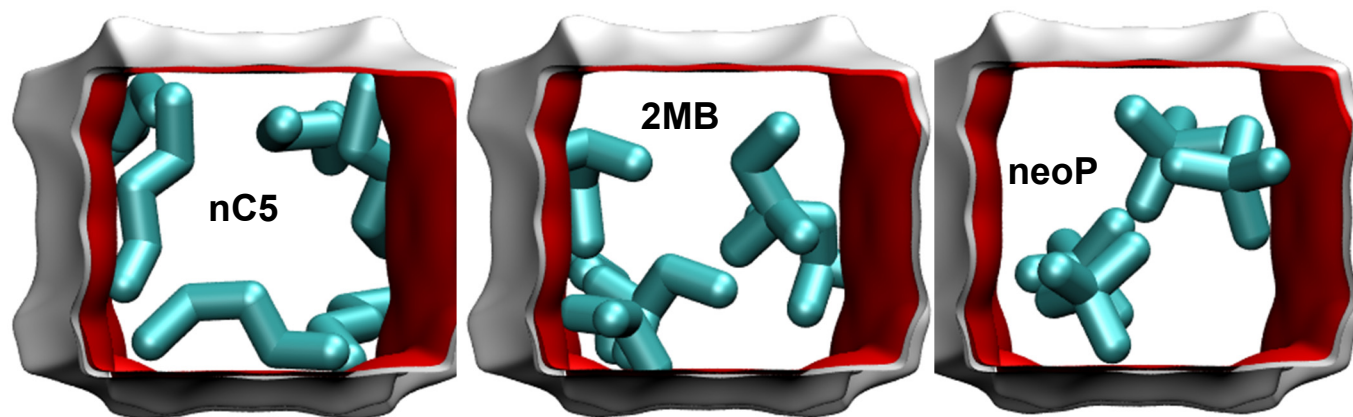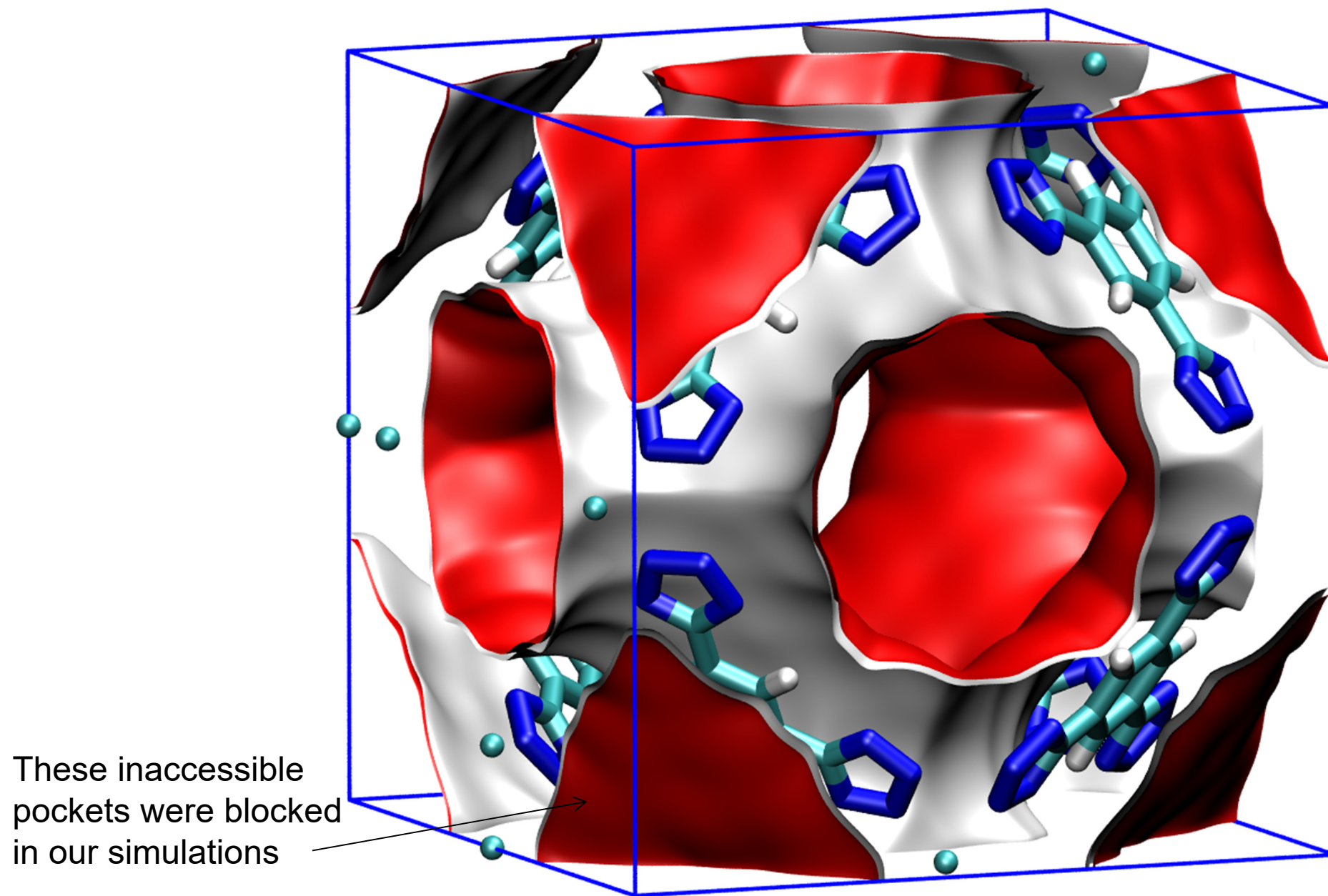
CuBTT pore dimensions

This plot of surface area versus pore dimension is determined using a combination of the DeLaunay triangulation method for pore dimension determination, and the procedure of Düren for determination of the surface area.

	CuBTT (blocked)
a /Å	18.595
b /Å	18.595
c /Å	18.595
Cell volume / Å^3	6429.668
conversion factor for [molec/uc] to [mol per kg Framework]	0.3224
conversion factor for [molec/uc] to [kmol/m^3]	0.4547
ρ [kg/m3]	801.0756
MW unit cell [g/mol(framework)]	3101.745
ϕ, fractional pore volume	0.568
open space / Å^3/uc	3652.1
Pore volume / cm^3/g	0.709
Surface area /m^2/g	1564.6
DeLaunay diameter /Å	9.99

CuBTT snshot of nC5/2MB/neo-P isomers

Figure S12
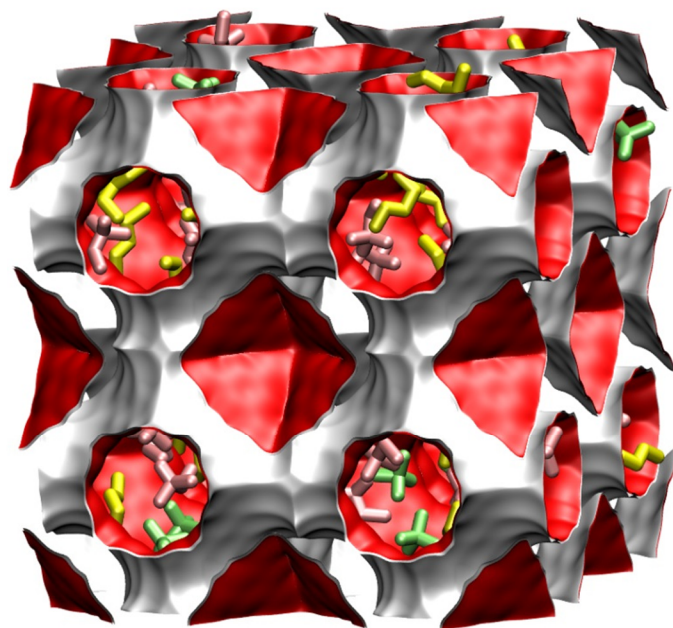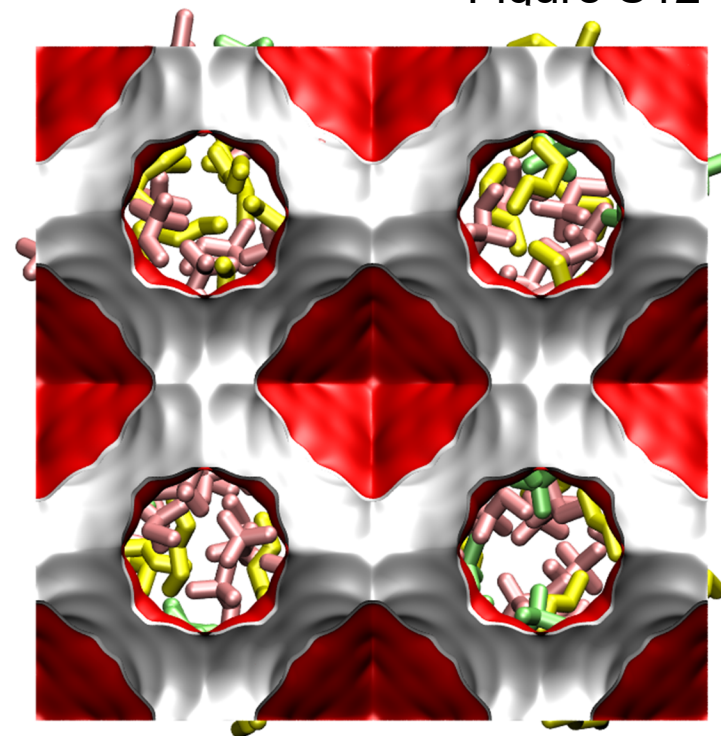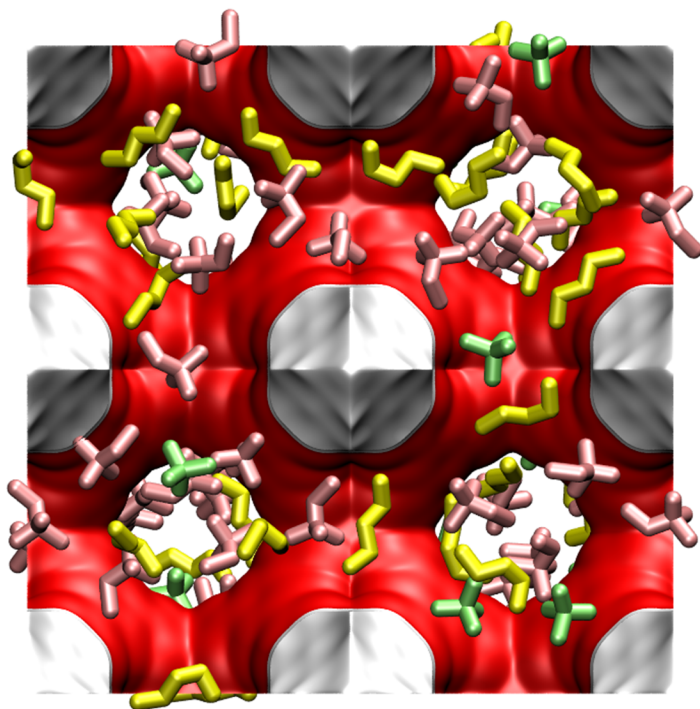
Fe$_2$(BDP)$_3$ pore landscapes
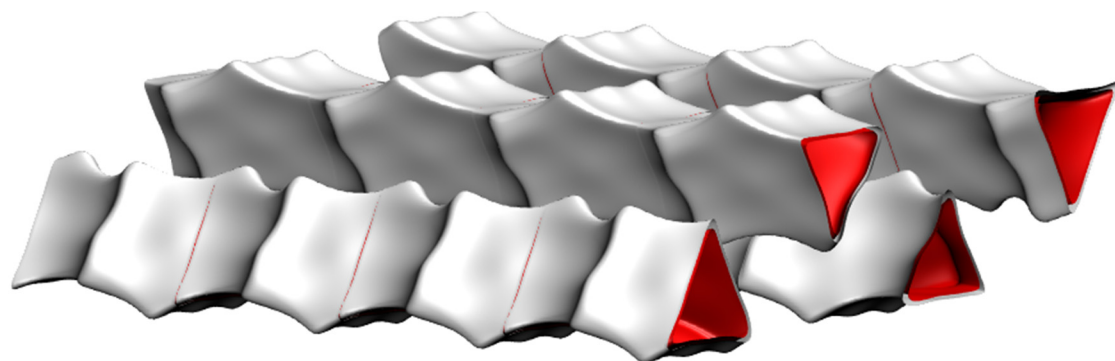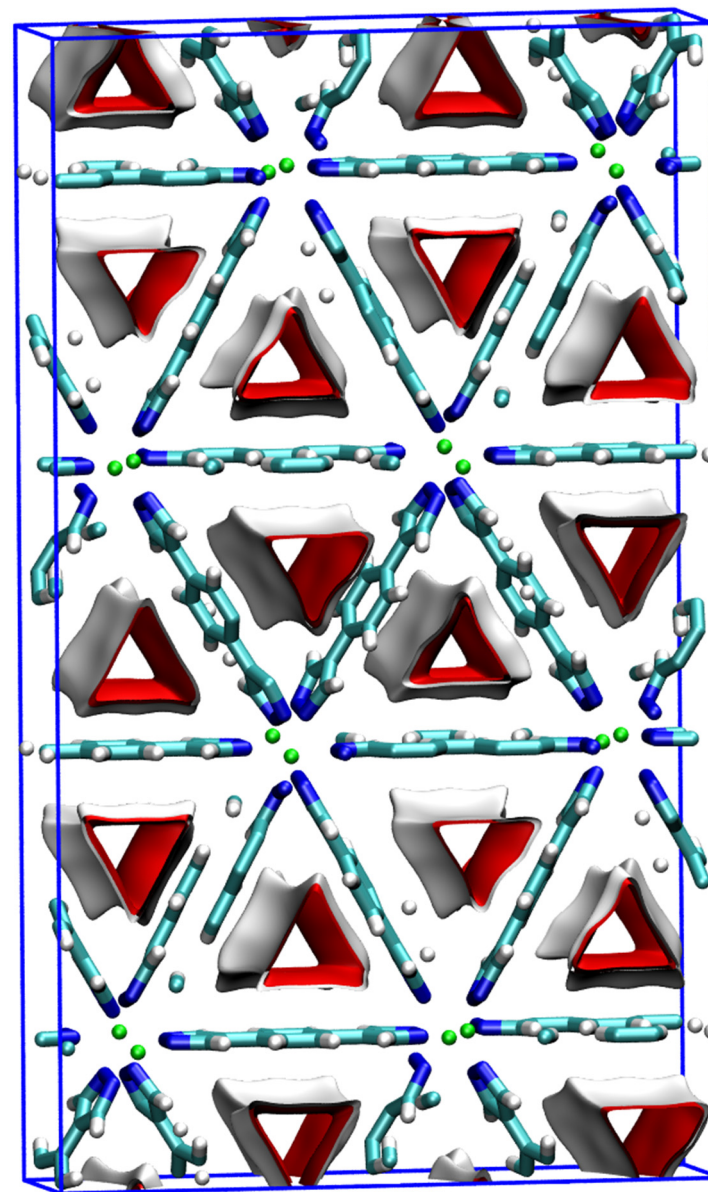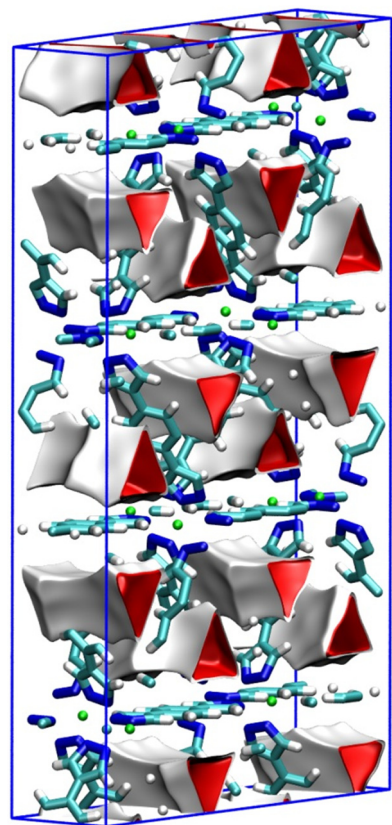
Fe$_2$(BDP)$_3$ pore dimensions

	Fe$_2$(BDP)$_3$
a /Å	7.104
b /Å	26.491
c /Å	45.353
Cell volume / Å^3	8535.33
ρ [kg/m3]	1145.46
Pore volume / cm^3/g	0.4
DeLaunay diameter /Å	4.9

Fe$_2$(BDP)$_3$ snapshots of C5, C6 isomers

Fe$_2$(BDP)$_3$

4.9 Å triangular channels
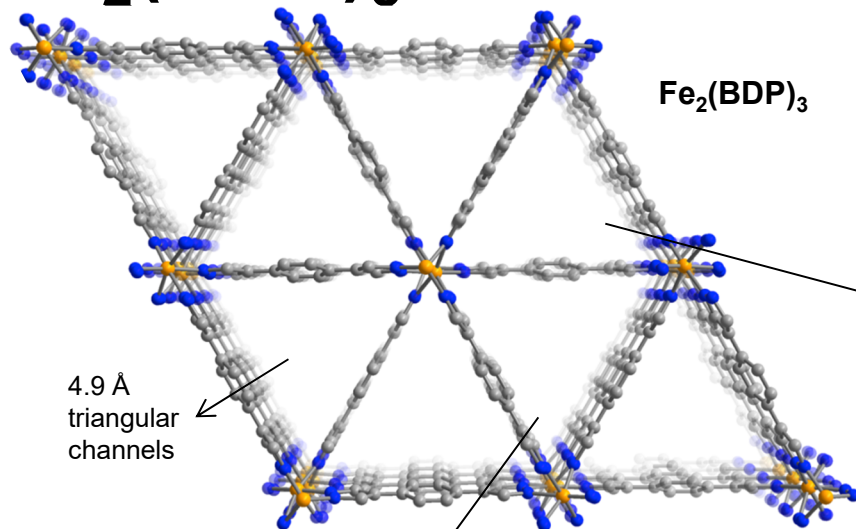
Side-view of C6 isomers in the gutters
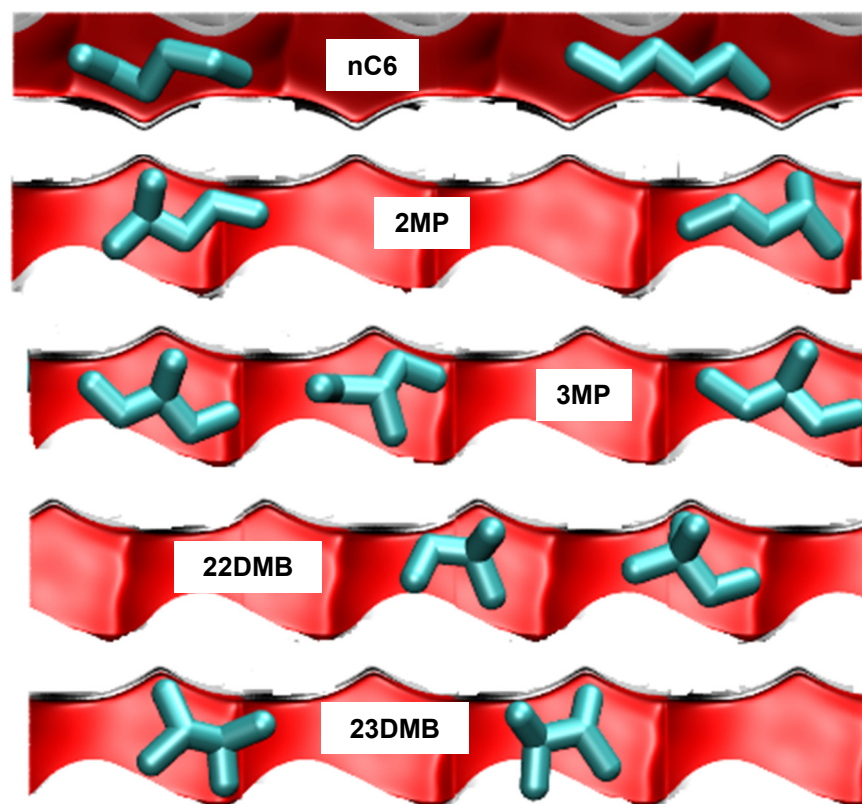
Side-view of C5 isomers in the gutters

nC6

2MP

3MP

22DMB

23DMB

nC5

2MB

neo-P
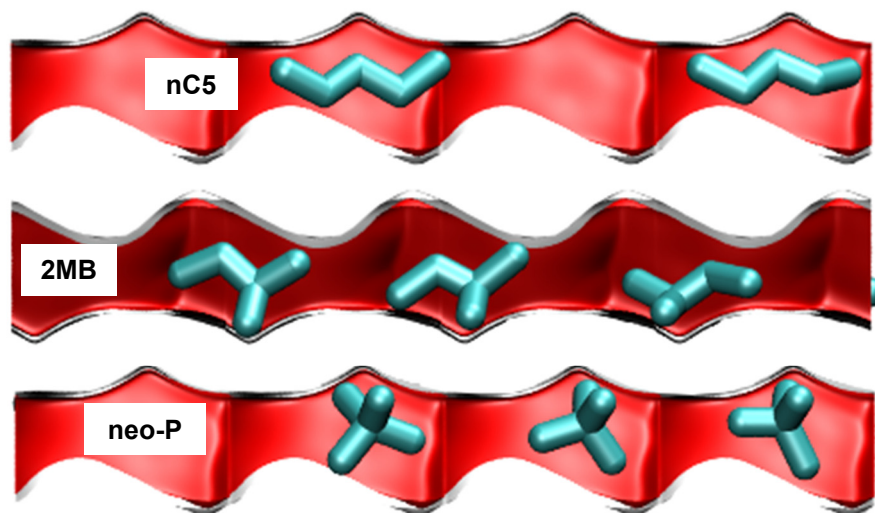
IRMOF-1 pore landscape

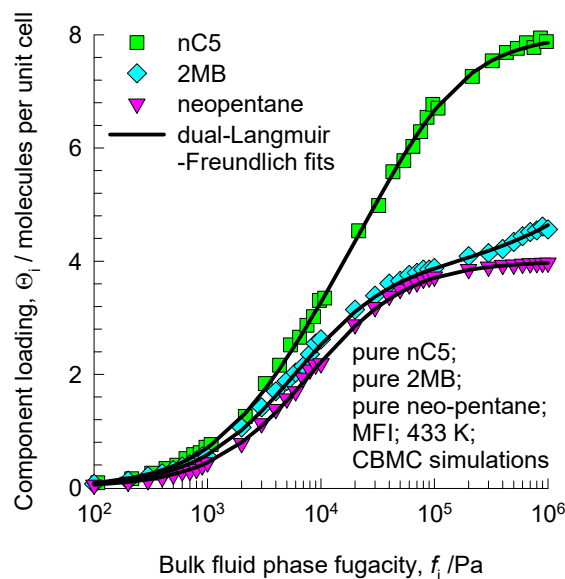Figure S16
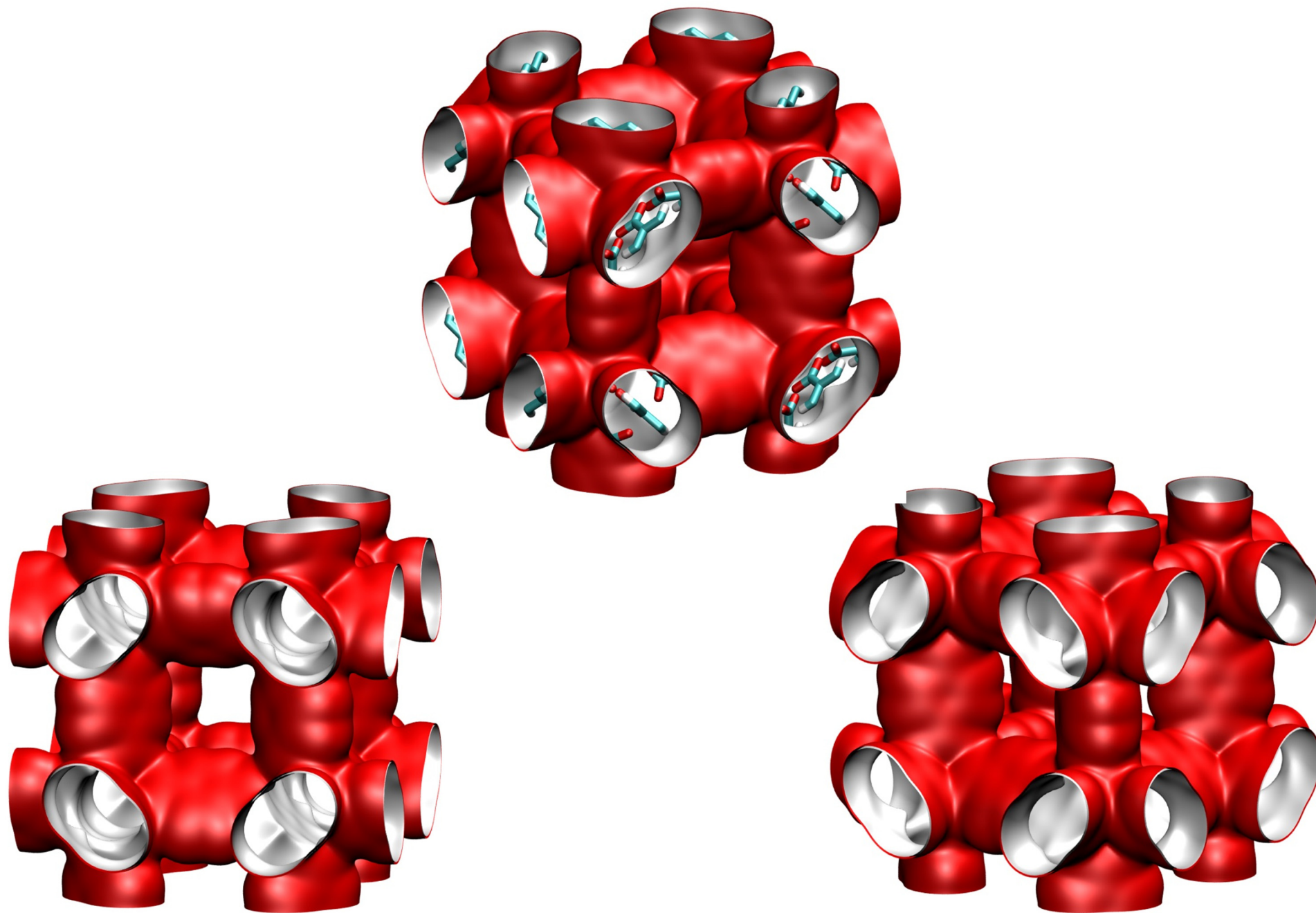
IRMOF-1 pore dimensions
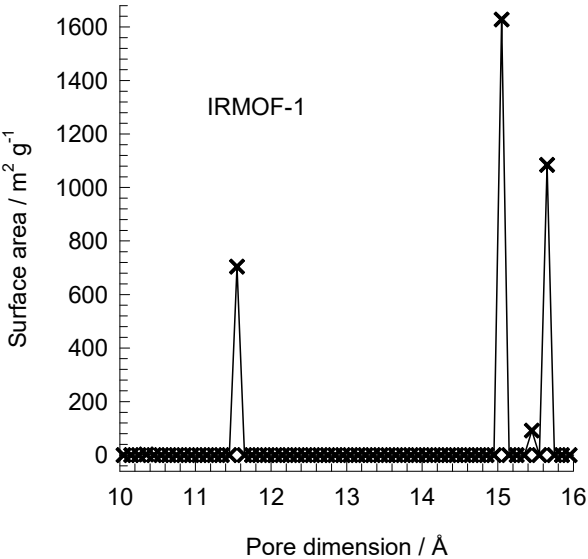
This plot of surface area versus pore dimension is determined using a combination of the DeLaunay triangulation method for pore dimension determination, and the procedure of Düren for determination of the surface area.

	IRMOF-1
a /Å	25.832
b /Å	25.832
c /Å	25.832
Cell volume / Å^3	17237.49
conversion factor for [molec/uc] to [mol per kg Framework]	0.1624
conversion factor for [molec/uc] to [kmol/m^3]	0.1186
ρ [kg/m3]	593.2075
MW unit cell [g/mol(framework)]	6157.788
ϕ, fractional pore volume	0.812
open space / Å^3/uc	13996.3
Pore volume / cm^3/g	1.369
Surface area /m^2/g	3522.2
DeLaunay diameter /Å	7.38

IRMOF-1 snapshot of nC5/2MB/neo-P mix

Figure S18
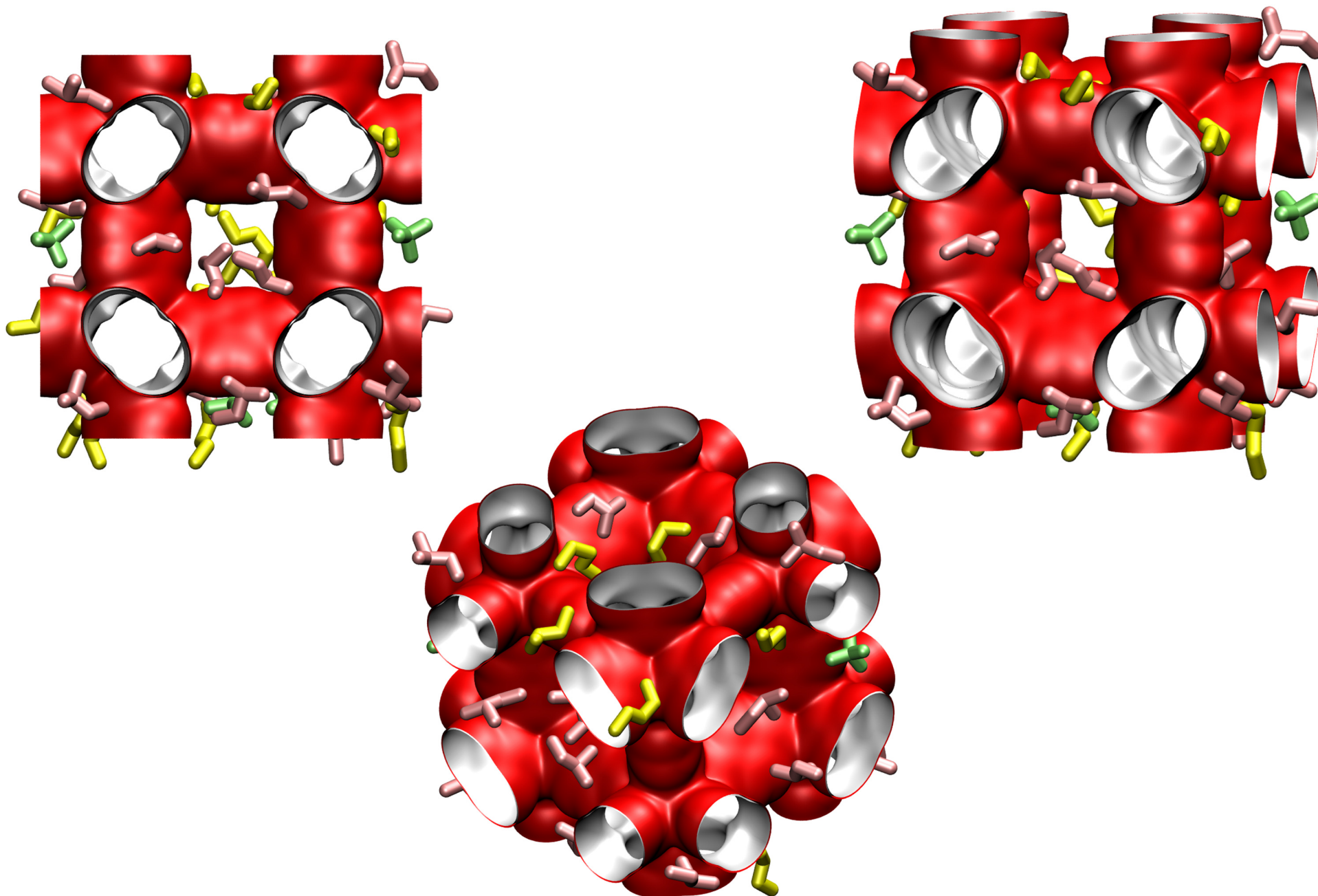
MgMOF-74 pore landscapes
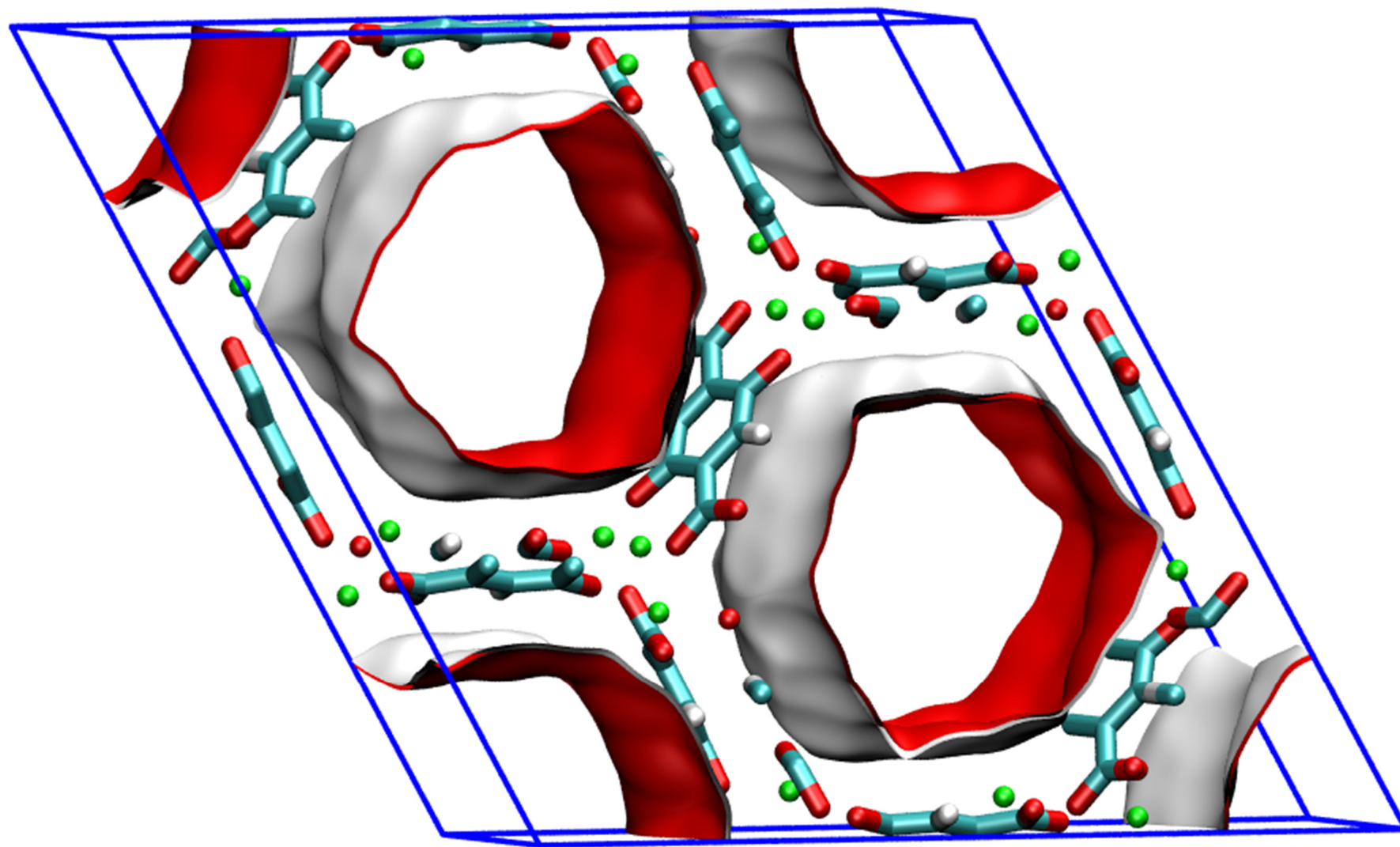
MgMOF-74 pore dimensions
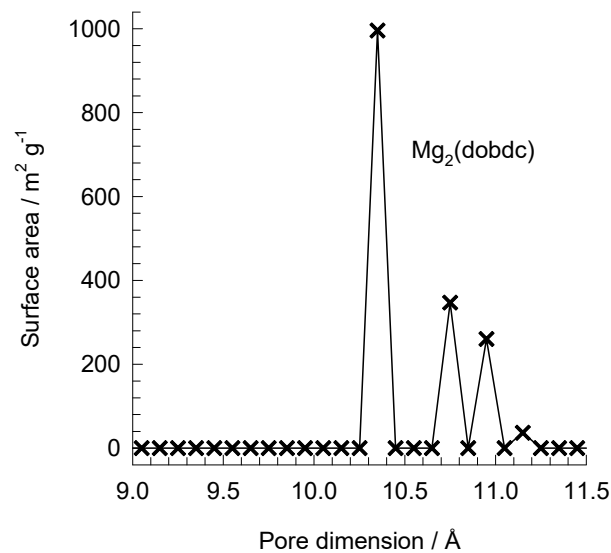
This plot of surface area versus pore dimension is determined using a combination of the DeLaunay triangulation method for pore dimension determination, and the procedure of Düren for determination of the surface area.

	MgMOF-74
a /Å	25.8621
b /Å	25.8621
c /Å	6.91427
Cell volume / Å^3	4005.019
conversion factor for [molec/uc] to [mol per kg Framework]	0.4580
conversion factor for [molec/uc] to [kmol/m^3]	0.5856
ρ [kg/m3]	905.367
MW unit cell [g/mol(framework)]	2183.601
ϕ, fractional pore volume	0.708
open space / Å^3/uc	2835.6
Pore volume / cm^3/g	0.782
Surface area /m^2/g	1640.0
DeLaunay diameter /Å	10.66

MgMOF-74 unary pentanes snaps

nC5
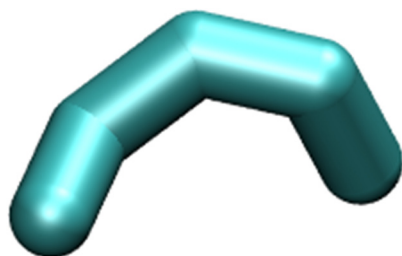
2MB
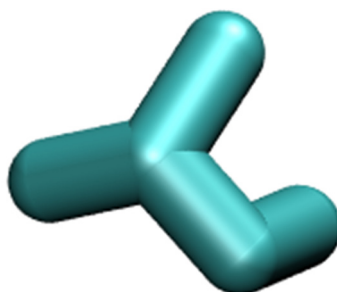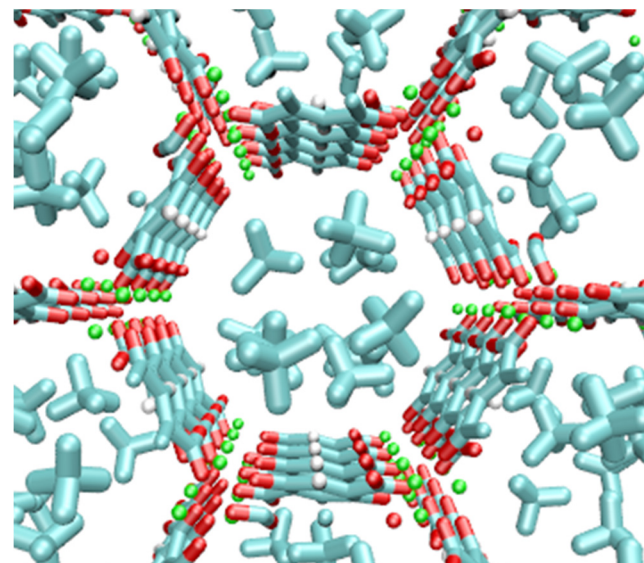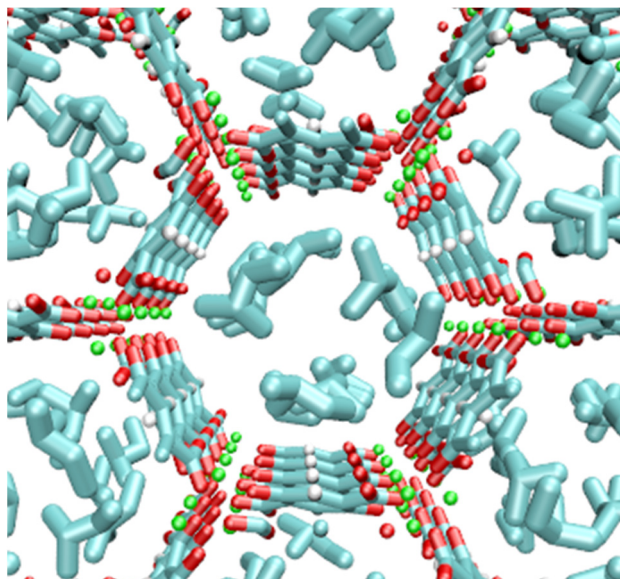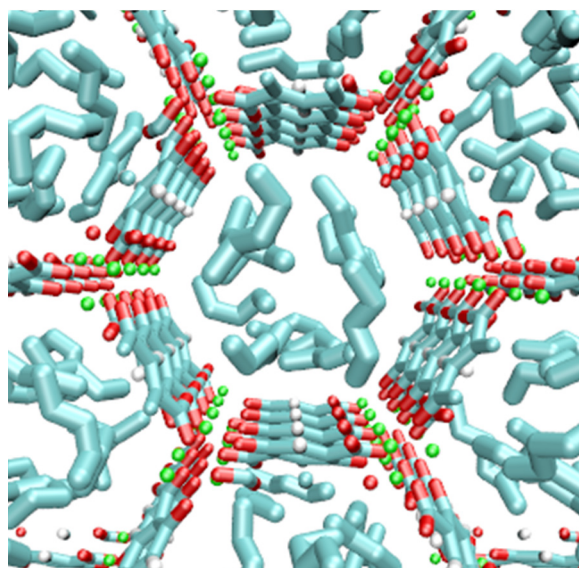
neoP

MgMOF-74 nC5/2MB/neo-P snap
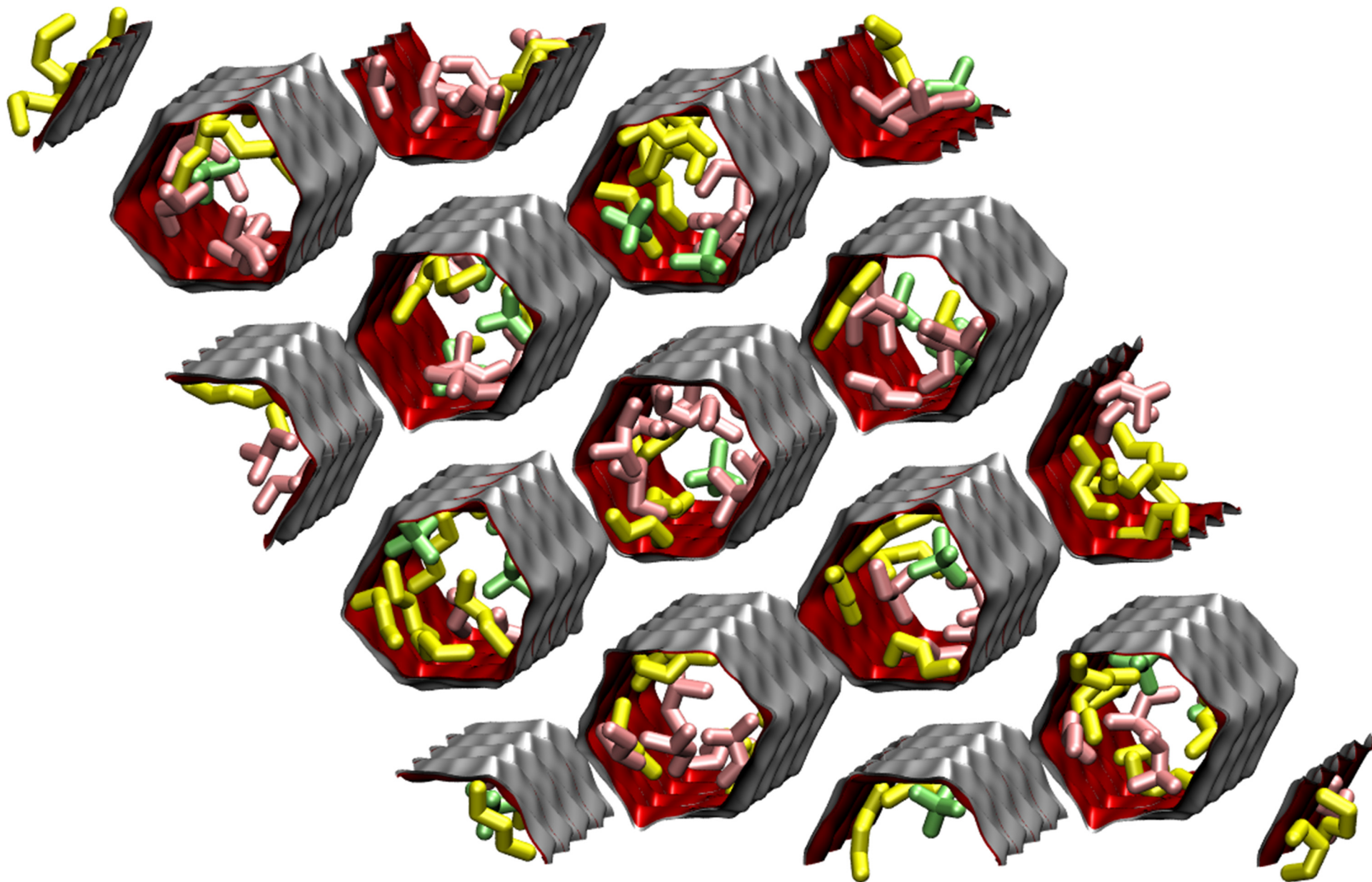
ZnMOF-74 pore landscapes
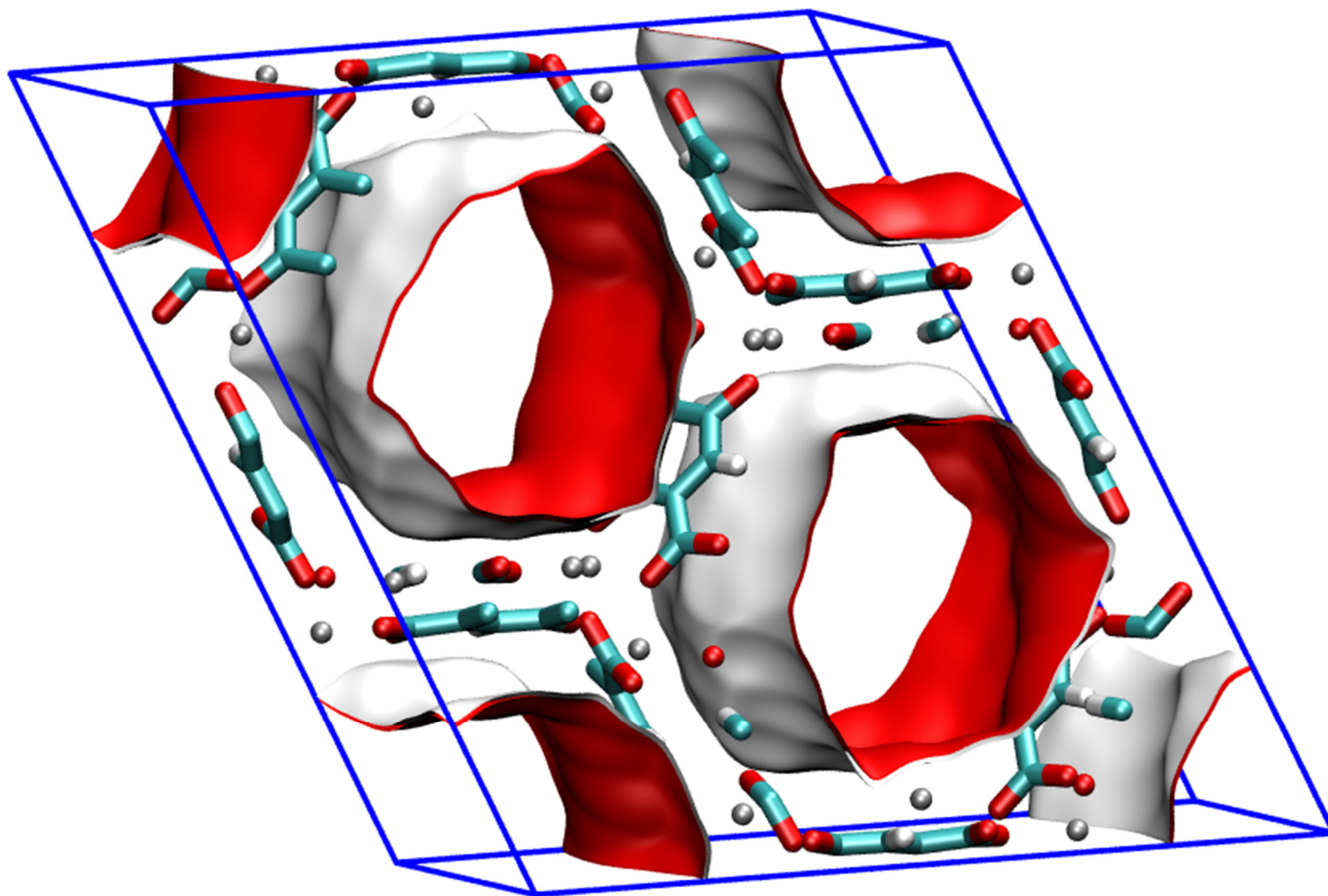
ZnMOF-74 pore dimensions
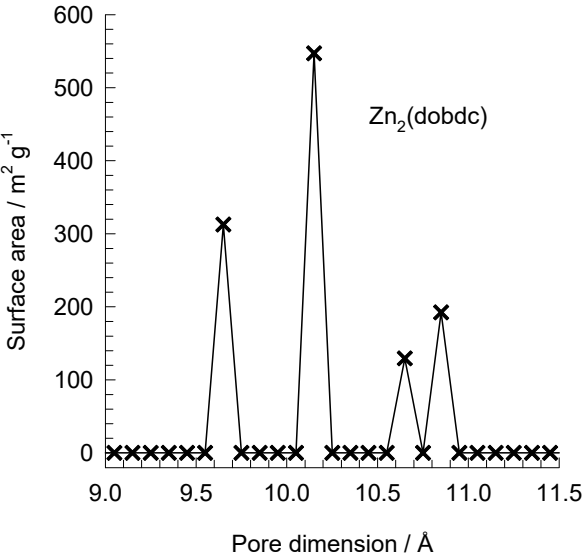
Zn$_2$(dobdc)

This plot of surface area versus pore dimension is determined using a combination of the DeLaunay triangulation method for pore dimension determination, and the procedure of Düren for determination of the surface area.

	ZnMOF-74
a /Å	25.9322
b /Å	25.9322
c /Å	6.8365
Cell volume / Å^3	3981.467
conversion factor for [molec/uc] to [mol per kg Framework]	0.3421
conversion factor for [molec/uc] to [kmol/m^3]	0.5881
ρ [kg/m3]	1219.304
MW unit cell [g/mol(framework)]	2923.473
ϕ, fractional pore volume	0.709
open space / Å^3/uc	2823.8
Pore volume / cm^3/g	0.582
Surface area /m^2/g	1176.0
DeLaunay diameter /Å	9.49

ZnMOF-74 snapshot of nC5/2MB/neo-P
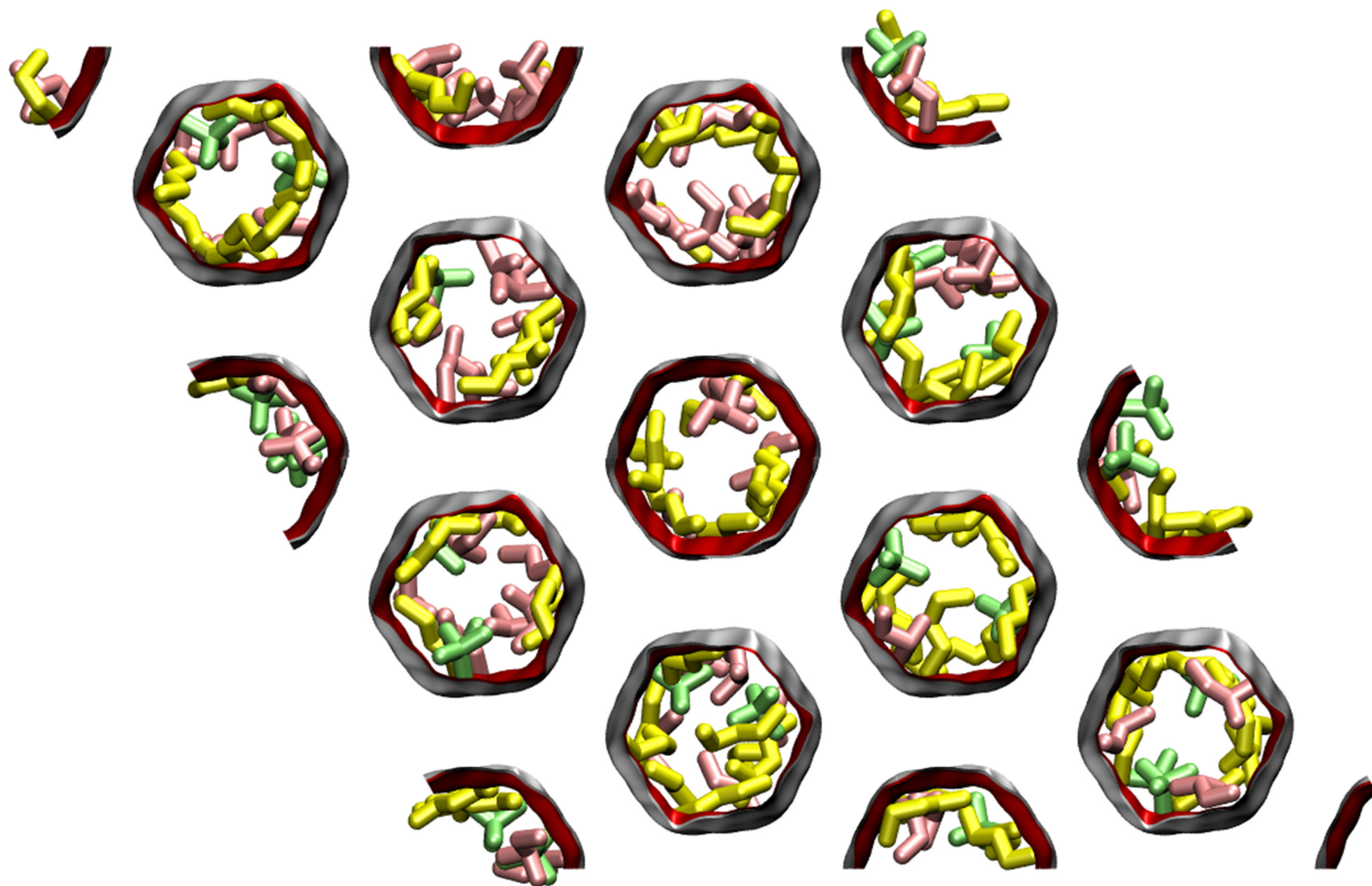
MOF-177 pore landscape
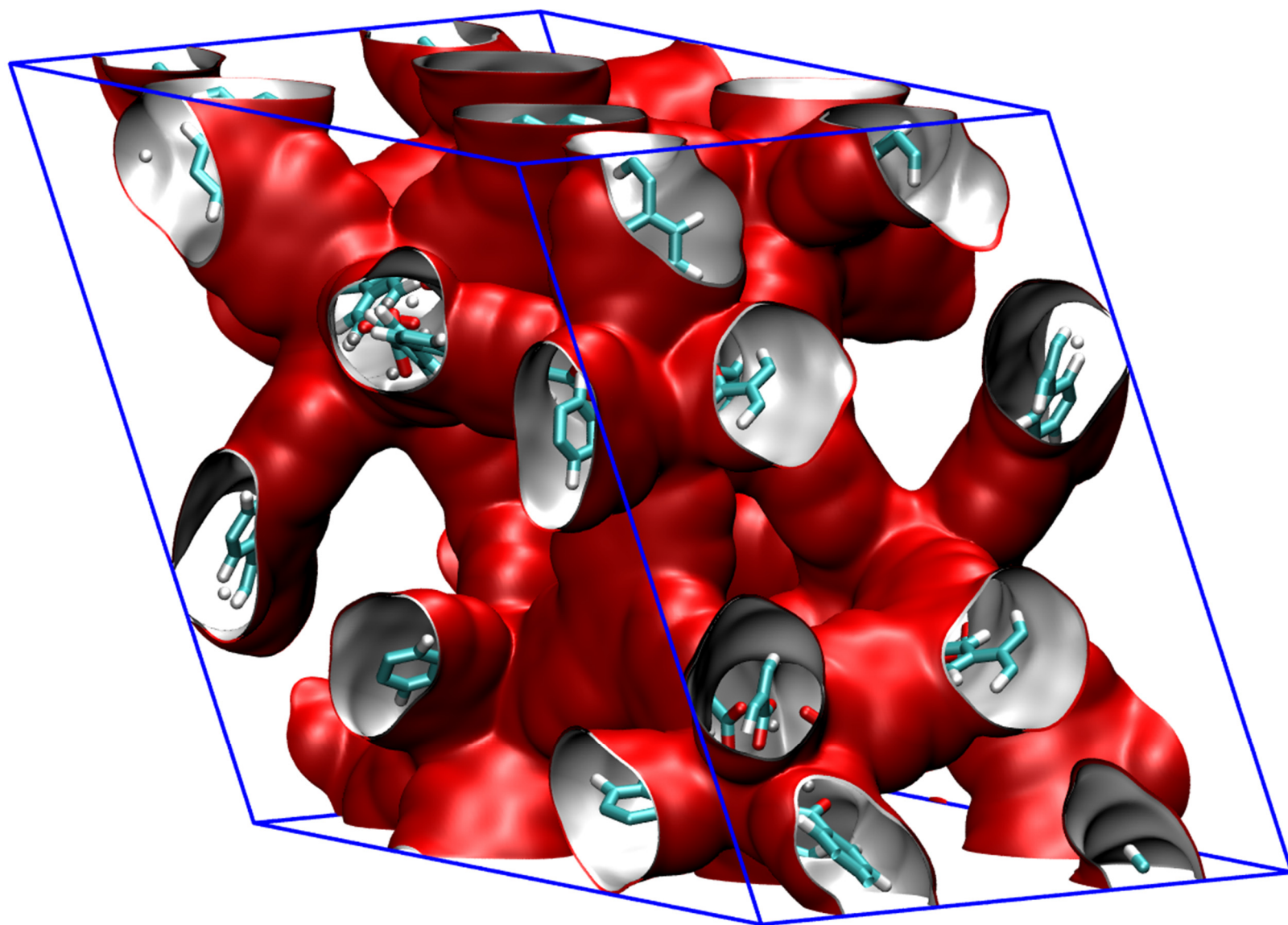
MOF-177 pore dimensions
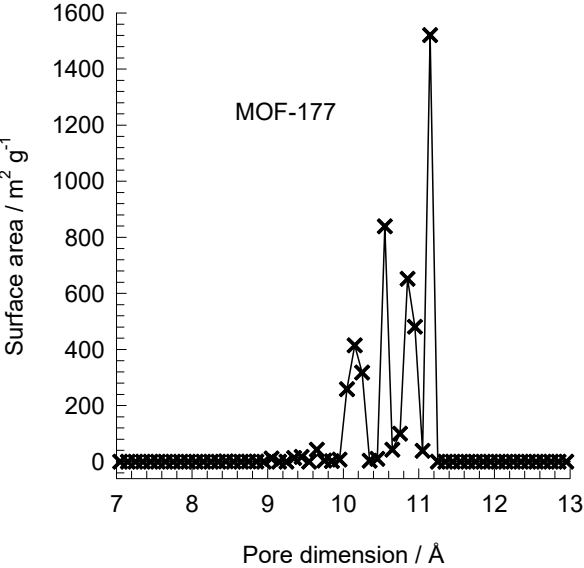
MOF-177

This plot of surface area versus pore dimension is determined using a combination of the DeLaunay triangulation method for pore dimension determination, and the procedure of Düren for determination of the surface area.

	MOF-177
a /Å	37.072
b /Å	37.072
c /Å	30.033
Cell volume / Å^3	35745.5
conversion factor for [molec/uc] to [mol per kg Framework]	0.1089
conversion factor for [molec/uc] to [kmol/m^3]	0.0553
ρ [kg/m3]	426.5952
MW unit cell [g/mol(framework)]	9182.931
ϕ, fractional pore volume	0.840
open space / Å^3/uc	30010.9
Pore volume / cm^3/g	1.968
Surface area /m^2/g	4781.0
DeLaunay diameter /Å	10.1

MOF-177 snapshots of nC6/3MP/22DMB hexane isomers

Figure S28
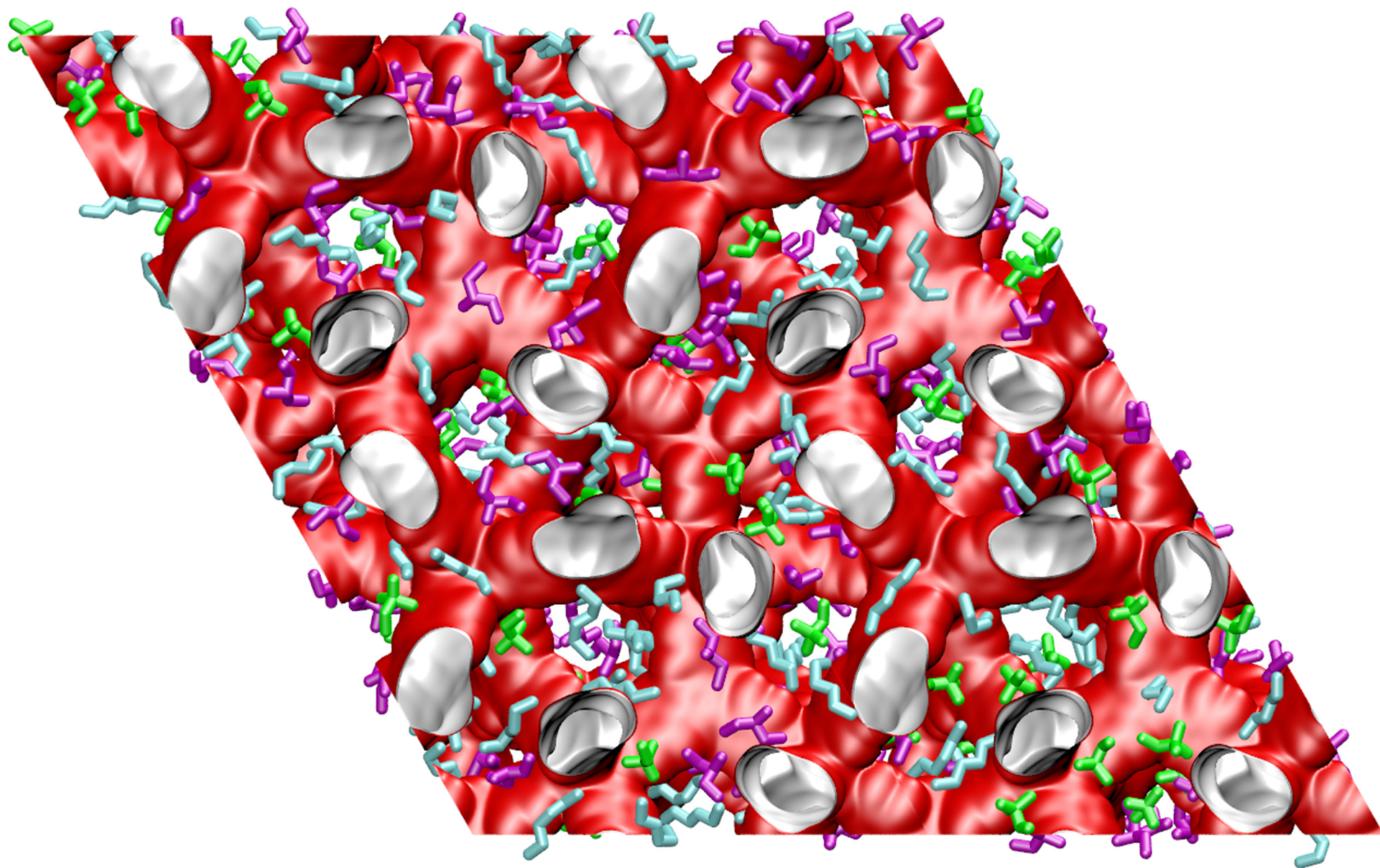
Zn(bdc)dabco
landscapes
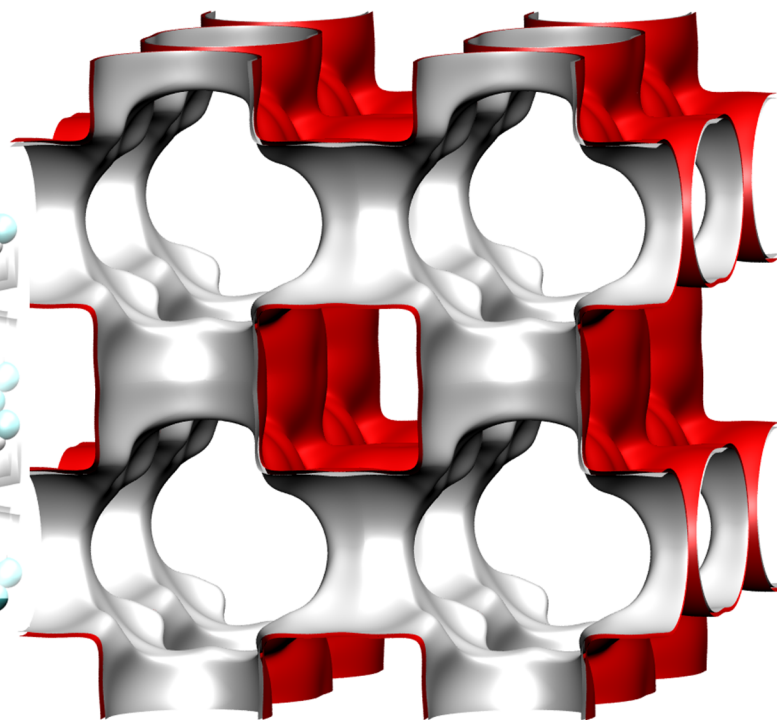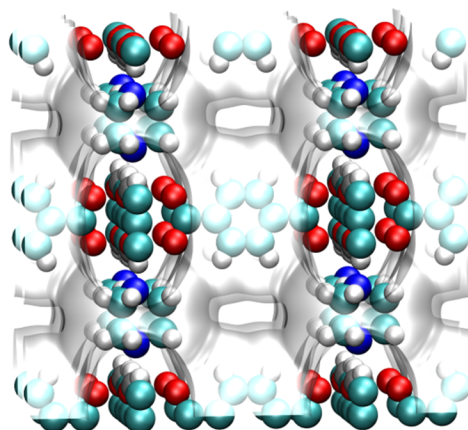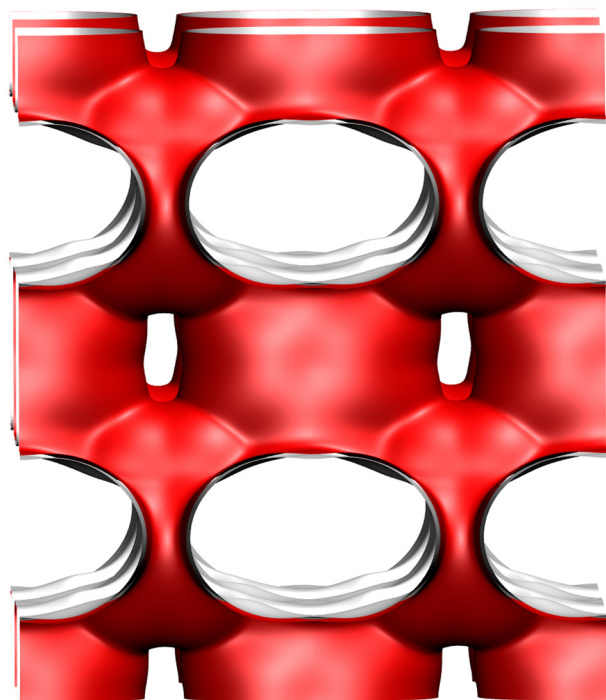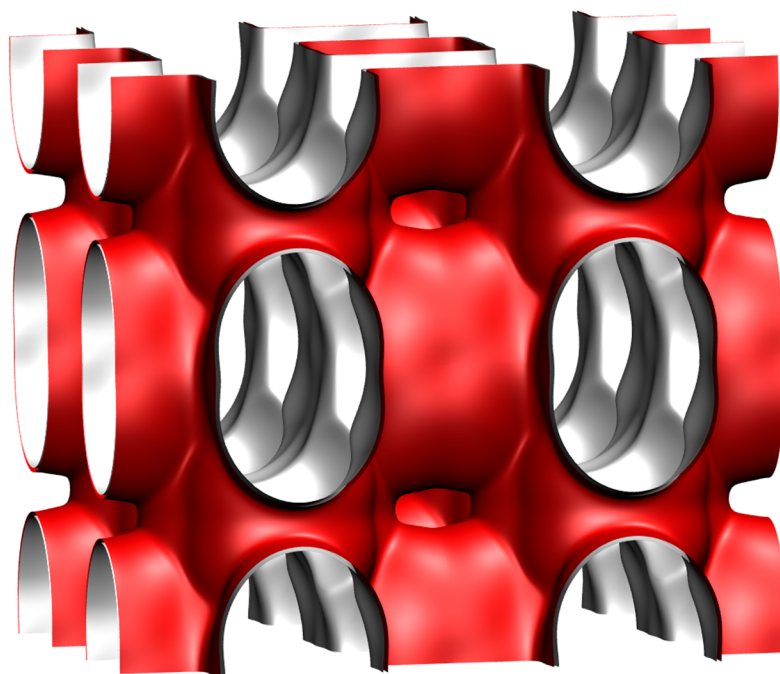
Zn(bdc)dabco
landscapes
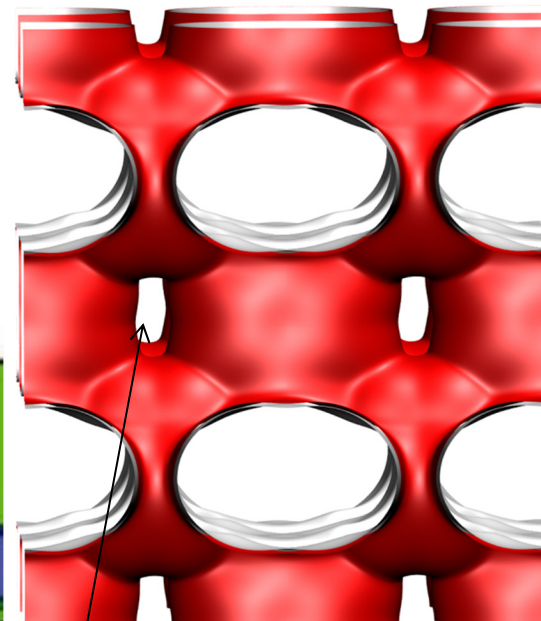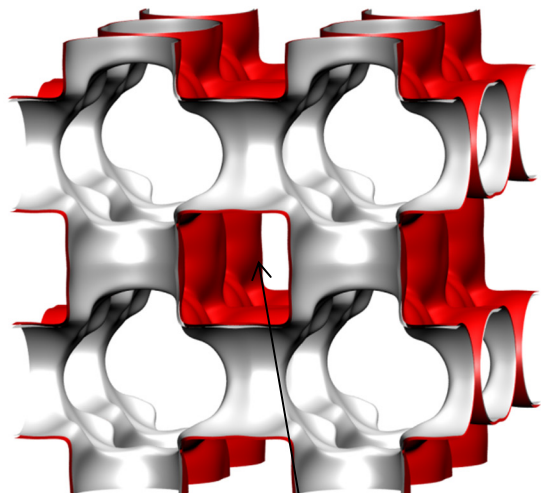
3D intersecting channels

Wide channels

7.5 Å

7.5 Å

Narrow channels

4.7 Å

3.8 Å
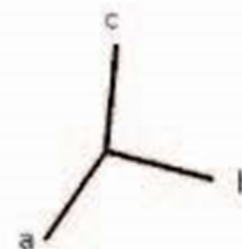
Zn(bdc)dabco pore dimensions
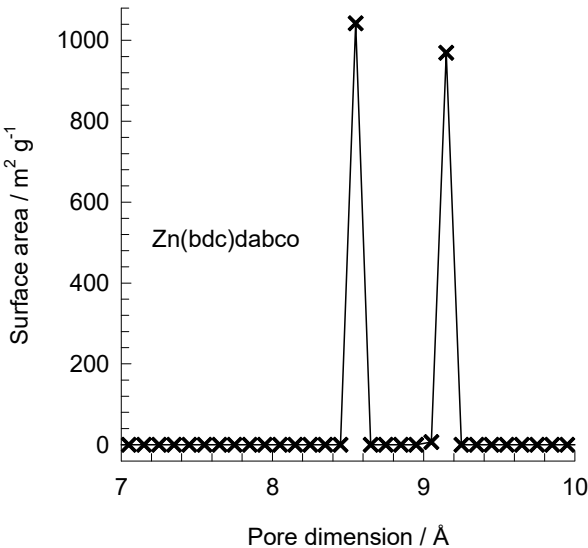
Zn(bdc)dabco

This plot of surface area versus pore dimension is determined using a combination of the DeLaunay triangulation method for pore dimension determination, and the procedure of Düren for determination of the surface area.

	Zn(bdc)dabco
a /Å	10.9288
b /Å	10.9288
c /Å	9.6084
Cell volume / Å^3	1147.615
conversion factor for [molec/uc] to [mol per kg Framework]	1.7514
conversion factor for [molec/uc] to [kmol/m^3]	2.1867
ρ [kg/m3]	826.1996
MW unit cell [g/mol(framework)]	570.9854
ϕ, fractional pore volume	0.662
open space / Å^3/uc	759.4
Pore volume / cm^3/g	0.801
Surface area /m^2/g	2022.5
DeLaunay diameter /Å	8.32

Zn(bdc)dabco snapshot of nC5/2MB/neo-P mix
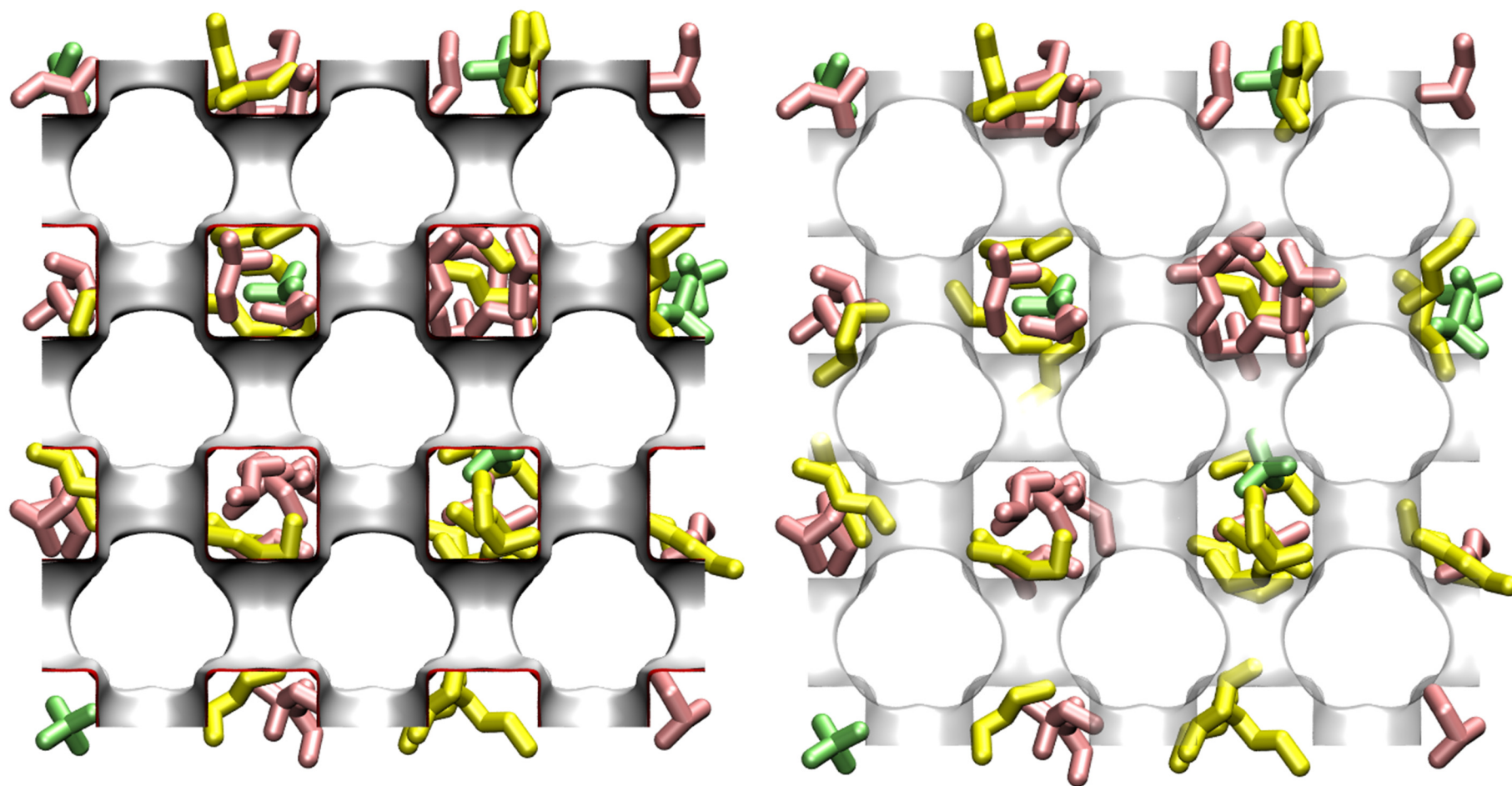
ZIF-77

pore landscapes
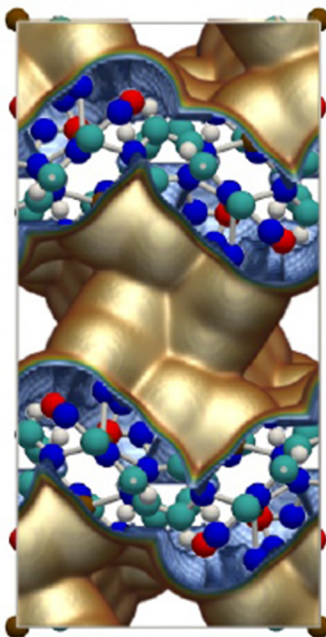
Single unit cell: x-y view
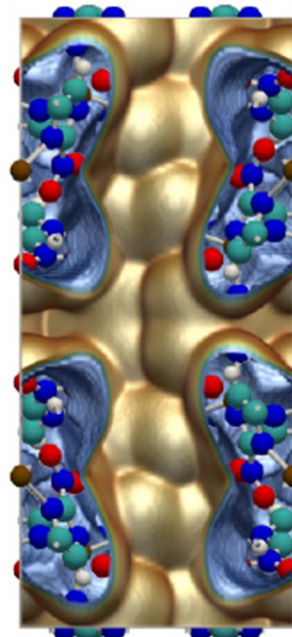
Single unit cell: x-z view
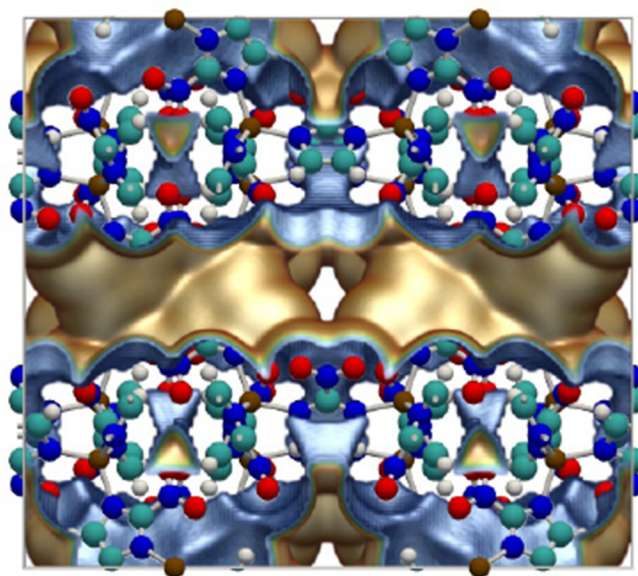
Single unit cell: y-z view
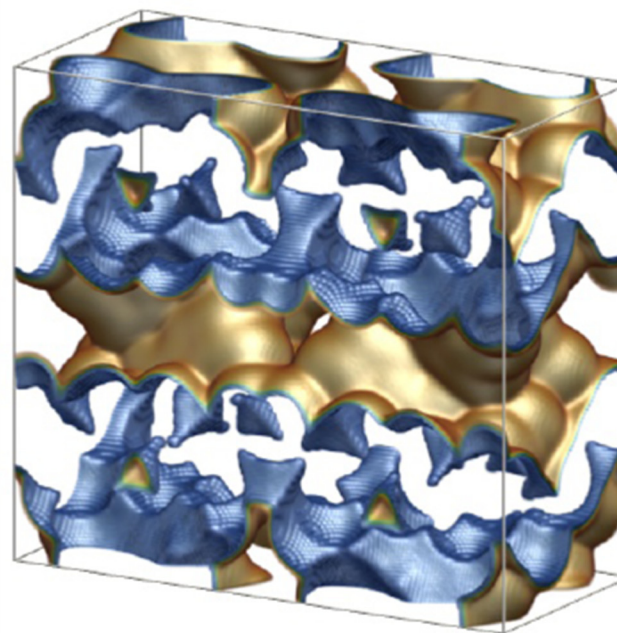
Single unit cell: x-y-z view

ZIF-77 dimensions

	ZIF-77
a /Å	11.1248
b /Å	22.3469
c /Å	24.9087
ρ [kg/m3]	1552.86
MW unit cell [g/mol(framework)]	2730.182
ϕ, fractional pore volume	0.293
Pore volume / cm^3/g	0.1889

ZIF-8 pore landscapes

There are 2 cages per unit cell. To convert from molecules per cage to mol kg^{-1}, multiply by 0.7325.

There are 2 cages per unit cell. The volume of one ZIF-8 cage is 1168 Å^3, significantly larger than that of a single cage of DDR (278 Å^3), or FAU (786 Å^3).
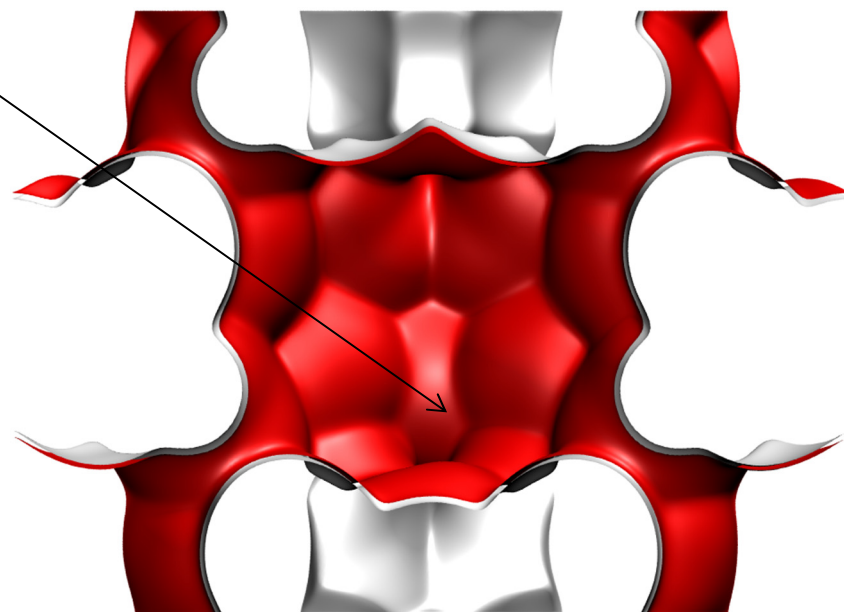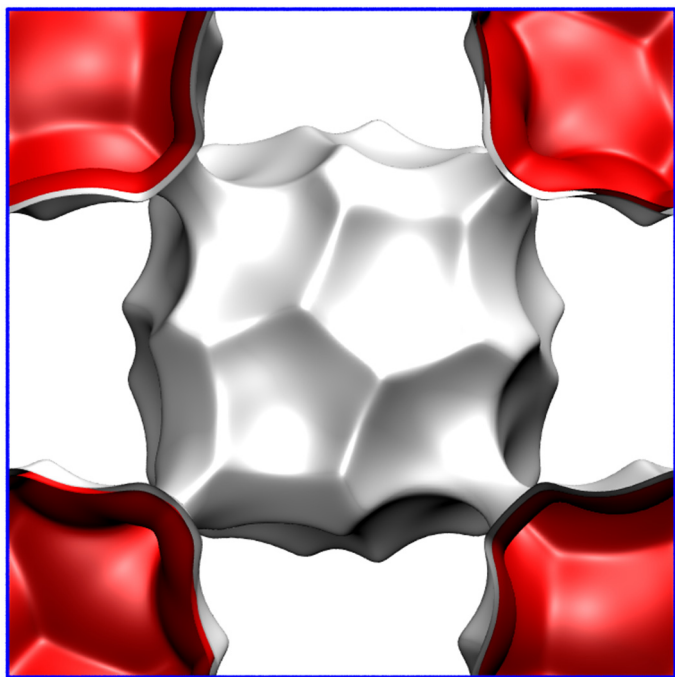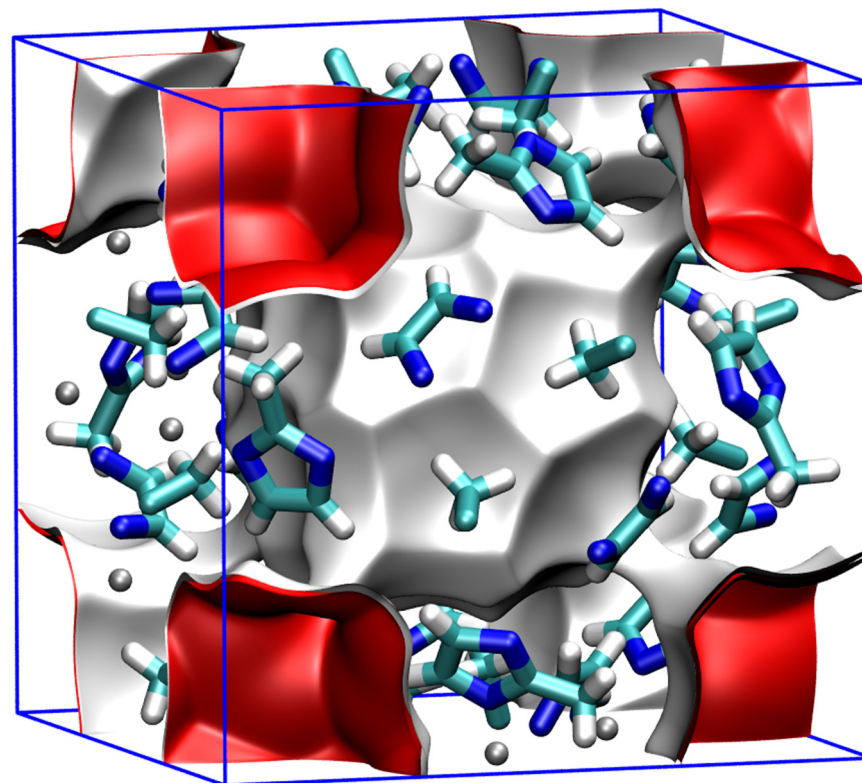
ZIF-8 dimensions
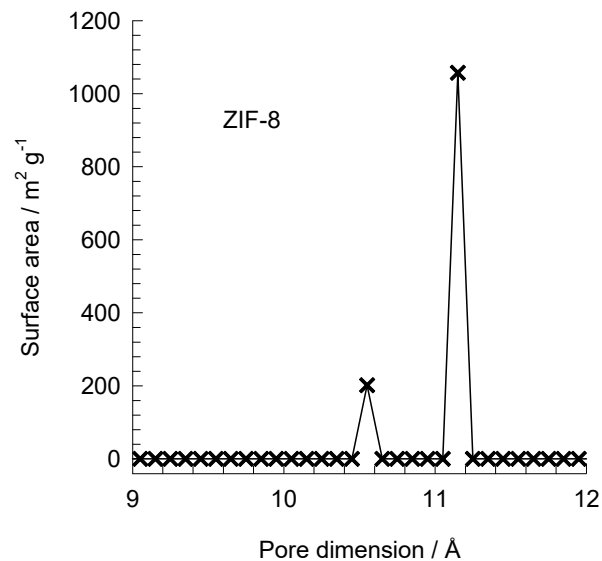
This plot of surface area versus pore dimension is determined using a combination of the DeLaunay triangulation method for pore dimension determination, and the procedure of Düren for determination of the surface area.

	ZIF-8
a /Å	16.991
b /Å	16.991
c /Å	16.991
Cell volume / Å^3	4905.201
conversion factor for [molec/uc] to [mol per kg Framework]	0.3663
conversion factor for [molec/uc] to [kmol/m^3]	0.7106
ρ [kg/m3]	924.253
MW unit cell [g/mol(framework)]	2730.182
ϕ, fractional pore volume	0.476
open space / Å^3/uc	2337.0
Pore volume / cm^3/g	0.515
Surface area /m^2/g	1164.7
DeLaunay diameter /Å	3.26

MFI CBMC simulations of pentanes adsorption vs IAST

Figure S37

(a) Unary CBMC vs DLF fit

(b) CBMC pentanes mixture vs IAST

(c) nC5/2MB selectivity

(d) 2MB/neo-P selectivity

(a) Unary fits

Figure S38

(b) CBMC mixture vs IAST

(c) CBMC mixture

Adsorption of hexane isomers in MFI zeolite: CBMC vs IAST

3MP prefers to locate at the intersections

The di-branched 22DMB can only locate at the intersections
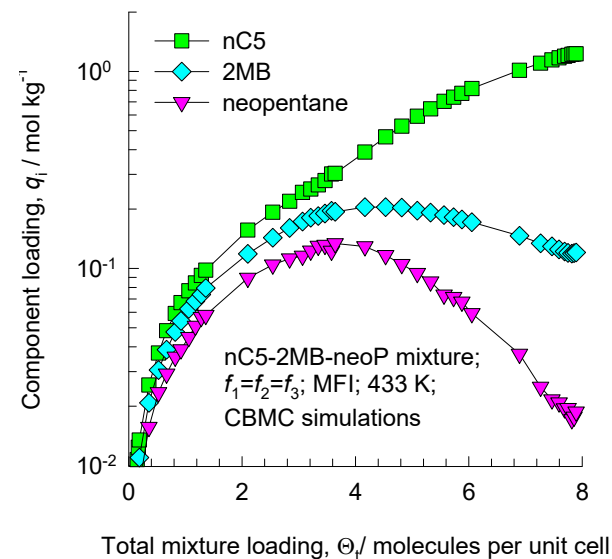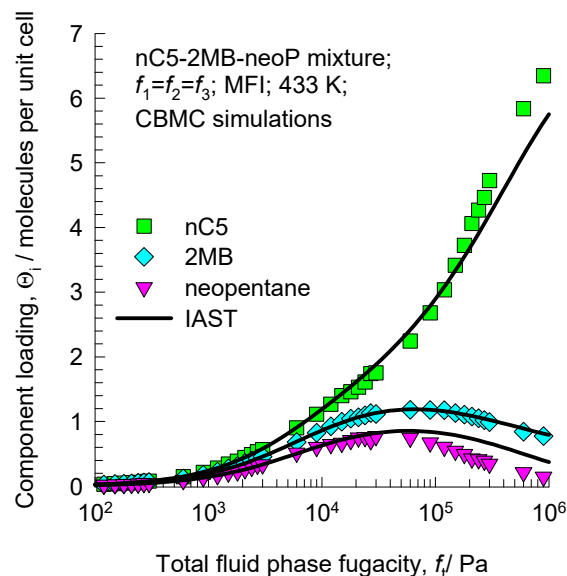
Adsorption of hexane isomers in MFI zeolite: CBMC vs IAST
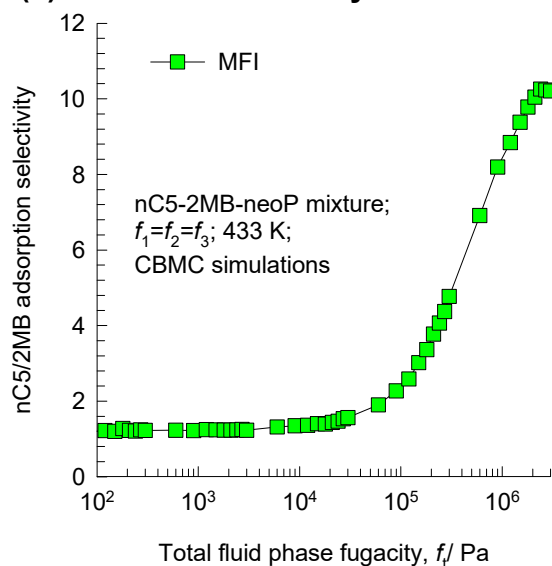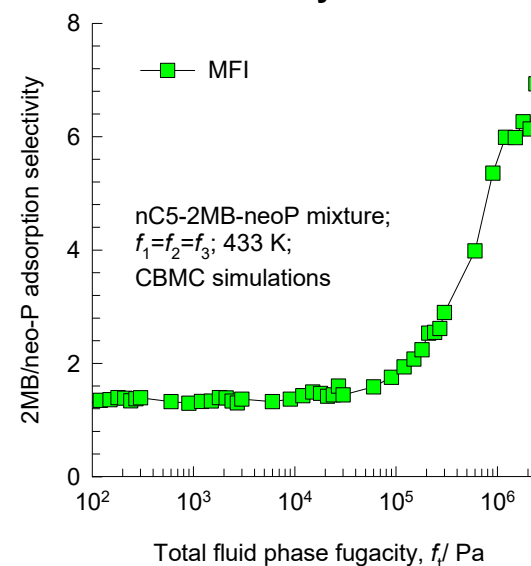
(a) Unary fits
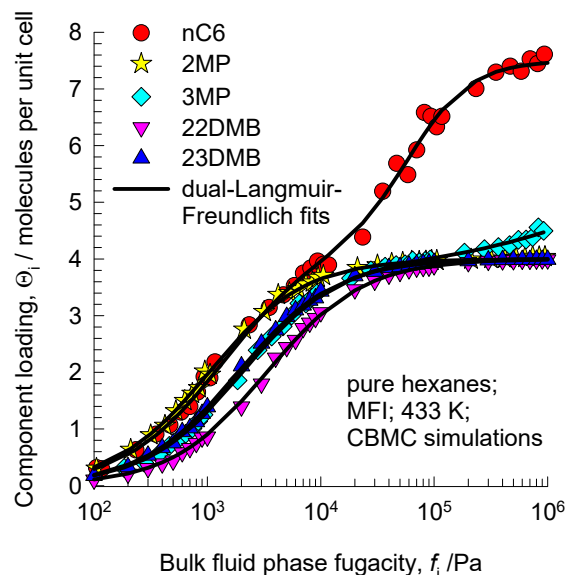
(b) CBMC mixture

(c) CBMC mixture vs IAST

BeBTB CBMC simulations of unary and mixture adsorption

(b) CBMC pentanes mixture

nC5-2MB-neoP mixture;
$f_1=f_2=f_3$; BeBTB; 433 K;
CBMC simulations

- nC5
- 2MB
- neopentane

Component loading, q_i / mol kg^{-1}

Total fluid phase fugacity, f_t / Pa

(c) nC5/2MB selectivity

BeBTB

nC5-2MB-neoP mixture;
$f_1=f_2=f_3$; 433 K; CBMC

nC5/2MB adsorption selectivity

Total fluid phase fugacity, f_t / Pa

(d) 2MB/neo-P selectivity

nC5-2MB-neoP mixture;
$f_1=f_2=f_3$; 433 K; CBMC

BeBTB

2MB/neo-P adsorption selectivity

Total fluid phase fugacity, f_t / Pa

Co(BDP) CBMC simulations of unary and mixture adsorption vs IAST

(a) Unary CBMC vs DLF fit

nC5
2MB
neopentane
dual-Langmuir-Freundlich fits

pure nC5;
pure 2MB;
pure neo-pentane;
Co(BDP); 433 K;
CBMC simulations

Component loading, q_i / mol kg^{-1}

Bulk fluid phase fugacity, f_i /Pa

(b) CBMC pentanes mixture vs IAST

nC5-2MB-neoP mixture;
$f_1=f_2=f_3$; Co(BDP); 433 K;
CBMC simulations

nC5
2MB
neopentane
IAST

Component loading, q_i / mol kg^{-1}

Total fluid phase fugacity, f_t/ Pa

(c) nC5/2MB selectivity

Co(BDP)

nC5-2MB-neoP mixture;
$f_1=f_2=f_3$; 433 K; CBMC

nC5/2MB adsorption selectivity

Total fluid phase fugacity, f_t/ Pa

(d) 2MB/neo-P selectivity

Co(BDP)

nC5-2MB-neoP mixture;
$f_1=f_2=f_3$; 433 K; CBMC

2MB/neo-P adsorption selectivity

Total fluid phase fugacity, f_t/ Pa

CuBTT CBMC simulations of unary and mixture adsorption

(b) CBMC pentanes mixture

(c) nC5/2MB selectivity
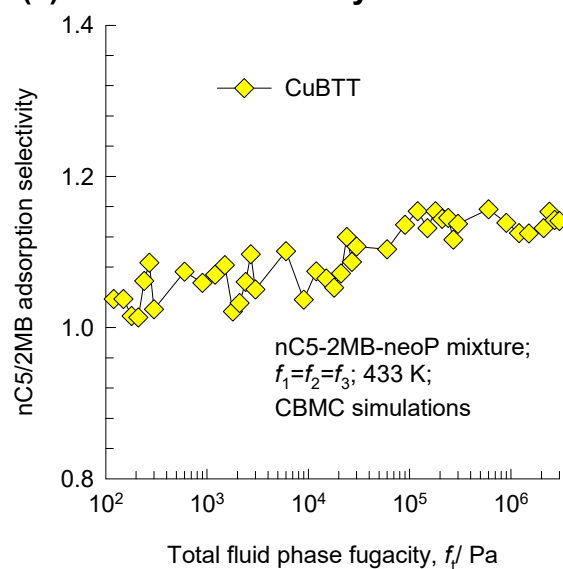
(d) 2MB/neo-P selectivity
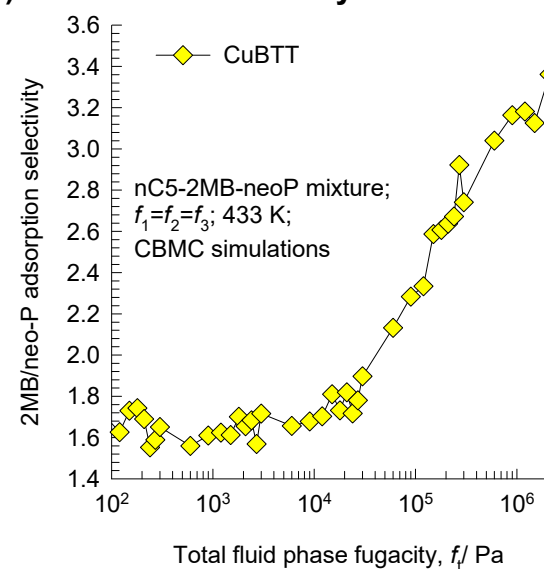
Fe$_2$(BDP)$_3$ CBMC simulations of unary C5 adsorption

(a) Unary CBMC vs DLF fit

(b) Heats of adsorption

unary pentanes;
Fe$_2$(BDP)$_3$; 433 K;
CBMC

dual-site
Langmuir fits
- nC5
- 2MB
- neo-P

Component loading, q_i / mol kg^{-1}

Bulk fluid phase fugacity, f_i /Pa

Heat of adsorption /kJ mol^{-1}

- nC5
- 2MB
- neo-P

unary pentanes; Fe$_2$(BDP)$_3$; 433 K

Component loading / mol kg^{-1}
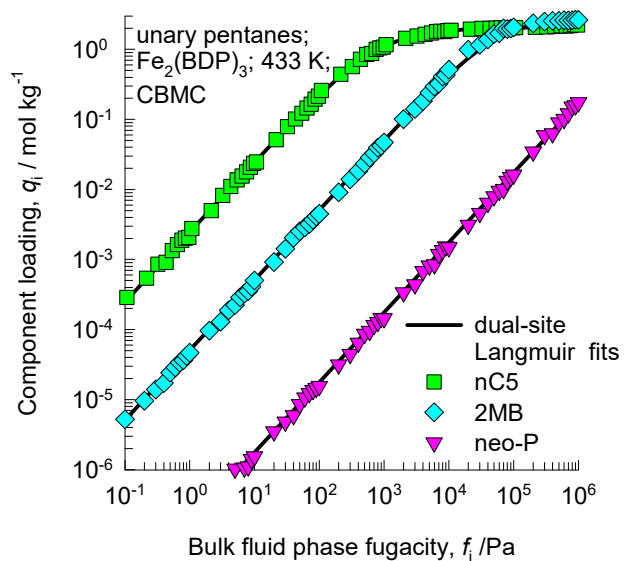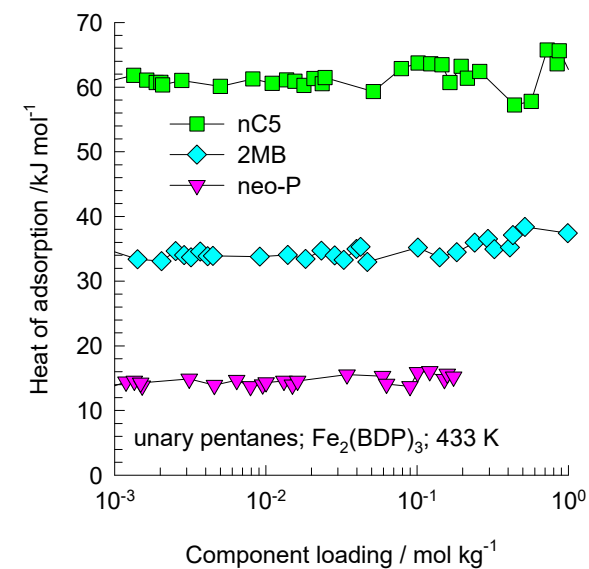
Fe$_2$(BDP)$_3$ CBMC simulations of unary C6, C7 adsorption

(a) Unary hexanes CBMC vs DL fit
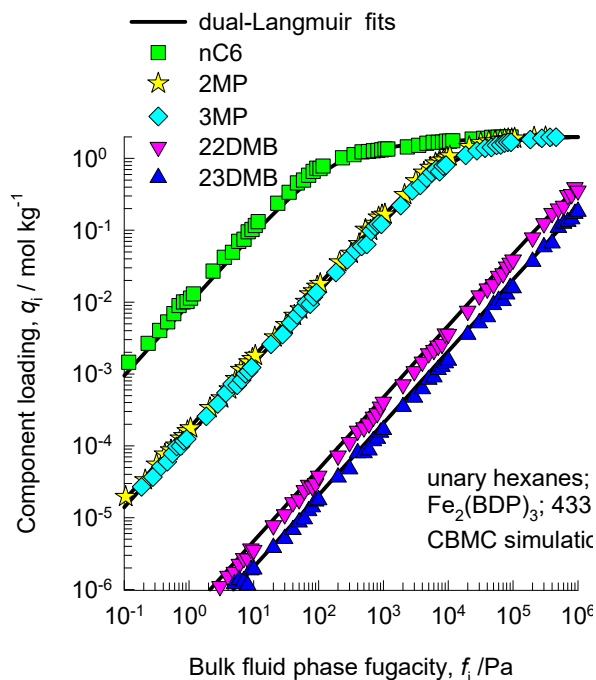
(b) CBMC unary heptanes vs DLT
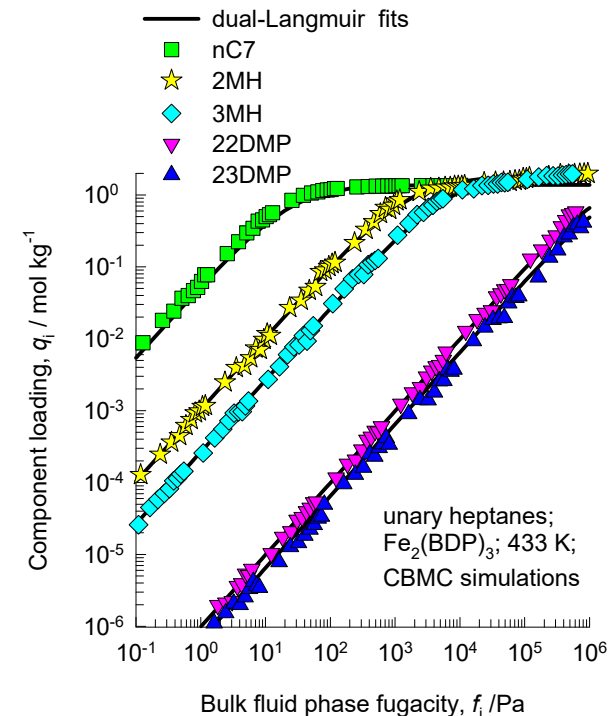
(b) Heats of adsorption of hexanes
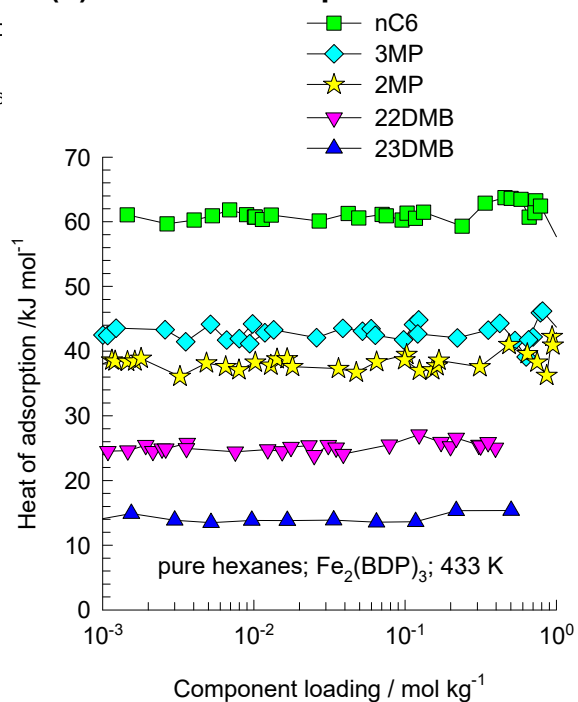
Fe$_2$(BDP)$_3$ CBMC simulations mixture adsorption vs IAST

(a) CBMC pentanes mixture vs IAST

nC5/2MB/neo-P mixture; $f_1=f_2=f_3$; Fe$_2$(BDP)$_3$; 433 K; CBMC

(b) nC5/2MB selectivity

nC5-2MB-neoP mixture; $f_1=f_2=f_3$; 433 K; CBMC

(c) 2MB/neo-P selectivity

nC5-2MB-neoP mixture; $f_1=f_2=f_3$; 433 K; CBMC
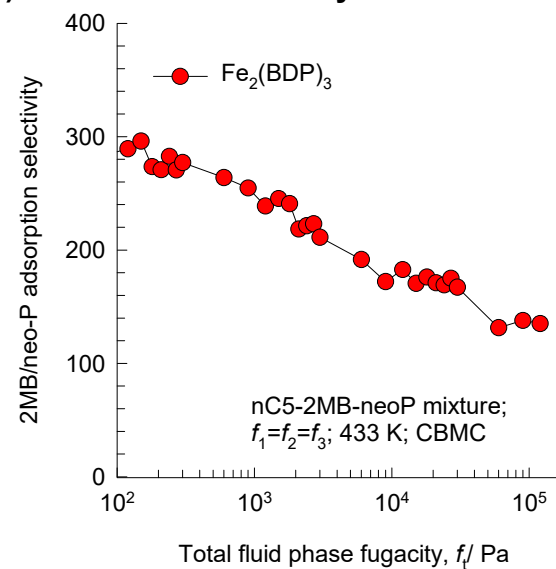
Fe$_2$(BDP)$_3$ CBMC simulations of mixture adsorption vs IAST

(a) CBMC C6 mixture vs IAST
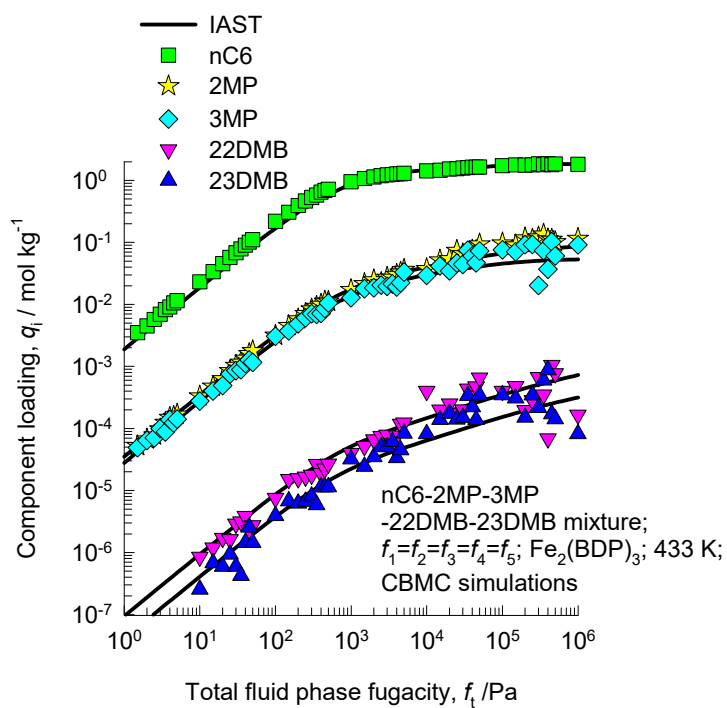
(b) CBMC C5, C6 mixture vs IAST

nC6-2MP-3MP-22DMB-23DMB mixture; $f_1=f_2=f_3=f_4=f_5$; Fe$_2$(BDP)$_3$; 433 K; CBMC simulations

C5/C6 mixture; CBMC simulations; Fe$_2$(BDP)$_3$; 433 K
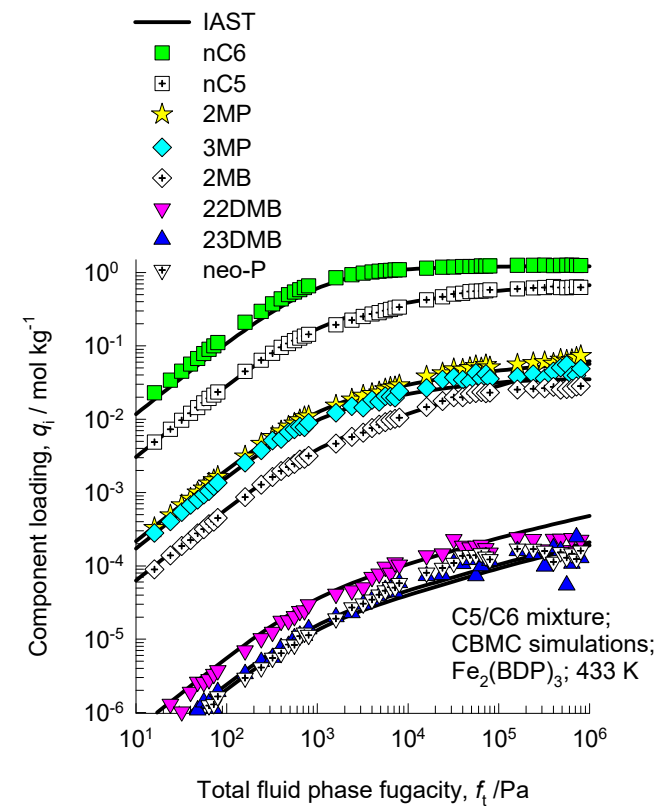
Fe$_2$(BDP)$_3$ CBMC mixture adsorption vs IAST

Legend:
- IAST
- nC6
- nC5
- 2MP
- 3MP
- 2MB
- 22DMB
- 23DMB
- neo-P
- nC7
- 2MH
- 3MH
- 22DMP
- 23DMP

C5/C6/C7 mixture;
CBMC simulations;
Fe$_2$(BDP)$_3$; 433 K

Component loading, q_i / mol kg^{-1}

Total fluid phase fugacity, f_t /Pa
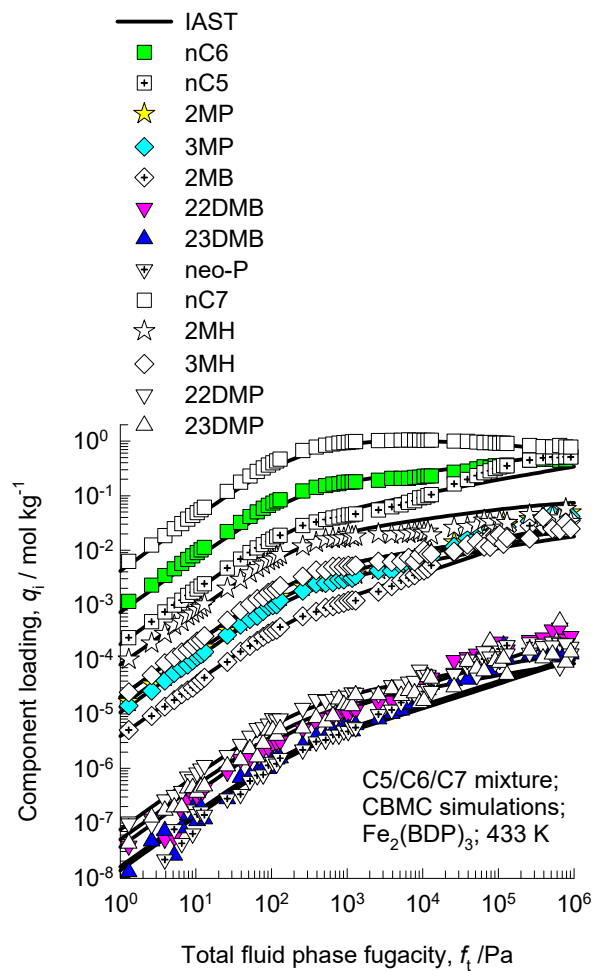
IRMOF-1 CBMC pentanes mixture simulations

(b) CBMC mixture

nC5-2MB-neoP mixture;
$f_1=f_2=f_3$; IRMOF-1; 433 K;
CBMC simulations

- ☐ nC5
- ◇ 2MB
- ▽ neopentane

Component loading, q_i / mol kg^{-1}

Total fluid phase fugacity, f_t / Pa

(c) nC5/2MB selectivity

▲ IRMOF-1

nC5-2MB-neoP mixture;
$f_1=f_2=f_3$; 433 K;
CBMC simulations

nC5/2MB adsorption selectivity

Total fluid phase fugacity, f_t/ Pa

(d) 2MB/neo-P selectivity

▲ IRMOF-1

nC5-2MB-neoP mixture;
$f_1=f_2=f_3$; 433 K;
CBMC simulations

2MB/neo-P adsorption selectivity

Total fluid phase fugacity, f_t/ Pa
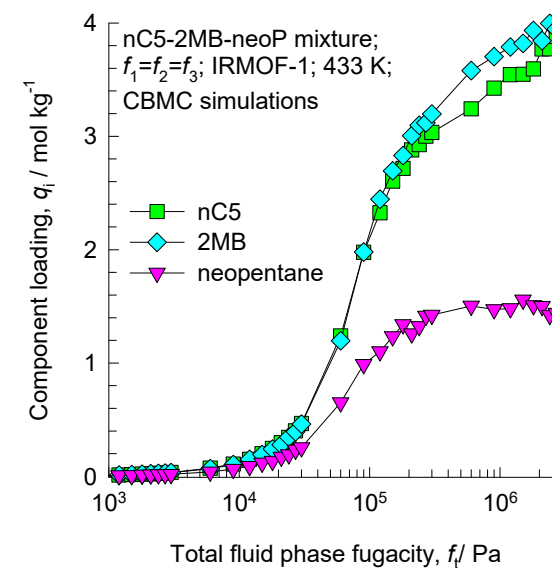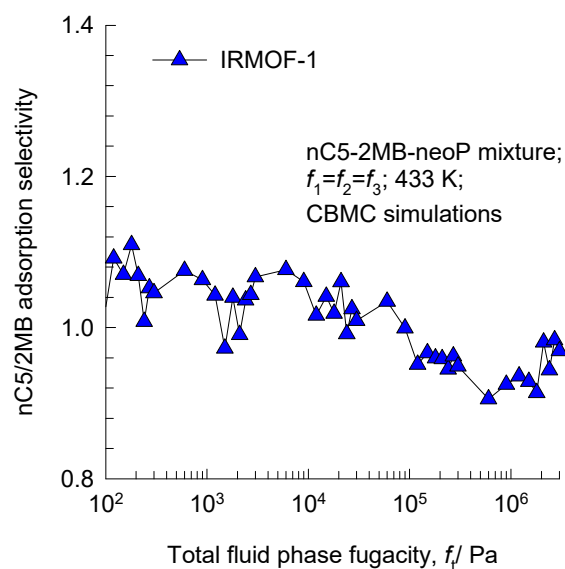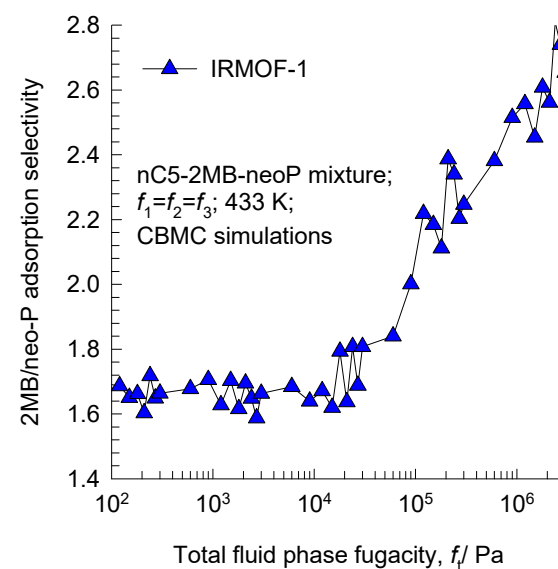
MgMOF-74 CBMC pentanes mixture simulation results

(a) Unary CBMC vs DLF fit
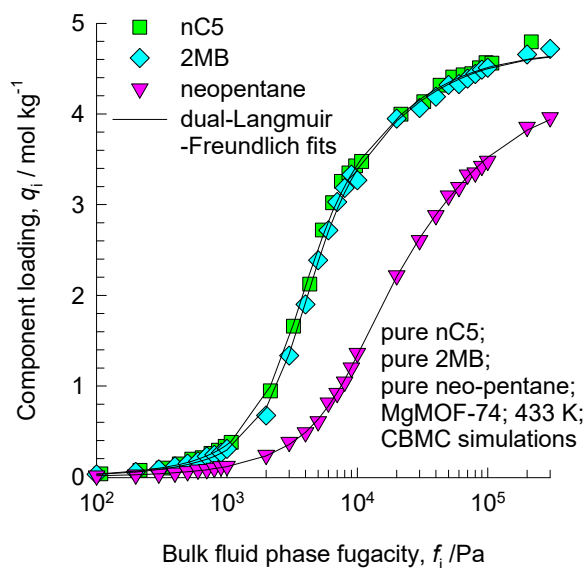
(b) CBMC mixture vs IAST
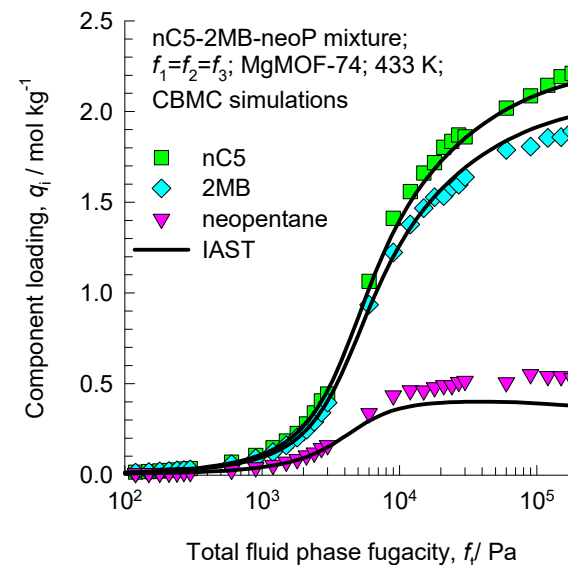
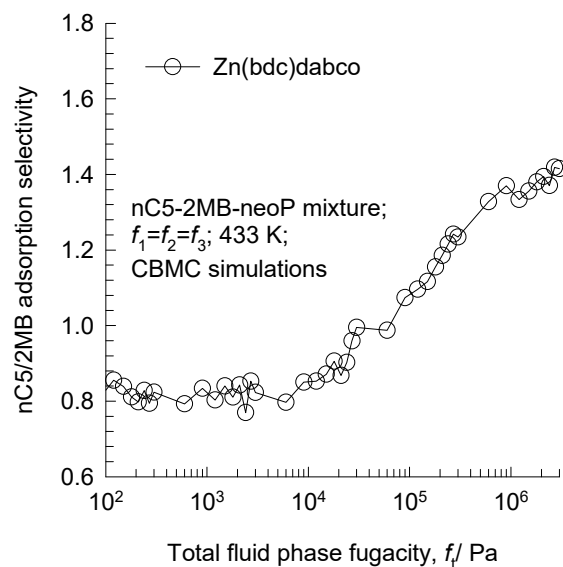**(c) nC5/2MB selectivity**
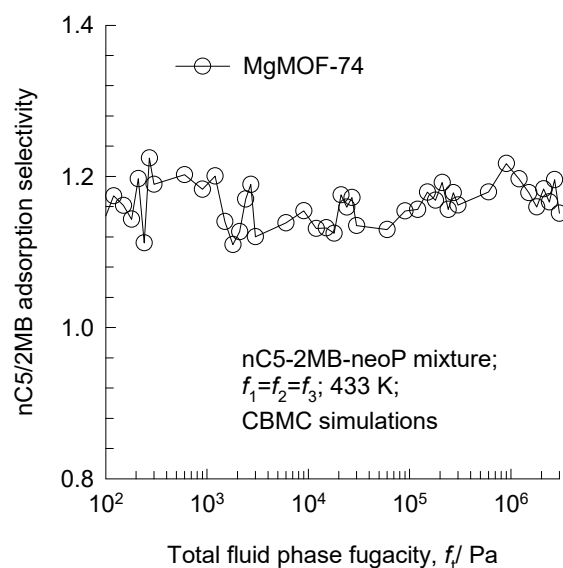
(d) 2MB/neo-P selectivity

ZnMOF-74 CBMC pentanes mixture simulation results

(a) Unary CBMC vs DLF fit

Legend:
- nC5
- 2MB
- neopentane
- dual-Langmuir-Freundlich fits

pure nC5;
pure 2MB;
pure neo-pentane;
ZnMOF-74; 433 K;
CBMC simulations

Axis labels: Component loading, q_i / mol kg^{-1} ; Bulk fluid phase fugacity, f_i /Pa

(b) CBMC mixture vs IAST

nC5-2MB-neoP mixture;
$f_1 = f_2 = f_3$; ZnMOF-74; 433 K;
CBMC simulations

Legend:
- nC5
- 2MB
- neopentane
- IAST

Axis labels: Component loading, q_i / mol kg^{-1} ; Total fluid phase fugacity, f_t/ Pa

(c) nC5/2MB selectivity

ZnMOF-74

nC5-2MB-neoP mixture;
$f_1 = f_2 = f_3$; 433 K;
CBMC simulations

Axis labels: nC5/2MB adsorption selectivity ; Total fluid phase fugacity, f_t/ Pa

(d) 2MB/neo-P selectivity

ZnMOF-74

nC5-2MB-neoP mixture;
$f_1 = f_2 = f_3$; 433 K;
CBMC simulations

Axis labels: 2MB/neo-P adsorption selectivity ; Total fluid phase fugacity, f_t/ Pa

MOF-177 CBMC pentanes mixture simulations

(a) Unary CBMC vs DLF fit
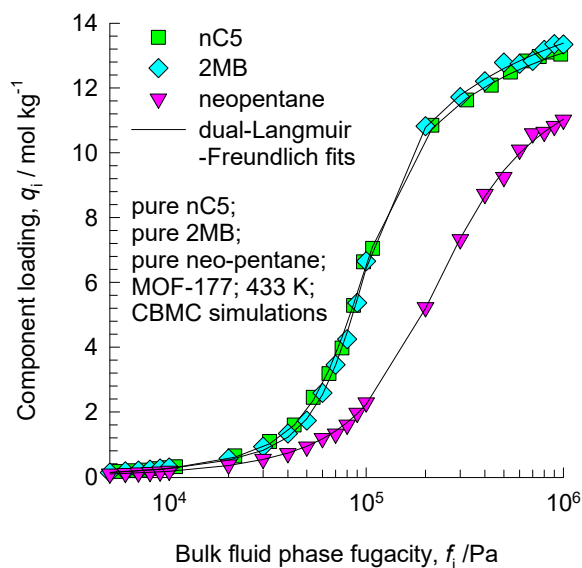
(b) CBMC mixture vs IAST
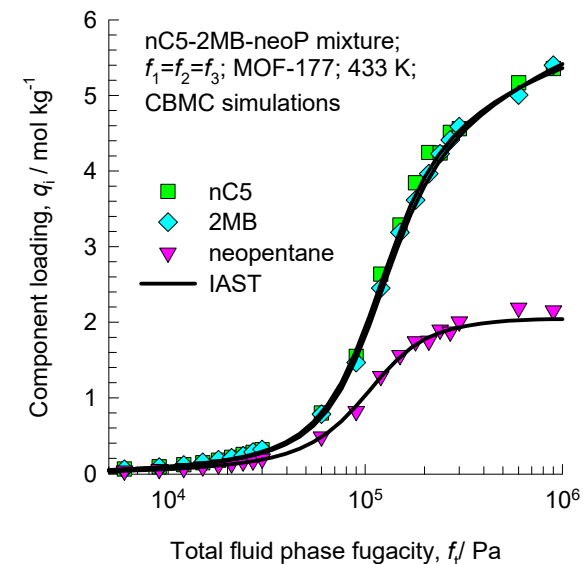
(c) nC5/2MB selectivity
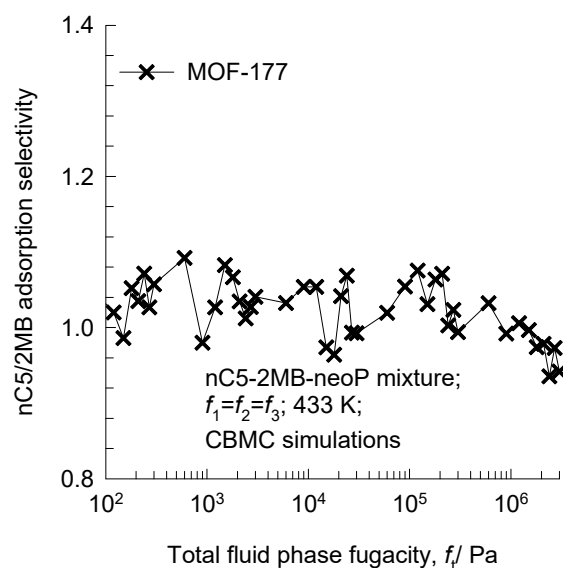
(d) 2MB/neo-P selectivity
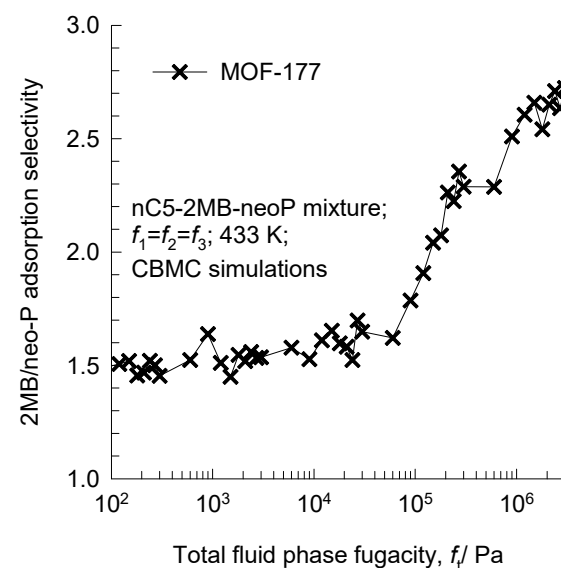
Zn(bdc)dabco CBMC pentanes mixture simulation results

(b) CBMC mixture

nC5-2MB-neoP mixture; $f_1=f_2=f_3$; Zn(bdc)dabco; 433 K; CBMC simulations

- nC5
- 2MB
- neopentane

(c) nC5/2MB selectivity

Zn(bdc)dabco

nC5-2MB-neoP mixture; $f_1=f_2=f_3$; 433 K; CBMC simulations

(d) 2MB/neo-P selectivity

Zn(bdc)dabco

nC5-2MB-neoP mixture; $f_1=f_2=f_3$; 433 K; CBMC simulations
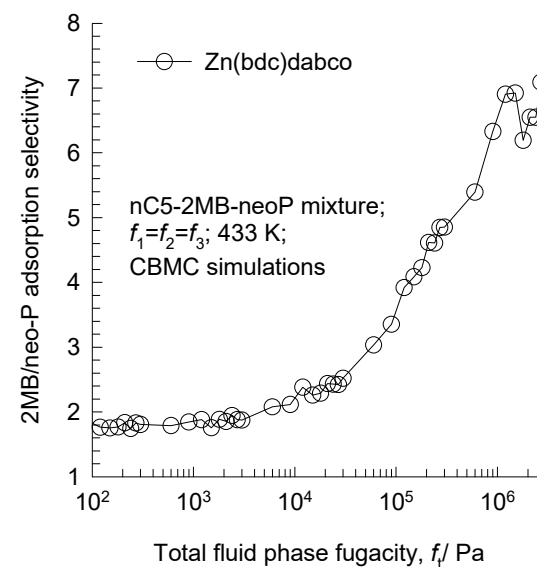
ZIF-77 CBMC simulations C5 isomers

Figure S53

(a) Unary CBMC vs DL fit
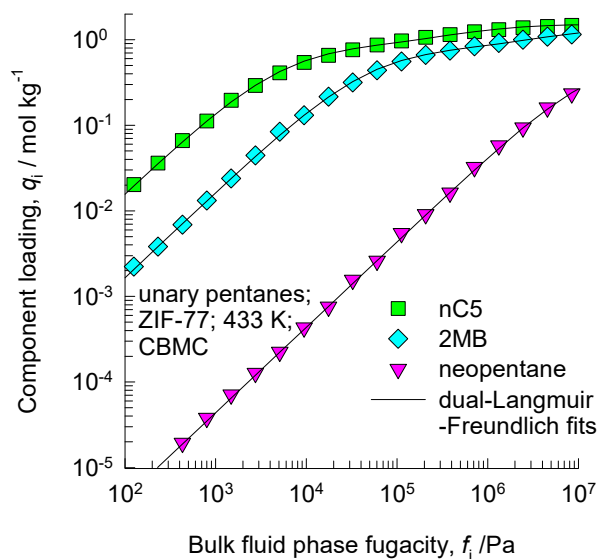
(b) IAST nC5/2MB/neo-P mixture
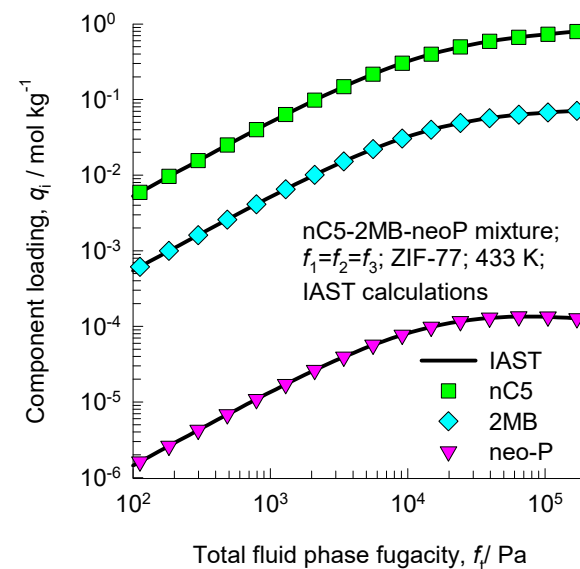
(c) nC5/2MB selectivity
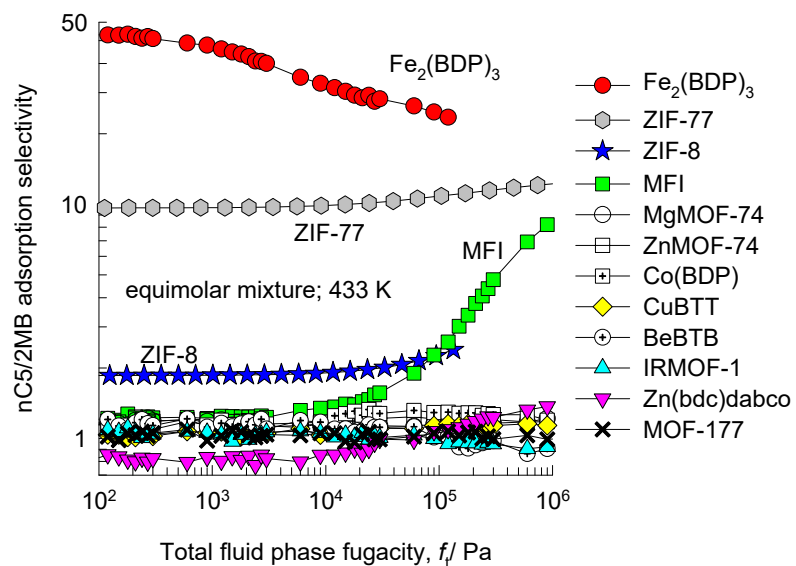
(d) 2MB/neo-P selectivity
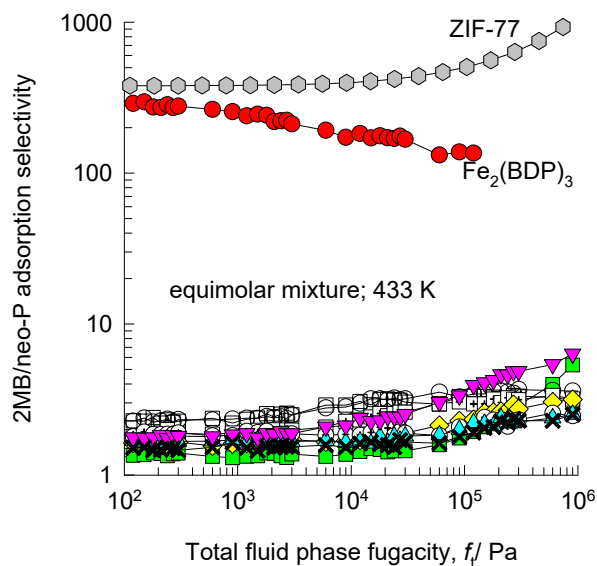
ZIF-77 CBMC simulations C6 isomers

(a) Unary CBMC vs DL fit

(b) CBMC vs IAST 5-component C6 isomers mixture

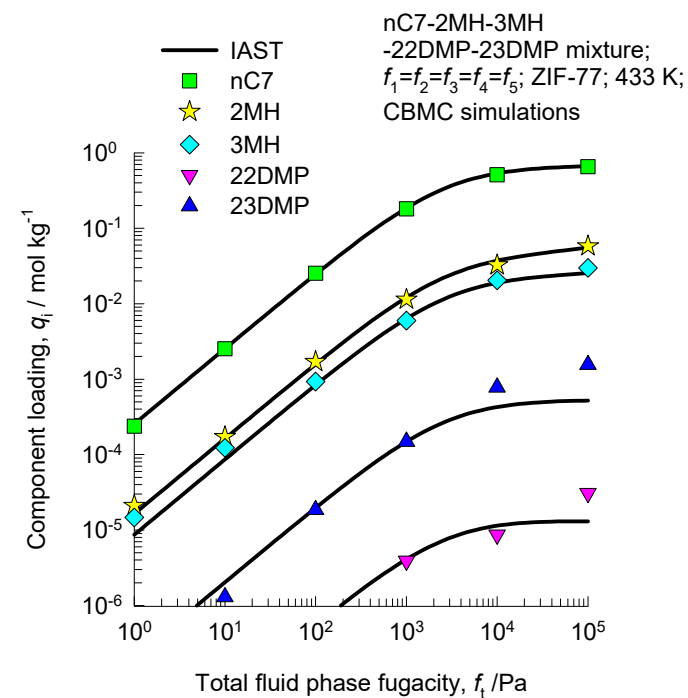

pure hexanes;
ZIF-77; 433 K;
CBMC simulations

nC6-2MP-3MP
-22DMB-23DMB mixture;
$f_1=f_2=f_3=f_4=f_5$; ZIF-77; 433 K;
CBMC simulations
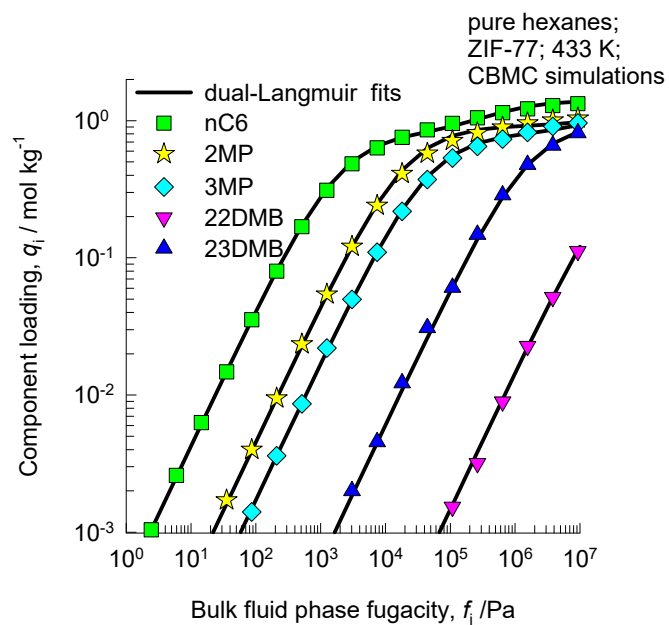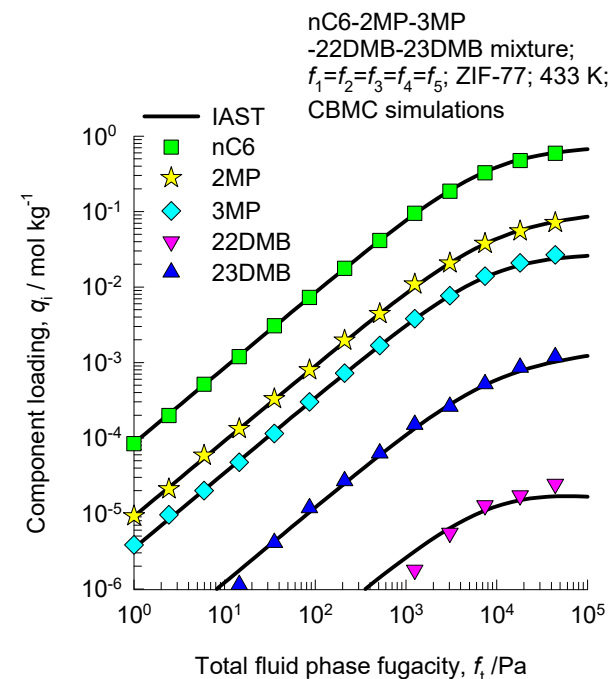
ZIF-77 CBMC simulations C7 isomers

(a) Unary CBMC vs DL fit

(b) CBMC vs IAST 5-component C6 isomers mixture

pure heptanes;
ZIF-77; 433 K;
CBMC simulations

Legend (a):
- dual-Langmuir fits
- nC7
- 2MH
- 3MH
- 22DMP
- 23DMP

Axes (a): Component loading, q_i / mol kg^{-1} vs Bulk fluid phase fugacity, f_i /Pa

nC7-2MH-3MH
-22DMP-23DMP mixture;
$f_1=f_2=f_3=f_4=f_5$; ZIF-77; 433 K;
CBMC simulations

Legend (b):
- IAST
- nC7
- 2MH
- 3MH
- 22DMP
- 23DMP

Axes (b): Component loading, q_i / mol kg^{-1} vs Total fluid phase fugacity, f_t /Pa
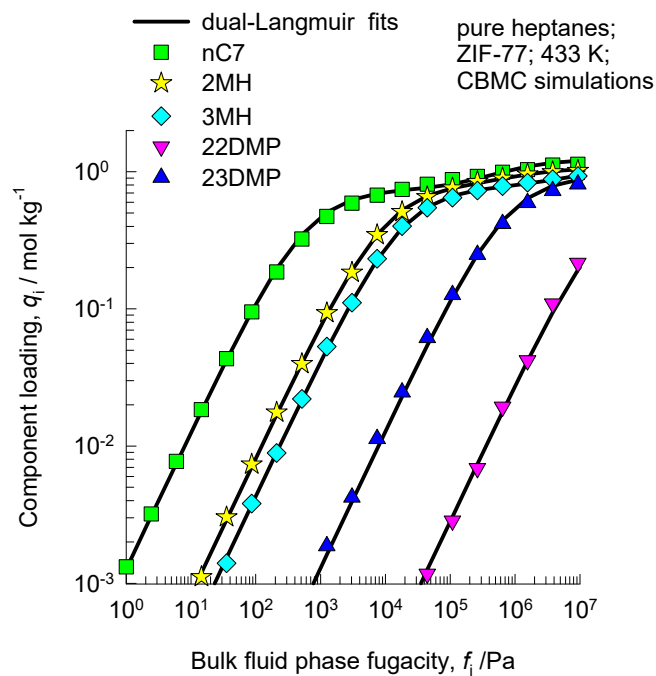
ZIF-8 IAST calculations for nC5/2MB separation

Figure S56

(a) Unary Langmuir fits, from Zhang expt data
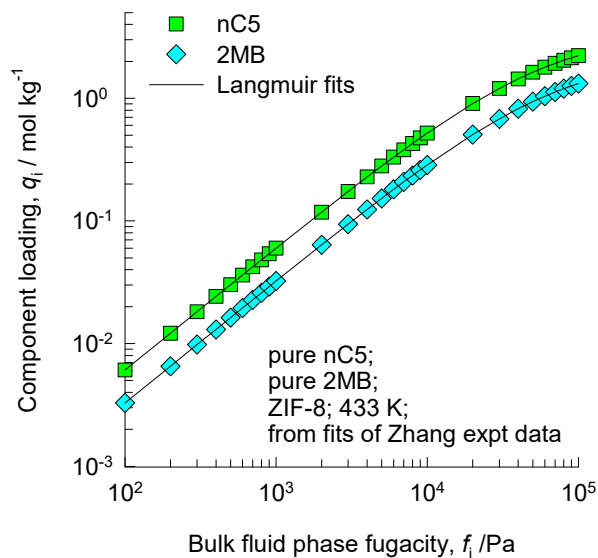
pure nC5;
pure 2MB;
ZIF-8; 433 K;
from fits of Zhang expt data

(b) IAST nC5/2MB mixture
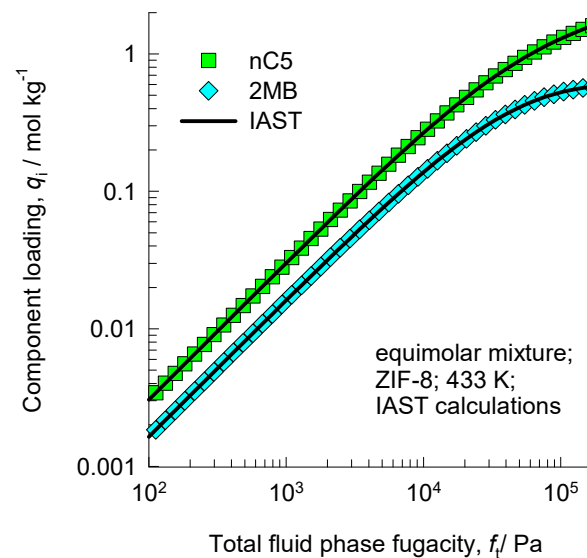
equimolar mixture;
ZIF-8; 433 K;
IAST calculations

(c) nC5/2MB selectivity

equimolar mixture; 433 K
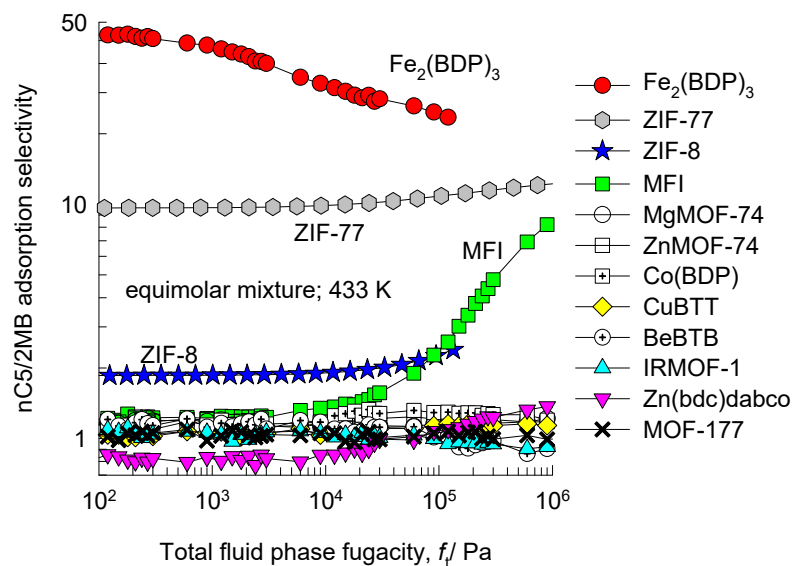
Comparison of adsorption selectivities
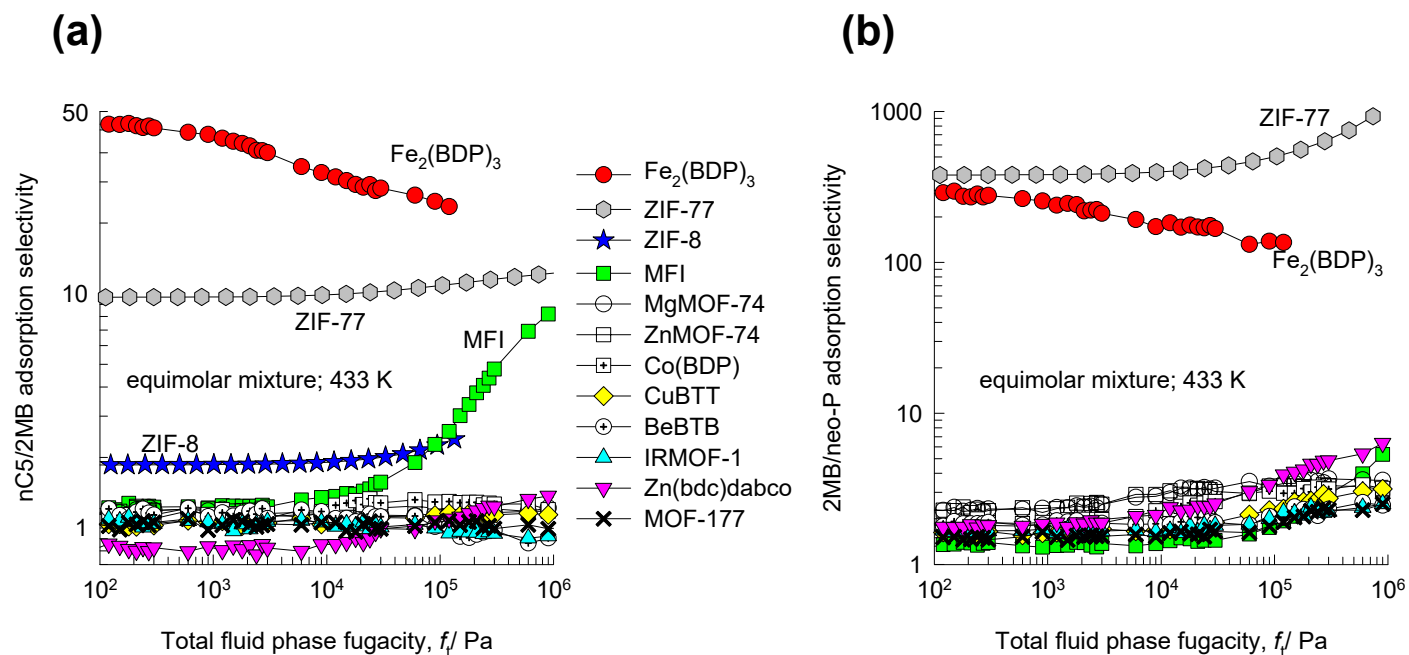
Comparison of uptake capacities

(a)

equimolar mixture; 433 K

- Fe$_2$(BDP)$_3$
- ZIF-77
- ZIF-8
- MFI

nC5 uptake / mol kg^{-1}

Total fluid phase fugacity, f_t/ Pa

(b)

equimolar mixture; 433 K

- Fe$_2$(BDP)$_3$
- ZIF-77
- MFI

2MB uptake / mol kg^{-1}

Total fluid phase fugacity, f_t/ Pa

Fixed bed adsorber

L = length of packed bed

Crystallites

ε = bed voidage
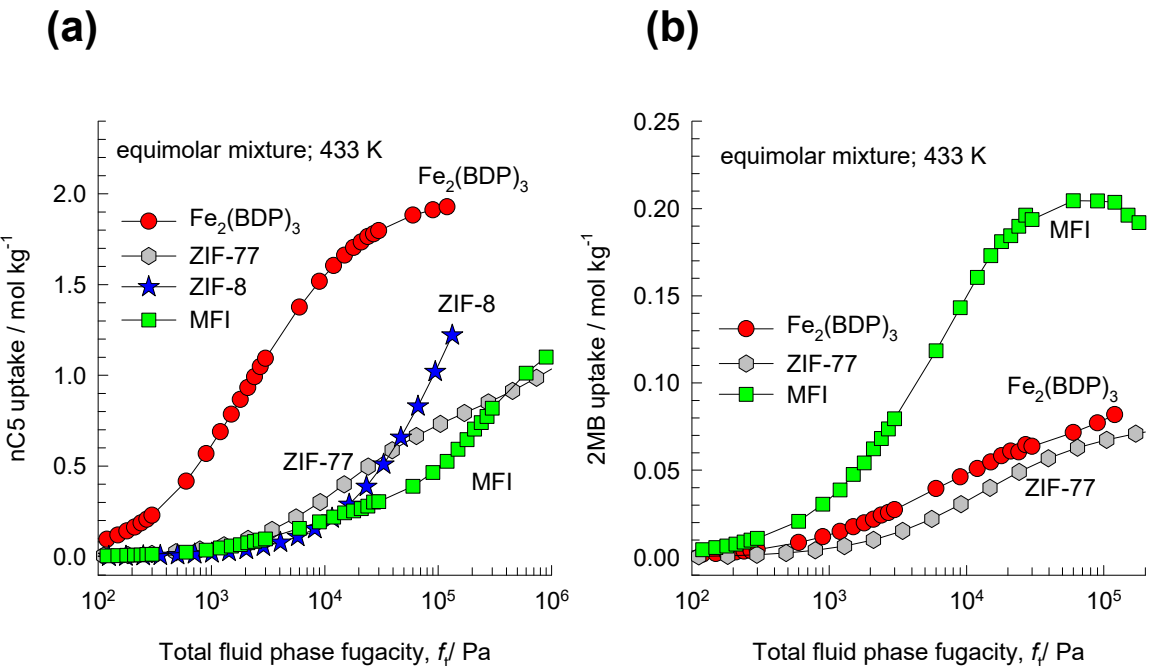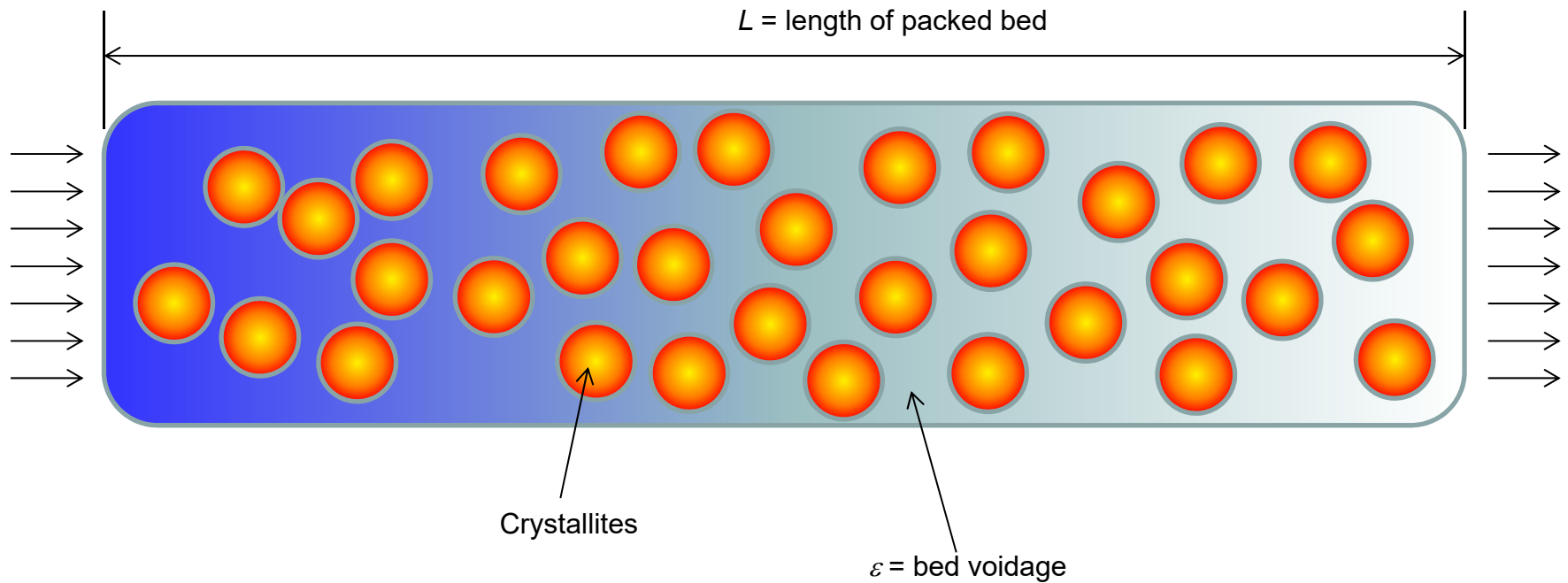
u =
superficial
gas
velocity

$v = u/\varepsilon$ = interstitial gas velocity

L/v =
Characteristic time of contact between gas and liquid

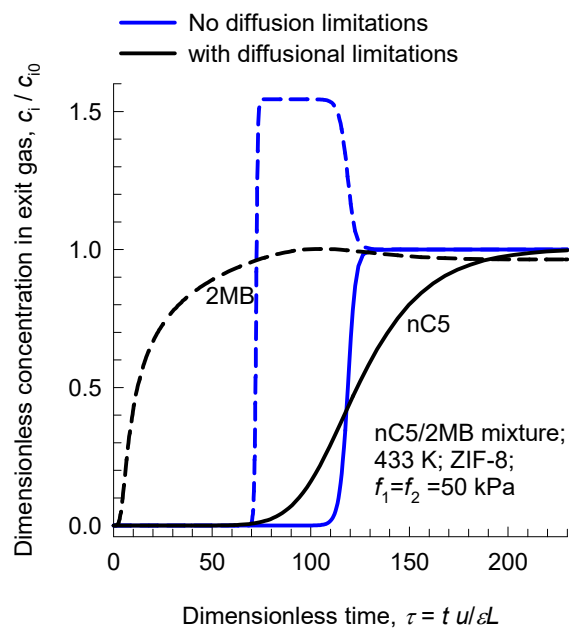# Transient nC5/2MB breakthrough in fixed bed adsorber

(a) Transient breakthroughs
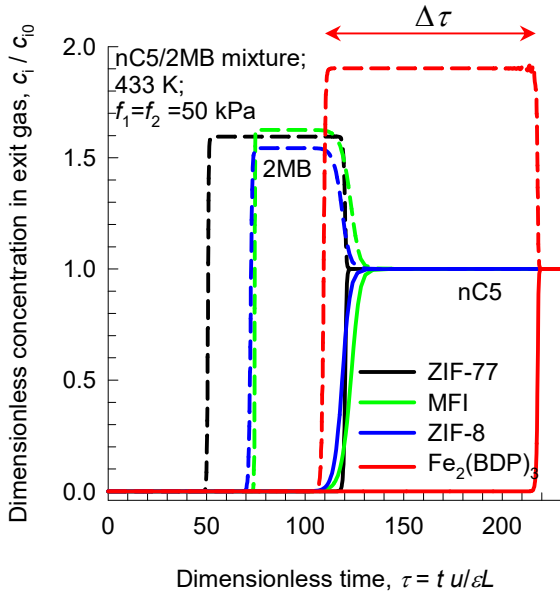
(b) $\Delta\tau$ **vs** τ_{nC5}
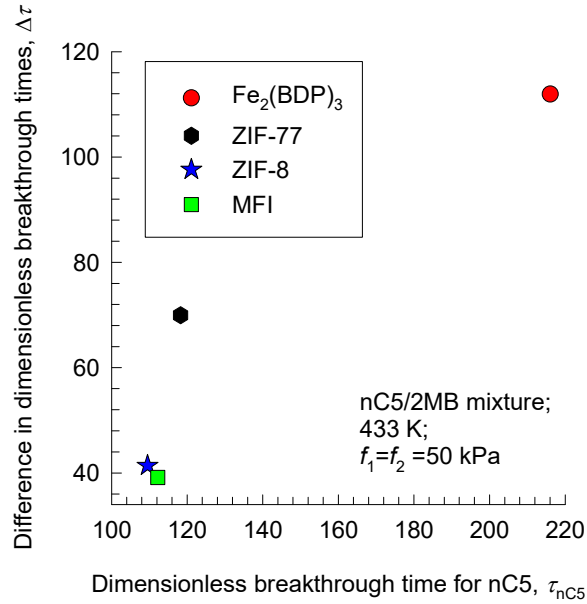
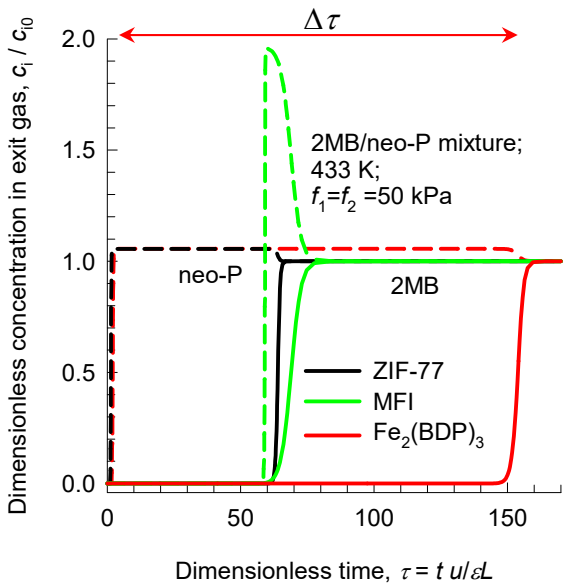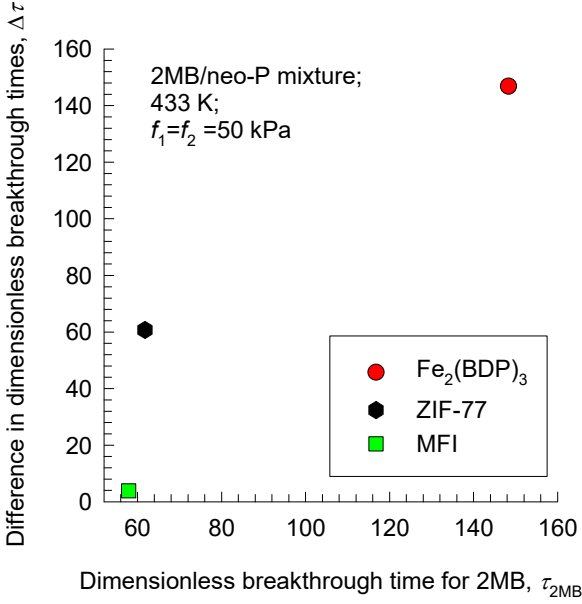# Transient nC5/2MB breakthrough in fixed bed adsorber with ZIF-8 Influence of intra-particle diffusion

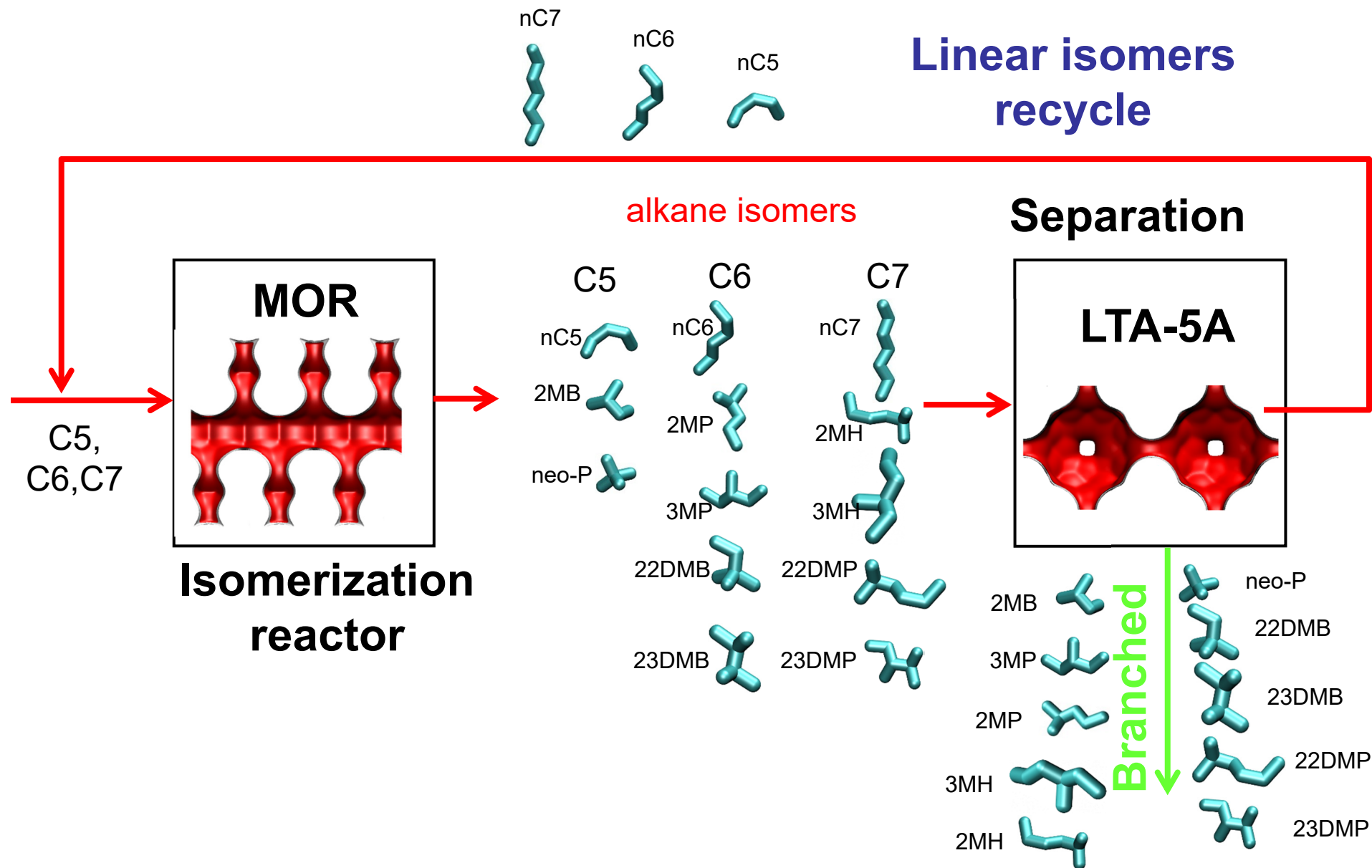# Transient 2MB/neo-P breakthrough in fixed bed adsorber

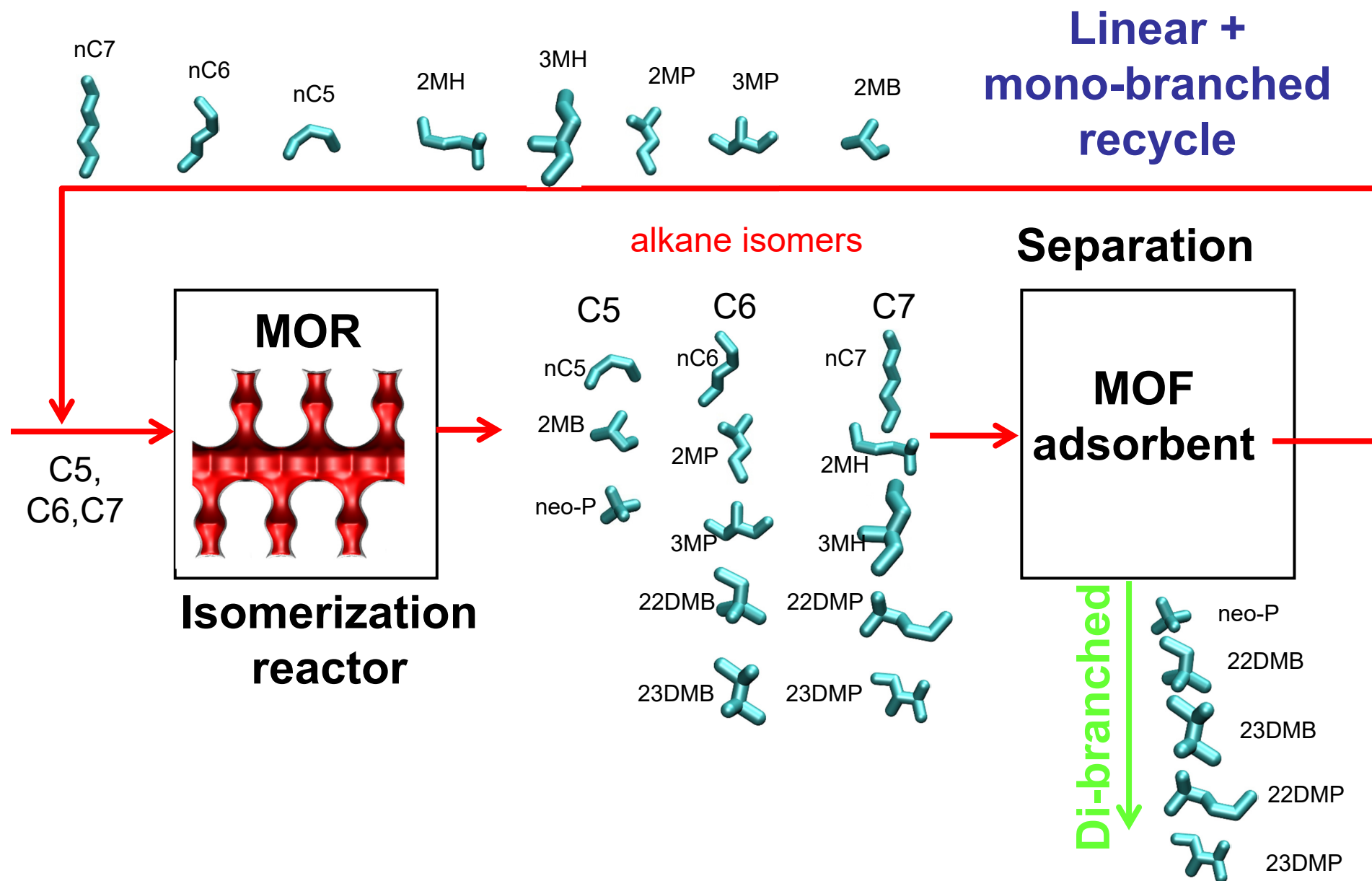**(a) Transient breakthroughs**

(b) $\Delta\tau$ vs τ_{2MB}

Current alkane isomerization process

Figure S63
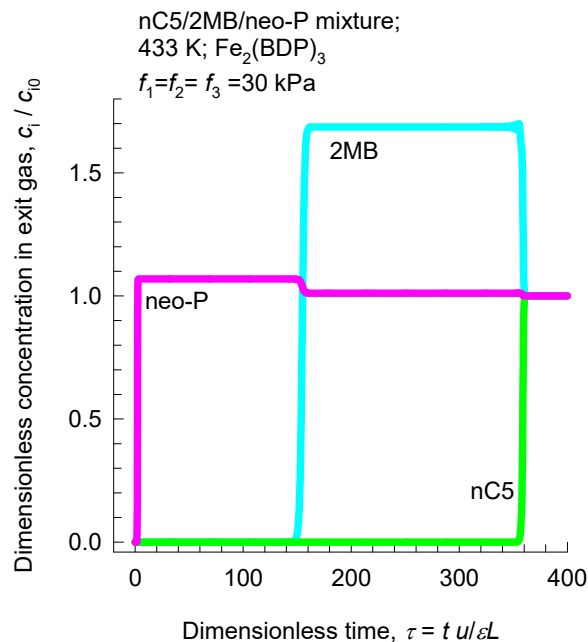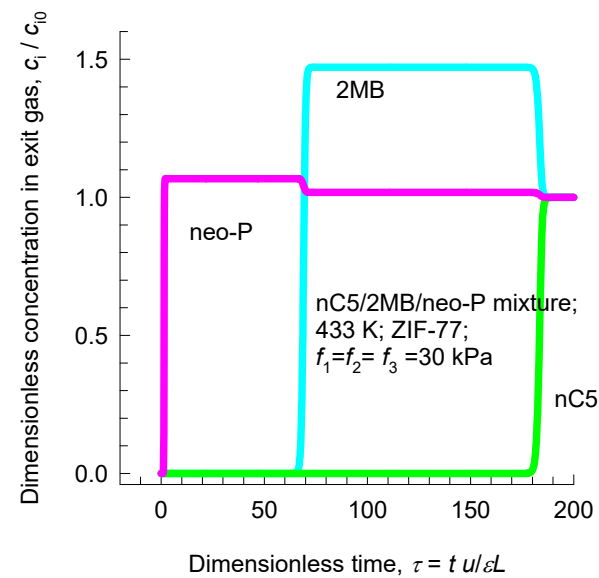
Alkane isomerization process

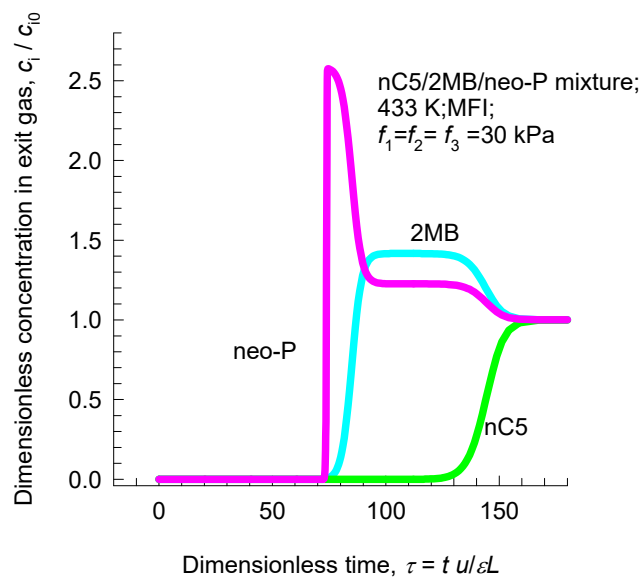# Transient nC5/2MB/neo-P breakthroughs with step-input

(a) Transient breakthroughs with Fe$_2$(BDP)$_3$

nC5/2MB/neo-P mixture;
433 K; Fe$_2$(BDP)$_3$
$f_1=f_2=f_3=30$ kPa

(b) Transient breakthroughs with ZIF-77

nC5/2MB/neo-P mixture;
433 K; ZIF-77;
$f_1=f_2=f_3=30$ kPa

(c) Transient breakthroughs with MFI

nC5/2MB/neo-P mixture;
433 K;MFI;
$f_1=f_2=f_3=30$ kPa

(d) Comparison of product RON vs breakthrough time

nC5/2MB/neo-P mixture;
433 K
$f_1=f_2=f_3=30$ kPa

ZIF-77
MFI
Fe$_2$(BDP)$_3$
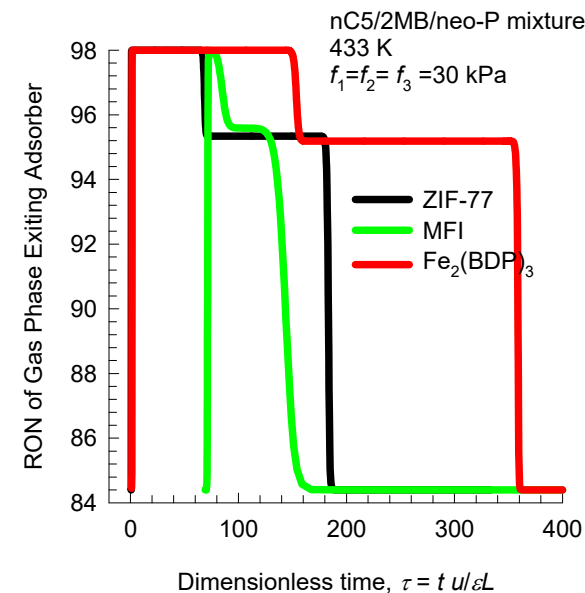
Transient nC6/2MP/3MP/22DMB/23DMB breakthroughs with step-input Figure S66

(a) Transient breakthroughs with $Fe_2(BDP)_3$

nC6-2MP-3MP-
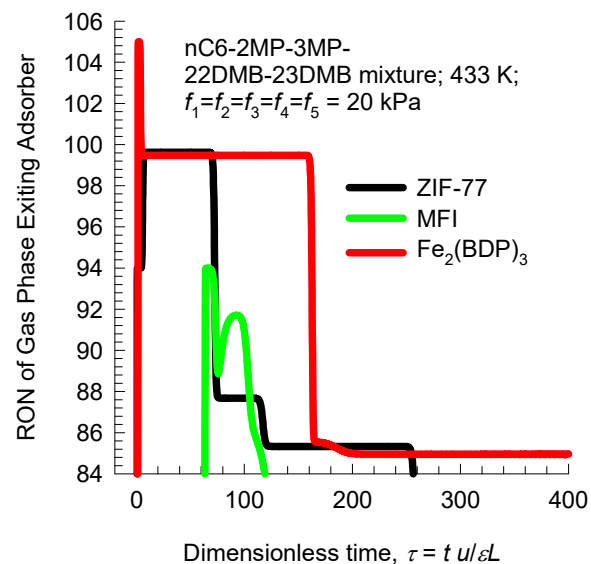22DMB-23DMB mixture;
$Fe_2(BDP)_3$; 433 K;
$f_1=f_2=f_3=f_4=f_5$ = 20 kPa

Dimensionless concentration in exit gas, c_i / c_{i0}

Dimensionless time, $\tau = t\, u/\varepsilon L$

Legend:
- 23DMB
- 22DMB
- 3MP
- 22DMB
- nC6

(b) Comparison of product RON vs breakthrough time

nC6-2MP-3MP-
22DMB-23DMB mixture; 433 K;
$f_1=f_2=f_3=f_4=f_5$ = 20 kPa

RON of Gas Phase Exiting Adsorber

Dimensionless time, $\tau = t\, u/\varepsilon L$

Legend:
- ZIF-77
- MFI
- $Fe_2(BDP)_3$
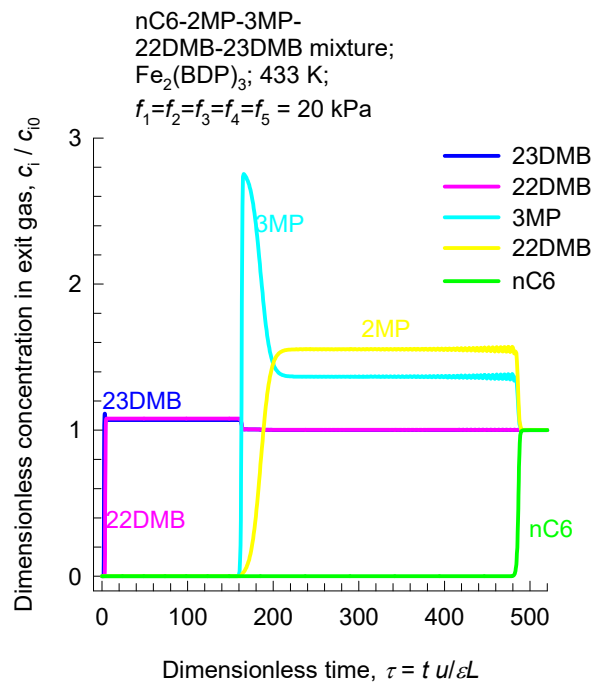
Transient C5/C6 breakthroughs with step-input

(a) Transient breakthroughs with Fe$_2$(BDP)$_3$

C5/C6 mixture; Fe$_2$(BDP)$_3$;
$f_1=f_2=f_3=..=f_8$ = 20 kPa; 433 K;

Legend:
- neo-P
- 23DMB
- 22DMB
- 3MP
- 2MB
- 2MP
- nC5
- nC6

Dimensionless concentration in exit gas, c_i / c_{i0}

Dimensionless time, $\tau = t\, u/\varepsilon L$

(b) Comparison of product RON vs breakthrough time

C5/C6 mixture;
$f_1=f_2=f_3=..=f_8$ = 20 kPa; 433 K;

Legend:
- ZIF-77
- MFI
- Fe$_2$(BDP)$_3$

RON of Gas Phase Exiting Adsorber

Dimensionless time, $\tau = t\, u/\varepsilon L$

Transient C5/C6/C7 breakthroughs with step-input

(a) Transient breakthroughs with Fe$_2$(BDP)$_3$

C5/C6/C7 mixture;
Fe$_2$(BDP)$_3$; 433 K;
$f_1=f_2=f_3..=f_{13}$ = 20 kPa

Legend:
- 23DMB
- 22DMB
- 3MP
- 2MP
- nC6
- nC5
- 2MB
- neo-P
- nC7
- 22DMP
- 23DMP
- 3MH
- 2MH

Y-axis: Dimensionless concentration in exit gas, c_i / c_{i0}
X-axis: Dimensionless time, $\tau = t\, u/\varepsilon L$

(b) Comparison of product RON vs breakthrough time

C5/C6/C7 mixture;
433 K;
$f_1=f_2=f_3..=f_{13}$ = 20 kPa

Legend:
- ZIF-77
- Fe$_2$(BDP)$_3$

Y-axis: RON of Gas Phase Exiting Adsorber
X-axis: Dimensionless time, $\tau = t\, u/\varepsilon L$

Transient breakthroughs: pulse feed input

nC5/2MB/neo-P mixture; 433 K; $Fe_2(BDP)_3$
$f_1 = f_2 = f_3 = 30$ kPa
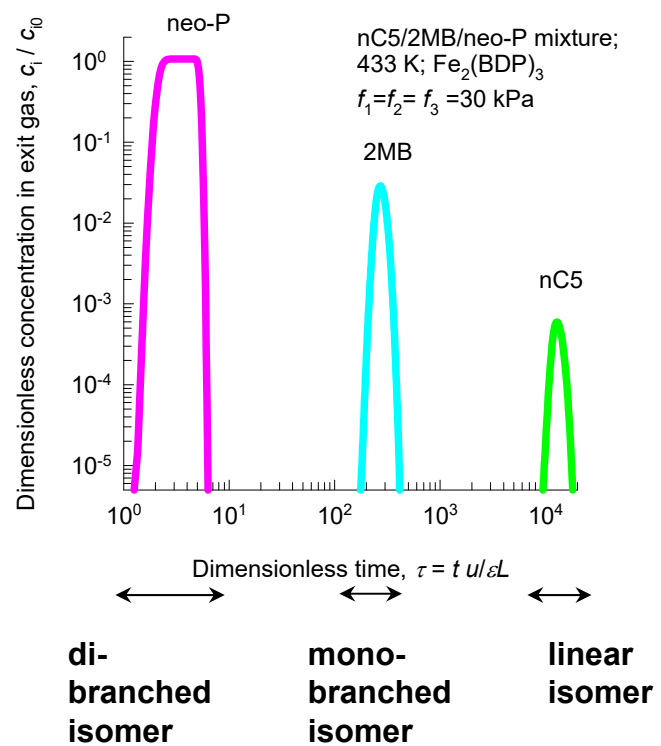
Pulse chromatographic C6 & C7 breakthroughs with Fe$_2$(BDP)$_3$ Figure S70

(a) Hexanes feed mixture

nC6-2MP-3MP-22DMB-23DMB mixture; Fe$_2$(BDP)$_3$; 433 K; $f_1=f_2=f_3=f_4=f_5 = 20$ kPa

Dimensionless concentration in exit gas, c_i / c_{i0}

Dimensionless time, $\tau = t\, u/\varepsilon L$

di-branched isomers   mono-branched isomers   linear isomer

(b) Heptanes feed mixture

nC7-2MH3MH-22DMP-23DMP mixture; $f_1=f_2=f_3=f_4=f_5=20$ kPa; Fe$_2$(BDP)$_3$; 433 K;

Dimensionless concentration in exit gas, c_i / c_{i0}

Dimensionless time, $\tau = t\, u/\varepsilon L$

di-branched isomers   mono-branched isomers   linear isomer
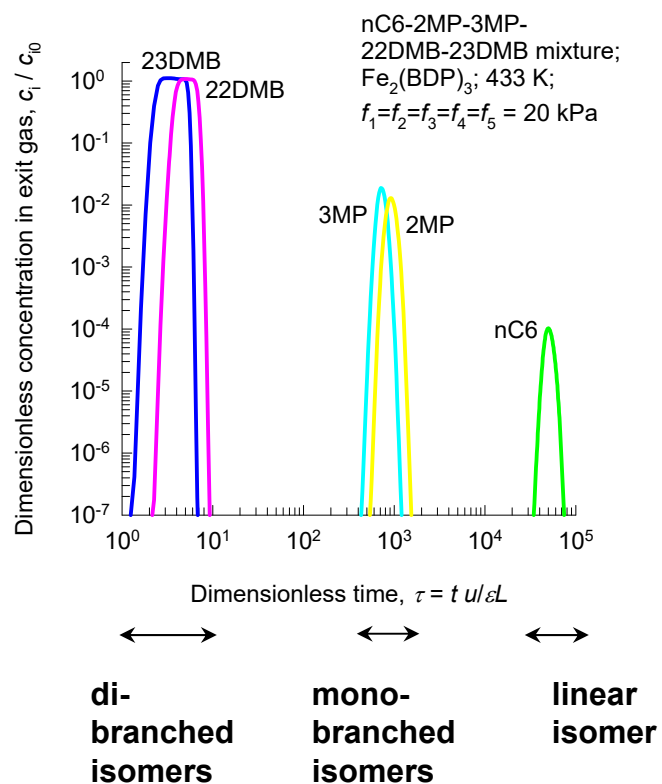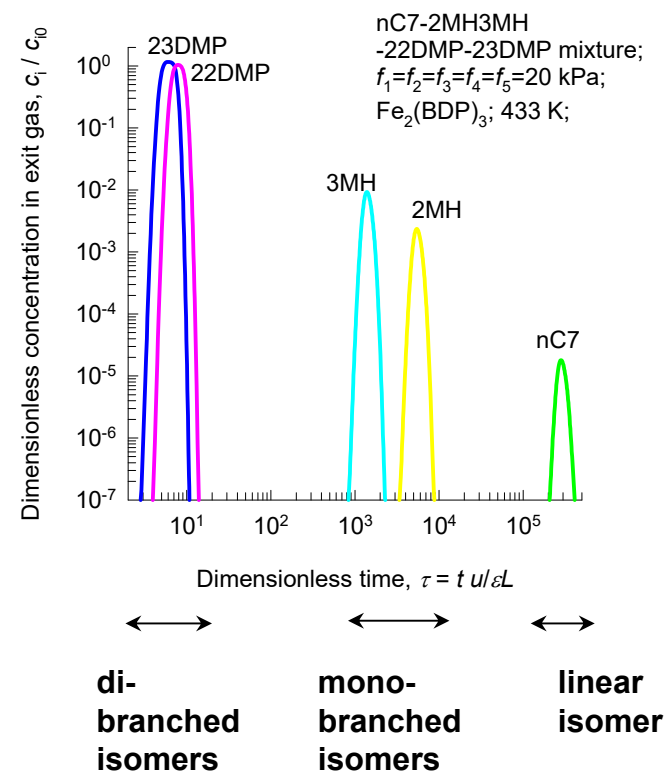
Pulse chromatographic pentanes/hexanes breakthrough with $Fe_2(BDP)_3$
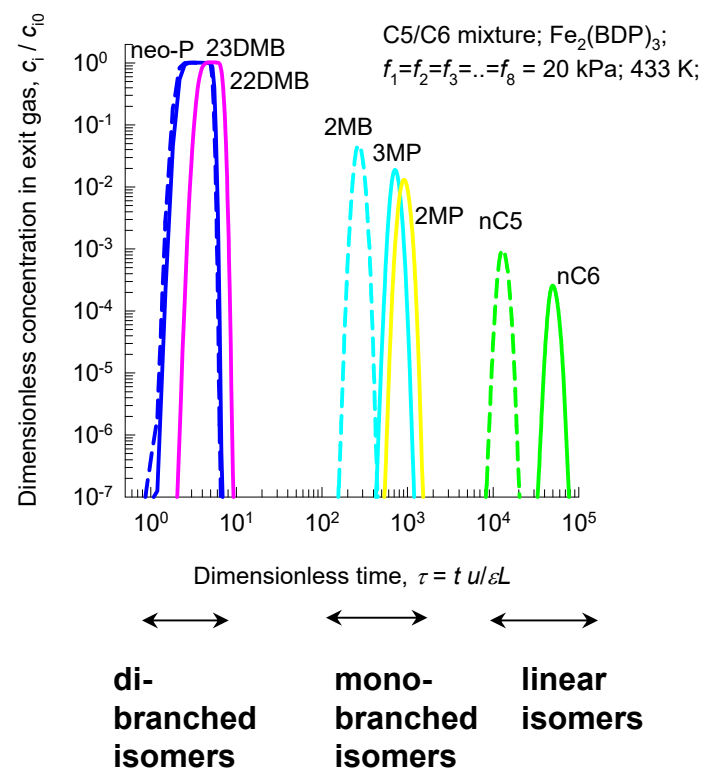
Pulse chromatographic pentanes/hexanes/heptanes breakthrough with $Fe_2(BDP)_3$